

# Measurement of the W Boson Mass and W<sup>+</sup>W<sup>-</sup> Production and Decay Properties in e<sup>+</sup>e<sup>-</sup> Collisions at $\sqrt{s}=172$ GeV

The OPAL Collaboration

## Abstract

This paper describes the measurement of the W boson mass,  $M_W$ , and decay width,  $\Gamma_W$ , from the direct reconstruction of the invariant mass of its decay products in W pair events collected at a mean centre-of-mass energy of  $\sqrt{s}=172.12$  GeV with the OPAL detector at LEP. Measurements of the W pair production cross-section, the W decay branching fractions and properties of the W decay final states are also described. A total of 120 candidate W<sup>+</sup>W<sup>-</sup> events has been selected for an integrated luminosity of 10.36 pb<sup>-1</sup>. The W<sup>+</sup>W<sup>-</sup> production cross-section is measured to be  $\sigma_{WW} = 12.3 \pm 1.3(\text{stat.}) \pm 0.3(\text{syst.})$  pb, consistent with the Standard Model expectation. The W<sup>+</sup>W<sup>-</sup>  $\rightarrow q\bar{q}\ell\bar{\nu}_\ell$  and W<sup>+</sup>W<sup>-</sup>  $\rightarrow q\bar{q}q\bar{q}$  final states are used to obtain a direct measurement of  $\Gamma_W = 1.30_{-0.55}^{+0.62}(\text{stat.}) \pm 0.18(\text{syst.})$  GeV. Assuming the Standard Model relation between  $M_W$  and  $\Gamma_W$ , the W boson mass is measured to be  $M_W = 80.32 \pm 0.30(\text{stat.}) \pm 0.09(\text{syst.})$  GeV. The event properties of the fully-hadronic decays of W<sup>+</sup>W<sup>-</sup> events are compared to those of the semi-leptonic decays. At the current level of precision there is no evidence for effects of colour reconnection in the observables studied. Combining data recorded by OPAL at  $\sqrt{s} \sim 161$ –172 GeV, the W boson branching fraction to hadrons is determined to be  $69.8_{-3.2}^{+3.0}(\text{stat.}) \pm 0.7(\text{syst.})\%$ , consistent with the prediction of the Standard Model. The combined mass measurement from direct reconstruction and from the W<sup>+</sup>W<sup>-</sup> production cross-sections measured at  $\sqrt{s} \sim 161$  and  $\sqrt{s} \sim 172$  GeV is  $M_W = 80.35 \pm 0.24(\text{stat.}) \pm 0.07(\text{syst.})$  GeV.

To be submitted to Zeit. Phys. C

# The OPAL Collaboration

K. Ackerstaff<sup>8</sup>, G. Alexander<sup>23</sup>, J. Allison<sup>16</sup>, N. Altekamp<sup>5</sup>, K.J. Anderson<sup>9</sup>, S. Anderson<sup>12</sup>, S. Arcelli<sup>2</sup>, S. Asai<sup>24</sup>, D. Axen<sup>29</sup>, G. Azuelos<sup>18,a</sup>, A.H. Ball<sup>17</sup>, E. Barberio<sup>8</sup>, R.J. Barlow<sup>16</sup>, R. Bartoldus<sup>3</sup>, J.R. Batley<sup>5</sup>, S. Baumann<sup>3</sup>, J. Bechtluft<sup>14</sup>, C. Beeston<sup>16</sup>, T. Behnke<sup>8</sup>, A.N. Bell<sup>1</sup>, K.W. Bell<sup>20</sup>, G. Bella<sup>23</sup>, S. Bentvelsen<sup>8</sup>, S. Bethke<sup>14</sup>, O. Biebel<sup>14</sup>, A. Biguzzi<sup>5</sup>, S.D. Bird<sup>16</sup>, V. Blobel<sup>27</sup>, I.J. Bloodworth<sup>1</sup>, J.E. Bloomer<sup>1</sup>, M. Bobinski<sup>10</sup>, P. Bock<sup>11</sup>, D. Bonacorsi<sup>2</sup>, M. Boutemeur<sup>34</sup>, B.T. Bouwens<sup>12</sup>, S. Braibant<sup>12</sup>, L. Brigliadori<sup>2</sup>, R.M. Brown<sup>20</sup>, H.J. Burckhart<sup>8</sup>, C. Burgard<sup>8</sup>, R. Bürgin<sup>10</sup>, P. Capiluppi<sup>2</sup>, R.K. Carnegie<sup>6</sup>, A.A. Carter<sup>13</sup>, J.R. Carter<sup>5</sup>, C.Y. Chang<sup>17</sup>, D.G. Charlton<sup>1,b</sup>, D. Chrisman<sup>4</sup>, P.E.L. Clarke<sup>15</sup>, I. Cohen<sup>23</sup>, J.E. Conboy<sup>15</sup>, O.C. Cooke<sup>8</sup>, M. Cuffiani<sup>2</sup>, S. Dado<sup>22</sup>, C. Dallapiccola<sup>17</sup>, G.M. Dallavalle<sup>2</sup>, R. Davis<sup>30</sup>, S. De Jong<sup>12</sup>, L.A. del Pozo<sup>4</sup>, K. Desch<sup>3</sup>, B. Dienes<sup>33,d</sup>, M.S. Dixit<sup>7</sup>, E. do Couto e Silva<sup>12</sup>, M. Doucet<sup>18</sup>, E. Duchovni<sup>26</sup>, G. Duckeck<sup>34</sup>, I.P. Duerdoth<sup>16</sup>, D. Eatough<sup>16</sup>, J.E.G. Edwards<sup>16</sup>, P.G. Estabrooks<sup>6</sup>, H.G. Evans<sup>9</sup>, M. Evans<sup>13</sup>, F. Fabbri<sup>2</sup>, M. Fanti<sup>2</sup>, A.A. Faust<sup>30</sup>, F. Fiedler<sup>27</sup>, M. Fierro<sup>2</sup>, H.M. Fischer<sup>3</sup>, I. Fleck<sup>8</sup>, R. Folman<sup>26</sup>, D.G. Fong<sup>17</sup>, M. Foucher<sup>17</sup>, A. Fürties<sup>8</sup>, D.I. Futyan<sup>16</sup>, P. Gagnon<sup>7</sup>, J.W. Gary<sup>4</sup>, J. Gascon<sup>18</sup>, S.M. Gascon-Shotkin<sup>17</sup>, N.I. Geddes<sup>20</sup>, C. Geich-Gimbel<sup>3</sup>, T. Geralis<sup>20</sup>, G. Giacomelli<sup>2</sup>, P. Giacomelli<sup>4</sup>, R. Giacomelli<sup>2</sup>, V. Gibson<sup>5</sup>, W.R. Gibson<sup>13</sup>, D.M. Gingrich<sup>30,a</sup>, D. Glenzinski<sup>9</sup>, J. Goldberg<sup>22</sup>, M.J. Goodrick<sup>5</sup>, W. Gorn<sup>4</sup>, C. Grandi<sup>2</sup>, E. Gross<sup>26</sup>, J. Grunhaus<sup>23</sup>, M. Gruwé<sup>8</sup>, C. Hajdu<sup>32</sup>, G.G. Hanson<sup>12</sup>, M. Hansroul<sup>8</sup>, M. Hapke<sup>13</sup>, C.K. Hargrove<sup>7</sup>, P.A. Hart<sup>9</sup>, C. Hartmann<sup>3</sup>, M. Hauschild<sup>8</sup>, C.M. Hawkes<sup>5</sup>, R. Hawkings<sup>27</sup>, R.J. Hemingway<sup>6</sup>, M. Herndon<sup>17</sup>, G. Herten<sup>10</sup>, R.D. Heuer<sup>8</sup>, M.D. Hildreth<sup>8</sup>, J.C. Hill<sup>5</sup>, S.J. Hillier<sup>1</sup>, P.R. Hobson<sup>25</sup>, R.J. Homer<sup>1</sup>, A.K. Honma<sup>28,a</sup>, D. Horváth<sup>32,c</sup>, K.R. Hossain<sup>30</sup>, R. Howard<sup>29</sup>, P. Hütemeyer<sup>27</sup>, D.E. Hutchcroft<sup>5</sup>, P. Igo-Kemenes<sup>11</sup>, D.C. Imrie<sup>25</sup>, M.R. Ingram<sup>16</sup>, K. Ishii<sup>24</sup>, A. Jawahery<sup>17</sup>, P.W. Jeffreys<sup>20</sup>, H. Jeremie<sup>18</sup>, M. Jimack<sup>1</sup>, A. Joly<sup>18</sup>, C.R. Jones<sup>5</sup>, G. Jones<sup>16</sup>, M. Jones<sup>6</sup>, U. Jost<sup>11</sup>, P. Jovanovic<sup>1</sup>, T.R. Junk<sup>8</sup>, D. Karlen<sup>6</sup>, V. Kartvelishvili<sup>16</sup>, K. Kawagoe<sup>24</sup>, T. Kawamoto<sup>24</sup>, P.I. Kayal<sup>30</sup>, R.K. Keeler<sup>28</sup>, R.G. Kellogg<sup>17</sup>, B.W. Kennedy<sup>20</sup>, J. Kirk<sup>29</sup>, A. Klier<sup>26</sup>, S. Kluth<sup>8</sup>, T. Kobayashi<sup>24</sup>, M. Kobel<sup>10</sup>, D.S. Koetke<sup>6</sup>, T.P. Kokott<sup>3</sup>, M. Kolrep<sup>10</sup>, S. Komamiya<sup>24</sup>, T. Kress<sup>11</sup>, P. Krieger<sup>6</sup>, J. von Krogh<sup>11</sup>, P. Kyberd<sup>13</sup>, G.D. Lafferty<sup>16</sup>, R. Lahmann<sup>17</sup>, W.P. Lai<sup>19</sup>, D. Lanske<sup>14</sup>, J. Lauber<sup>15</sup>, S.R. Lautenschlager<sup>31</sup>, J.G. Layter<sup>4</sup>, D. Lazic<sup>22</sup>, A.M. Lee<sup>31</sup>, E. Lefebvre<sup>18</sup>, D. Lellouch<sup>26</sup>, J. Letts<sup>12</sup>, L. Levinson<sup>26</sup>, S.L. Lloyd<sup>13</sup>, F.K. Loebinger<sup>16</sup>, G.D. Long<sup>28</sup>, M.J. Losty<sup>7</sup>, J. Ludwig<sup>10</sup>, A. Macchiolo<sup>2</sup>, A. Macpherson<sup>30</sup>, M. Mannelli<sup>8</sup>, S. Marcellini<sup>2</sup>, C. Markus<sup>3</sup>, A.J. Martin<sup>13</sup>, J.P. Martin<sup>18</sup>, G. Martinez<sup>17</sup>, T. Mashimo<sup>24</sup>, P. Mättig<sup>3</sup>, W.J. McDonald<sup>30</sup>, J. McKenna<sup>29</sup>, E.A. Mckigney<sup>15</sup>, T.J. McMahon<sup>1</sup>, R.A. McPherson<sup>8</sup>, F. Meijers<sup>8</sup>, S. Menke<sup>3</sup>, F.S. Merritt<sup>9</sup>, H. Mes<sup>7</sup>, J. Meyer<sup>27</sup>, A. Michelini<sup>2</sup>, G. Mikenberg<sup>26</sup>, D.J. Miller<sup>15</sup>, A. Mincer<sup>22,e</sup>, R. Mir<sup>26</sup>, W. Mohr<sup>10</sup>, A. Montanari<sup>2</sup>, T. Mori<sup>24</sup>, M. Morii<sup>24</sup>, U. Müller<sup>3</sup>, S. Mihara<sup>24</sup>, K. Nagai<sup>26</sup>, I. Nakamura<sup>24</sup>, H.A. Neal<sup>8</sup>, B. Nellen<sup>3</sup>, R. Nisius<sup>8</sup>, S.W. O’Neale<sup>1</sup>, F.G. Oakham<sup>7</sup>, F. Odoric<sup>2</sup>, H.O. Ogren<sup>12</sup>, A. Oh<sup>27</sup>, N.J. Oldershaw<sup>16</sup>, M.J. Oreglia<sup>9</sup>, S. Orito<sup>24</sup>, J. Pálinkás<sup>33,d</sup>, G. Pásztor<sup>32</sup>, J.R. Pater<sup>16</sup>, G.N. Patrick<sup>20</sup>, J. Patt<sup>10</sup>, M.J. Pearce<sup>1</sup>, R. Perez-Ochoa<sup>8</sup>, S. Petzold<sup>27</sup>, P. Pfeifenschneider<sup>14</sup>, J.E. Pilcher<sup>9</sup>, J. Pinfold<sup>30</sup>, D.E. Plane<sup>8</sup>, P. Poffenberger<sup>28</sup>, B. Poli<sup>2</sup>, A. Posthaus<sup>3</sup>, D.L. Rees<sup>1</sup>, D. Rigby<sup>1</sup>, S. Robertson<sup>28</sup>, S.A. Robins<sup>22</sup>, N. Rodning<sup>30</sup>, J.M. Roney<sup>28</sup>, A. Rooke<sup>15</sup>, E. Ros<sup>8</sup>, A.M. Rossi<sup>2</sup>, P. Routenburg<sup>30</sup>, Y. Rozen<sup>22</sup>, K. Runge<sup>10</sup>, O. Runolfsson<sup>8</sup>, U. Ruppel<sup>14</sup>, D.R. Rust<sup>12</sup>, R. Rylko<sup>25</sup>, K. Sachs<sup>10</sup>, T. Saeki<sup>24</sup>, E.K.G. Sarkisyan<sup>23</sup>, C. Sbarra<sup>29</sup>, A.D. Schaile<sup>34</sup>, O. Schaile<sup>34</sup>, F. Scharf<sup>3</sup>, P. Scharff-Hansen<sup>8</sup>, P. Schenk<sup>34</sup>, J. Schieck<sup>11</sup>, P. Schleper<sup>11</sup>, B. Schmitt<sup>8</sup>, S. Schmitt<sup>11</sup>, A. Schönig<sup>8</sup>, M. Schröder<sup>8</sup>, H.C. Schultz-Coulon<sup>10</sup>, M. Schumacher<sup>3</sup>, C. Schwick<sup>8</sup>, W.G. Scott<sup>20</sup>, T.G. Shears<sup>16</sup>, B.C. Shen<sup>4</sup>, C.H. Shepherd-Themistocleous<sup>8</sup>, P. Sherwood<sup>15</sup>, G.P. Siroli<sup>2</sup>, A. Sittler<sup>27</sup>, A. Skillman<sup>15</sup>, A. Skuja<sup>17</sup>, A.M. Smith<sup>8</sup>, G.A. Snow<sup>17</sup>, R. Sobie<sup>28</sup>, S. Söldner-Rembold<sup>10</sup>, R.W. Springer<sup>30</sup>, M. Sproston<sup>20</sup>, K. Stephens<sup>16</sup>, J. Steuerer<sup>27</sup>, B. Stockhausen<sup>3</sup>, K. Stoll<sup>10</sup>, D. Strom<sup>19</sup>, P. Szymanski<sup>20</sup>, R. Tafirout<sup>18</sup>, S.D. Talbot<sup>1</sup>, S. Tanaka<sup>24</sup>, P. Taras<sup>18</sup>, S. Tarem<sup>22</sup>, R. Teuscher<sup>8</sup>, M. Thiergen<sup>10</sup>, M.A. Thomson<sup>8</sup>, E. von Törne<sup>3</sup>, S. Towers<sup>6</sup>, I. Trigger<sup>18</sup>, Z. Trócsányi<sup>33</sup>, E. Tsur<sup>23</sup>, A.S. Turcot<sup>9</sup>, M.F. Turner-Watson<sup>8</sup>, P. Utzat<sup>11</sup>, R. Van Kooten<sup>12</sup>, M. Verzocchi<sup>10</sup>, P. Vikas<sup>18</sup>, E.H. Vokurka<sup>16</sup>, H. Voss<sup>3</sup>, F. Wäckerle<sup>10</sup>,

A. Wagner<sup>27</sup>, C.P. Ward<sup>5</sup>, D.R. Ward<sup>5</sup>, P.M. Watkins<sup>1</sup>, A.T. Watson<sup>1</sup>, N.K. Watson<sup>1</sup>, P.S. Wells<sup>8</sup>,  
N. Wermes<sup>3</sup>, J.S. White<sup>28</sup>, B. Wilkens<sup>10</sup>, G.W. Wilson<sup>27</sup>, J.A. Wilson<sup>1</sup>, G. Wolf<sup>26</sup>, T.R. Wyatt<sup>16</sup>,  
S. Yamashita<sup>24</sup>, G. Yekutieli<sup>26</sup>, V. Zacek<sup>18</sup>, D. Zer-Zion<sup>8</sup>

<sup>1</sup>School of Physics and Space Research, University of Birmingham, Birmingham B15 2TT, UK

<sup>2</sup>Dipartimento di Fisica dell' Università di Bologna and INFN, I-40126 Bologna, Italy

<sup>3</sup>Physikalisches Institut, Universität Bonn, D-53115 Bonn, Germany

<sup>4</sup>Department of Physics, University of California, Riverside CA 92521, USA

<sup>5</sup>Cavendish Laboratory, Cambridge CB3 0HE, UK

<sup>6</sup>Ottawa-Carleton Institute for Physics, Department of Physics, Carleton University, Ottawa, Ontario K1S 5B6, Canada

<sup>7</sup>Centre for Research in Particle Physics, Carleton University, Ottawa, Ontario K1S 5B6, Canada

<sup>8</sup>CERN, European Organisation for Particle Physics, CH-1211 Geneva 23, Switzerland

<sup>9</sup>Enrico Fermi Institute and Department of Physics, University of Chicago, Chicago IL 60637, USA

<sup>10</sup>Fakultät für Physik, Albert Ludwigs Universität, D-79104 Freiburg, Germany

<sup>11</sup>Physikalisches Institut, Universität Heidelberg, D-69120 Heidelberg, Germany

<sup>12</sup>Indiana University, Department of Physics, Swain Hall West 117, Bloomington IN 47405, USA

<sup>13</sup>Queen Mary and Westfield College, University of London, London E1 4NS, UK

<sup>14</sup>Technische Hochschule Aachen, III Physikalisches Institut, Sommerfeldstrasse 26-28, D-52056 Aachen, Germany

<sup>15</sup>University College London, London WC1E 6BT, UK

<sup>16</sup>Department of Physics, Schuster Laboratory, The University, Manchester M13 9PL, UK

<sup>17</sup>Department of Physics, University of Maryland, College Park, MD 20742, USA

<sup>18</sup>Laboratoire de Physique Nucléaire, Université de Montréal, Montréal, Quebec H3C 3J7, Canada

<sup>19</sup>University of Oregon, Department of Physics, Eugene OR 97403, USA

<sup>20</sup>Rutherford Appleton Laboratory, Chilton, Didcot, Oxfordshire OX11 0QX, UK

<sup>22</sup>Department of Physics, Technion-Israel Institute of Technology, Haifa 32000, Israel

<sup>23</sup>Department of Physics and Astronomy, Tel Aviv University, Tel Aviv 69978, Israel

<sup>24</sup>International Centre for Elementary Particle Physics and Department of Physics, University of Tokyo, Tokyo 113, and Kobe University, Kobe 657, Japan

<sup>25</sup>Brunel University, Uxbridge, Middlesex UB8 3PH, UK

<sup>26</sup>Particle Physics Department, Weizmann Institute of Science, Rehovot 76100, Israel

<sup>27</sup>Universität Hamburg/DESY, II Institut für Experimental Physik, Notkestrasse 85, D-22607 Hamburg, Germany

<sup>28</sup>University of Victoria, Department of Physics, P O Box 3055, Victoria BC V8W 3P6, Canada

<sup>29</sup>University of British Columbia, Department of Physics, Vancouver BC V6T 1Z1, Canada

<sup>30</sup>University of Alberta, Department of Physics, Edmonton AB T6G 2J1, Canada

<sup>31</sup>Duke University, Dept of Physics, Durham, NC 27708-0305, USA

<sup>32</sup>Research Institute for Particle and Nuclear Physics, H-1525 Budapest, P O Box 49, Hungary

<sup>33</sup>Institute of Nuclear Research, H-4001 Debrecen, P O Box 51, Hungary

<sup>34</sup>Ludwigs-Maximilians-Universität München, Sektion Physik, Am Coulombwall 1, D-85748 Garching, Germany

<sup>a</sup> and at TRIUMF, Vancouver, Canada V6T 2A3

<sup>b</sup> and Royal Society University Research Fellow

<sup>c</sup> and Institute of Nuclear Research, Debrecen, Hungary

<sup>d</sup> and Department of Experimental Physics, Lajos Kossuth University, Debrecen, Hungary

<sup>e</sup> and Department of Physics, New York University, NY 1003, USA

# 1 Introduction

In 1996, the LEP collider at CERN entered a new phase of operation, LEP2, with the first  $e^+e^-$  collisions above the  $W^+W^-$  production threshold. Approximately  $10 \text{ pb}^{-1}$  of integrated luminosity was delivered to each of the four LEP experiments at a centre-of-mass energy  $\sqrt{s} \sim 161 \text{ GeV}$ . Subsequently, a further  $\sim 10 \text{ pb}^{-1}$  was delivered at a higher energy of  $\sqrt{s} \sim 172 \text{ GeV}$ . This paper describes measurements of the production and decay properties of  $W^+W^-$  events in this higher energy run.

One of the principal goals of the LEP2 programme is the measurement of the mass of the W boson,  $M_W$ . Comparison between this direct measurement and the value of  $M_W$  determined indirectly from precise electroweak analyses at  $\sqrt{s} \sim 91 \text{ GeV}$  (LEP1) and elsewhere will eventually provide an important new test of the Standard Model (SM) of electroweak interactions. Direct measurements of  $M_W$  from hadron colliders currently yield  $80.33 \pm 0.15 \text{ GeV}$  [1–3]. Ultimately it is believed [4] that LEP2 can achieve a precision on the W mass of approximately 30–40 MeV. The mass dependence of the  $W^+W^-$  production cross-section at threshold,  $\sqrt{s} \sim 161 \text{ GeV}$ , was used to extract the first measurements of  $M_W$  from LEP2 data [5–8]. At higher centre-of-mass energies measurement of the  $W^+W^-$  cross-section itself provides an interesting test of the non-Abelian gauge structure of the Standard Model, which predicts substantial destructive interference between the different  $W^+W^-$  production diagrams, thus avoiding unitarity violation at higher energies.

This paper describes the measurement, above  $W^+W^-$  production threshold, of  $M_W$  and of the W decay width,  $\Gamma_W$ , by direct reconstruction of the invariant mass spectrum of the W decay products. The mass and width measurements use events in the channels<sup>1</sup>  $W^+W^- \rightarrow q\bar{q}q\bar{q}$  and  $W^+W^- \rightarrow q\bar{q}\ell\bar{\nu}_\ell$  ( $\ell=e, \mu$  or  $\tau$ ). For each event, the mass of the W is reconstructed from its decay products, and  $M_W$  and  $\Gamma_W$  are determined by a fit to the resulting distribution.

The structure of the paper is as follows. Section 2 contains a brief overview of the OPAL detector and the Monte Carlo models used. Section 3 describes the selection methods used for the identification of samples of  $W^+W^- \rightarrow \ell^+\nu_\ell\ell'^-\bar{\nu}_{\ell'}$ ,  $W^+W^- \rightarrow q\bar{q}\ell\bar{\nu}_\ell$  and  $W^+W^- \rightarrow q\bar{q}q\bar{q}$  events at  $\sqrt{s} \simeq 172 \text{ GeV}$ . In Section 4, these selections are used to determine the  $W^+W^-$  production cross-section and the branching fractions of the W boson into various final states. These results may be interpreted in terms of a measurement of the Cabibbo-Kobayashi-Maskawa (CKM) mixing parameter  $|V_{cs}|$ . In Section 5 the  $W^+W^- \rightarrow q\bar{q}q\bar{q}$  and  $W^+W^- \rightarrow q\bar{q}\ell\bar{\nu}_\ell$  samples are used for a determination of the W mass and width. Finally, Section 6 discusses the properties of the hadronic W decays, which are potentially sensitive to interesting QCD final-state interactions between the products of the two W decays.

## 2 The OPAL Detector, Data and Monte Carlo Models

### 2.1 Detector

A detailed description of the OPAL detector has been presented elsewhere [9] and therefore only the features relevant to this analysis are summarised here. Charged particle trajectories are reconstructed using the cylindrical central tracking detectors, which consist of a silicon microvertex detector, a high precision vertex detector, a large volume jet chamber and thin  $z$ -chambers. The silicon microvertex detector consists of two layers of silicon strip detectors, allowing at least one hit per charged track in

---

<sup>1</sup>Throughout this paper, a reference to  $W^+$  or its decay products implicitly includes the charge conjugate states.

the angular<sup>2</sup> region  $|\cos\theta| < 0.93$ . It is surrounded by a vertex drift chamber. Outside this lies the jet chamber, about 400 cm in length and 185 cm in radius, which provides up to 159 space points per track, and measures the ionisation energy loss of charged particles,  $dE/dx$  [10]. The  $z$ -chambers, which improve considerably the measurement of charged tracks in  $\theta$ , are situated immediately beyond and co-axial with the jet chamber. Track finding is nearly 100% efficient within the angular region  $|\cos\theta| < 0.97$ . The entire central detector is contained within a solenoid which provides an axial magnetic field of 0.435 T.

The electromagnetic calorimeter (ECAL) measures the energy of electrons and photons and provides a partial energy measurement for hadrons. It consists of a cylindrical ensemble of 9440 lead glass blocks arranged such that the inter-block gaps point slightly away from the origin, and of two endcaps, each having 1132 lead glass blocks aligned parallel to the beam axis. The barrel encompasses the angular region  $|\cos\theta| < 0.82$  whilst the endcaps cover the region  $0.81 < |\cos\theta| < 0.98$ .

Calorimeters close to the beam axis measure the luminosity using small angle Bhabha scattering events and complete the geometrical acceptance down to 34 mrad from the beam axis. These include the forward detectors which are lead-scintillator sandwich calorimeters and, at smaller angles, silicon tungsten calorimeters [11] located on both sides of the interaction point.

The iron return yoke of the magnet lies outside the electromagnetic calorimeter, and is instrumented with streamer tubes as a hadron calorimeter (HCAL). Muon detectors are situated outside the hadron calorimeter. Muons with momenta above 3 GeV usually penetrate to the muon detectors. In addition, up to nine hits may be recorded for minimum ionising particles traversing the hadron calorimeter, further enhancing muon identification.

## 2.2 Data and Monte Carlo

The basic data selection, luminosity measurement, Monte Carlo (MC) models and detector simulation are identical to those described in [5]. The accepted integrated luminosity, evaluated using small angle Bhabha scattering events observed in the silicon tungsten forward calorimeter, is  $10.363 \pm 0.045(\text{stat.}) \pm 0.036(\text{syst.}) \text{ pb}^{-1}$  [12], of which approximately  $1 \text{ pb}^{-1}$  was collected at 170.3 GeV and  $9.3 \text{ pb}^{-1}$  at 172.3 GeV. The luminosity weighted mean centre-of-mass energy for the data sample is  $\sqrt{s} = 172.12 \pm 0.06 \text{ GeV}$  [13].

The GENTLE [14] semi-analytic program is used to calculate the Standard Model  $W^+W^-$  cross-section which is used throughout this paper to determine the expected number of  $W^+W^-$  events. The use of GENTLE is motivated by the fact that it provides a more complete calculation than current Monte Carlo generators [4]. The calculated cross-section is 12.4 pb at  $\sqrt{s} = 172.12 \text{ GeV}$  using the current world-average W boson mass of  $M_W = 80.33 \text{ GeV}$  [1,2].

In the analyses described below, a number of Monte Carlo models were used to provide estimates of efficiencies and backgrounds as well as the shapes of the W mass distributions. The majority of the Monte Carlo samples were generated at  $\sqrt{s} = 171 \text{ GeV}$  with  $M_W = 80.33 \text{ GeV}$ . Unless stated otherwise, all Monte Carlo samples were generated with a full simulation of the OPAL detector [15]. A number of Monte Carlo studies were performed without detector simulation, referred to as generator level.

---

<sup>2</sup>The OPAL right-handed coordinate system is defined such that the origin is at the geometric centre of the jet chamber,  $z$  is parallel to, and has positive sense along, the  $e^-$  beam direction,  $r$  is the coordinate normal to  $z$ ,  $\theta$  is the polar angle with respect to  $+z$  and  $\phi$  is the azimuthal angle around  $z$ .

The separation between signal and background processes is complicated by the interference between the  $W^+W^-$  production diagrams (class<sup>3</sup> CC03) and other four-fermion graphs. For example, the process  $Z^0/\gamma \rightarrow q\bar{q}$  where a  $W^\pm$  is radiated off one of the quarks can interfere with  $W^+W^- \rightarrow q\bar{q}\ell\bar{\nu}_\ell$  and  $W^+W^- \rightarrow q\bar{q}q\bar{q}$  final states. Monte Carlo samples of  $W^+W^-$  events, restricted to the CC03 diagrams, were obtained with the KORALW [16], EXCALIBUR [17], grc4f [18], PYTHIA [19] and HERWIG [20] generators. KORALW was used to determine the efficiencies for  $W^+W^-$  events for the selections presented in this paper. This sample was generated at  $\sqrt{s} = 171$  GeV using a value for  $M_W$  of 80.33 GeV. A number of PYTHIA Monte Carlo samples generated with different values of  $\sqrt{s}$  and  $M_W$  were used to investigate the sensitivities of the analyses to these parameters. EXCALIBUR was used to investigate the sensitivity to  $\Gamma_W$ .

The main background process,  $Z^0/\gamma \rightarrow q\bar{q}$ , was simulated using PYTHIA, with HERWIG used as an alternative to study possible systematic effects. Other backgrounds involving two fermions in the final state were studied using KORALZ [21] for  $e^+e^- \rightarrow \mu^+\mu^-$ ,  $e^+e^- \rightarrow \tau^+\tau^-$  and  $e^+e^- \rightarrow \nu\bar{\nu}\gamma\gamma$ , and BHWIDE [22] for  $e^+e^- \rightarrow e^+e^-$ . Backgrounds from processes with four fermions in the final state were evaluated using grc4f, EXCALIBUR and FERMISV [23]. Backgrounds from two-photon processes were evaluated using PYTHIA, HERWIG, PHOJET [24], TWOGEN [25] and the Vermaseren program [26]. At least two independent Monte Carlo estimates were available for each category of two-photon and four-fermion background. To study the influence of interference effects in the four-fermion final states the grc4f and EXCALIBUR Monte Carlo generators were used. In both cases samples were generated using the full set of interfering four fermion diagrams. These four-fermion samples were compared to samples obtained with the same generator using only the CC03 set of W pair production diagrams.

Throughout this paper it is assumed that the production cross-section at  $\sqrt{s} \sim 172$  GeV for the Standard Model Higgs boson,  $H^0$ , is negligible. This assumption is valid for a Higgs mass above 80 GeV. Below this mass, the cross-section becomes significant and the  $W^+W^-$  event selections have high efficiencies to select  $H^0$  events, particularly for the process  $H^0Z^0 \rightarrow q\bar{q}q\bar{q}$  which would result in a non-negligible background.

### 3 Event Selection

Event selections have been developed to identify efficiently all Standard Model  $W^+W^-$  final states with low acceptance for background processes. The  $W^+W^-$  event selection consists of three distinct parts to select fully leptonic decays,  $W^+W^- \rightarrow \ell^+\nu_\ell\ell'^-\bar{\nu}_{\ell'}$ , semi-leptonic decays,  $W^+W^- \rightarrow q\bar{q}\ell\bar{\nu}_\ell$ , and fully hadronic decays,  $W^+W^- \rightarrow q\bar{q}q\bar{q}$ . To ensure that the selections are mutually exclusive, only events failing the  $W^+W^- \rightarrow \ell^+\nu_\ell\ell'^-\bar{\nu}_{\ell'}$  selection are considered as possible  $W^+W^- \rightarrow q\bar{q}\ell\bar{\nu}_\ell$  candidates and only events failing both the  $W^+W^- \rightarrow \ell^+\nu_\ell\ell'^-\bar{\nu}_{\ell'}$  and  $W^+W^- \rightarrow q\bar{q}\ell\bar{\nu}_\ell$  selections are considered as possible  $W^+W^- \rightarrow q\bar{q}q\bar{q}$  candidates. The fully leptonic and semi-leptonic selections are separated into the individual lepton types giving ten selected final states:  $e^+\nu_e e^-\bar{\nu}_e$ ,  $e^+\nu_e\mu^-\bar{\nu}_\mu$ ,  $e^+\nu_e\tau^-\bar{\nu}_\tau$ ,  $\mu^+\nu_\mu\mu^-\bar{\nu}_\mu$ ,  $\mu^+\nu_\mu\tau^-\bar{\nu}_\tau$ ,  $\tau^+\nu_\tau\tau^-\bar{\nu}_\tau$ ,  $q\bar{q}e\bar{\nu}_e$ ,  $q\bar{q}\mu\bar{\nu}_\mu$ ,  $q\bar{q}\tau\bar{\nu}_\tau$  and  $q\bar{q}q\bar{q}$ . No attempt has been made to identify the flavour composition of the hadronic final states.

The hadronic and semi-leptonic event samples are used to determine the decay width and the mass of the W boson and also to study hadronic event properties of W boson decays. All final states are used in the measurement of the W pair production cross-sections and decay branching fractions. The classification into separate leptonic final states allows the measurement of the W branching ratios with or without the assumption of charged current lepton universality.

---

<sup>3</sup>In this paper, the W pair production diagrams, *i.e.*  $t$ -channel  $\nu_e$  exchange and  $s$ -channel  $Z^0/\gamma$  exchange, are referred to as ‘‘CC03’’, following the notation of [4].

An overview of the event selections is given below. Emphasis is placed on the performance of the selections and, in particular, the systematic uncertainties in the selection efficiencies and accepted background cross-sections. More detailed descriptions of the  $W^+W^- \rightarrow q\bar{q}\ell\bar{\nu}_\ell$  and  $W^+W^- \rightarrow q\bar{q}q\bar{q}$  event selections can be found in the Appendices.

### 3.1 Treatment of Systematic Uncertainties

The KORALW Monte Carlo program (CC03 diagrams only) was used to estimate the efficiencies of each of the selections. Two types of systematic uncertainties in the selection efficiencies have been considered: generator uncertainties and differences between data and the Monte Carlo simulation, including detector simulation. The generator uncertainties were estimated by comparing the efficiencies for four different Monte Carlo generators, KORALW, grc4f, EXCALIBUR and PYTHIA. The uncertainties arising from the beam energy dependence of the selection efficiencies were assessed by comparing PYTHIA samples generated at different beam energies. The dominant uncertainties due to the beam energy dependence arise because the Monte Carlo samples used to evaluate efficiencies were generated at a centre-of-mass energy of 171 GeV rather than 172.12 GeV, the mean energy at which the data were recorded. Similarly, the propagation of uncertainties on  $M_W$  to the selection efficiencies was estimated using samples of PYTHIA events (including detector simulation) generated with different values of  $M_W$ .

For each selection, the four-fermion backgrounds were determined using the grc4f Monte Carlo program. The systematic uncertainties on the four-fermion backgrounds were estimated from the difference between the accepted cross-sections predicted by the grc4f and EXCALIBUR Monte Carlo programs. For both the  $W^+W^- \rightarrow q\bar{q}\ell\bar{\nu}_\ell$  and  $W^+W^- \rightarrow q\bar{q}q\bar{q}$  selections, the dominant systematic uncertainty on the background was due to the modelling of the  $Z^0/\gamma \rightarrow q\bar{q}$  process.

### 3.2 $W^+W^- \rightarrow \ell^+\nu_\ell\ell'^-\bar{\nu}_{\ell'}$ Events

#### 3.2.1 Selection

Approximately 11% of W pair events are expected to decay through the fully leptonic channel. These events may be observed as an acoplanar pair of charged leptons with missing momentum. The selection is sensitive to the six possible classes of observed leptons,  $e^+e^-$ ,  $\mu^+\mu^-$ ,  $\tau^+\tau^-$ ,  $e^\pm\mu^\mp$ ,  $e^\pm\tau^\mp$ ,  $\mu^\pm\tau^\mp$ , which are expected to be produced in the ratio 1:1:1:2:2:2. The main backgrounds are  $e^+e^- \rightarrow Z^0Z^0$ ,  $e^+e^- \rightarrow Z^0e^+e^-$ ,  $e^+e^- \rightarrow We\bar{\nu}_e$ ,  $e^+e^- \rightarrow \tau^+\tau^-$  and  $e^+e^- \rightarrow e^+e^-\ell^+\ell^-$ .

The experimental signature for  $W^+W^- \rightarrow \ell^+\nu_\ell\ell'^-\bar{\nu}_{\ell'}$  events is also the signature for a number of non-Standard Model processes. The selection used to identify  $W^+W^- \rightarrow \ell^+\nu_\ell\ell'^-\bar{\nu}_{\ell'}$  events is based on the general charged lepton pair selection used in the search for anomalous production of lepton pair events with significant missing transverse momentum [27]. A high efficiency for selecting fully leptonic events is obtained by forming the logical “or” of two distinct analyses<sup>4</sup>. The first analysis performs a general selection of events conforming to the acoplanar di-lepton topology. The second consists of several selections, each designed to select a particular di-lepton class. This analysis was optimised to identify events consistent with being  $W^+W^- \rightarrow \ell^+\nu_\ell\ell'^-\bar{\nu}_{\ell'}$ . Both analyses require evidence that a pair of charged leptons has been produced in association with an invisible system

<sup>4</sup>Referred to as Selection I and Selection II in Reference [27]. For Selection I the additional  $W^+W^-$  selection criteria are applied.

that carries away significant transverse momentum. The first analysis simply requires leptonic events with significant missing transverse momentum, whereas the second analysis exploits the kinematics of  $W^+W^- \rightarrow \ell^+\nu_\ell\ell'^-\bar{\nu}_{\ell'}$  events and the flavour mixture of the expected backgrounds. This leads to a complementary acceptance.

From KORALW Monte Carlo studies, 80% of the expected efficiency for  $W^+W^- \rightarrow \ell^+\nu_\ell\ell'^-\bar{\nu}_{\ell'}$  events is common to the two analyses, 6% is exclusive to the first analysis, and 14% to the second. Both analyses have similar efficiencies for  $W^+W^- \rightarrow \ell^+\nu_\ell\ell'^-\bar{\nu}_{\ell'}$  events with two stable leptons, while the second analysis performs significantly better for events with one or two taus.

### 3.2.2 $W^+W^- \rightarrow \ell^+\nu_\ell\ell'^-\bar{\nu}_{\ell'}$ Classification

Selected  $W^+W^- \rightarrow \ell^+\nu_\ell\ell'^-\bar{\nu}_{\ell'}$  candidates are classified as one of the six possible di-lepton combinations according to the electron and muon identification results, the scaled energy of the leptons and the charged track and cluster multiplicity associated with each lepton. Jets are defined using the cone algorithm [28]. Those not identified as either electrons or muons are classified as taus. A small fraction of selected events are expected to be reconstructed with only one jet. These are events where one of the charged leptons is outside the geometric acceptance of the tracking chambers. For these one-jet events, the unobserved lepton is taken to be a muon. For two-jet events, corresponding to most of the selected events, the classification is further elaborated to improve the assignment of secondary electrons and muons from tau decays to the tau class. Identified electrons or muons with energy scaled by the beam energy less than 0.3 are classified as taus. In order to recuperate inefficiencies in the electron and muon identification algorithm, jets failing the electron and muon identification, but with scaled energy greater than 0.5 are reclassified as electrons if  $E/p$  exceeds 0.5 and as muons if  $E/p$  is less than 0.5. Lastly, jets with three or more charged tracks or three or more associated electromagnetic clusters (consistent with three-prong tau decays) are classified as taus.

### 3.2.3 Results and Systematic Errors

A total of eight events is selected by the combined event selection at  $\sqrt{s} = 172$  GeV as  $W^+W^- \rightarrow \ell^+\nu_\ell\ell'^-\bar{\nu}_{\ell'}$  candidates. Seven of the events are common to both analyses, while one event is exclusively selected by the first analysis.

Representative kinematic distributions for the selected events are given in Figure 1, together with the Monte Carlo expectations. Figure 1(a) shows the energy of each charged lepton scaled by the beam energy. Figure 1(b) shows  $\cos\theta_- - \cos\theta_+$ , where  $\theta_-$  and  $\theta_+$  are the polar angles of negatively charged and positively charged leptons respectively. The selected events favour positive values of  $\cos\theta_- - \cos\theta_+$ , as expected for  $W^+W^-$  production. These kinematic distributions are consistent with the Standard Model expectations.

The Monte Carlo selection efficiencies for each di-lepton combination are shown in Table 1. The overall efficiency for selecting  $W^+W^- \rightarrow \ell^+\nu_\ell\ell'^-\bar{\nu}_{\ell'}$  events is determined to be  $(78.3 \pm 0.4 \pm 2.5)\%$ , where the errors are statistical and systematic, respectively. Since events can be rejected on basis of having a significant energy deposit in the forward detectors, a correction factor of 0.99 with a systematic uncertainty of 0.01 has been applied to the selection efficiencies and the background estimate to account for detector occupancy due to off-momentum beam particles. Systematic uncertainties on the efficiency were estimated based on comparisons of the efficiencies for different Monte Carlo models (3.0% for  $e^+\nu_e e^-\bar{\nu}_e$ , 4.5% for  $\tau^+\nu_\tau\tau^-\bar{\nu}_\tau$  and 2.0% for the other fully leptonic final states). The Monte



Carlo models have different implementations of both initial and final state radiation effects and the modelling of tau decays. In addition, systematic errors were assigned to account for data/Monte Carlo agreement (0.8%) and the knowledge of the trigger efficiency (0.4%).

The expected background cross-sections from Standard Model processes are given in Table 2. The systematic errors are based on comparisons of different Monte Carlo generators. Table 3 lists the expected and observed numbers of events in each final state. The 8 fully leptonic events observed in the data are consistent with the Standard Model expectation.

### 3.3 $W^+W^- \rightarrow q\bar{q}\ell\bar{\nu}_\ell$ Events

#### 3.3.1 Selection

Semi-leptonic final states,  $W^+W^- \rightarrow q\bar{q}\ell\bar{\nu}_\ell$ , are expected to comprise 44% of  $W^+W^-$  decays.  $W^+W^- \rightarrow q\bar{q}e\bar{\nu}_e$  and  $W^+W^- \rightarrow q\bar{q}\mu\bar{\nu}_\mu$  events are characterised by two well-separated hadronic jets, a high momentum lepton and missing momentum due to the unobserved neutrino. The signature for  $W^+W^- \rightarrow q\bar{q}\tau\bar{\nu}_\tau$  events is two well separated jets from the hadronic W decay and one low multiplicity jet typically consisting of one or three tracks. The expected missing momentum is less well defined due to the additional neutrino(s) from the decay of the tau.

The  $W^+W^- \rightarrow q\bar{q}\ell\bar{\nu}_\ell$  event selection, described in Appendix A, consists of three separate selections, one for each type of semi-leptonic decay. The  $W^+W^- \rightarrow q\bar{q}\tau\bar{\nu}_\tau$  selection is applied only to events which fail the  $W^+W^- \rightarrow q\bar{q}e\bar{\nu}_e$  and  $W^+W^- \rightarrow q\bar{q}\mu\bar{\nu}_\mu$  selections. Each selection proceeds in four stages:

- **Identification of the Candidate Lepton:** The track with the highest probability of being a lepton from either the decay  $W \rightarrow e\bar{\nu}_e$  or  $W \rightarrow \mu\bar{\nu}_\mu$  is identified. The  $W^+W^- \rightarrow q\bar{q}\tau\bar{\nu}_\tau$  selection uses the track (or tracks) most consistent with being from a tau decay from  $W \rightarrow \tau\bar{\nu}_\tau$ .
- **Preselection:** Cuts are applied to the data to reduce the background from  $Z^0/\gamma \rightarrow q\bar{q}$  events.
- **Relative Likelihood Selection:** Relative likelihood selections, based on kinematic variables and the lepton candidate, are used to distinguish signal events ( $W^+W^- \rightarrow q\bar{q}e\bar{\nu}_e$ ,  $W^+W^- \rightarrow q\bar{q}\mu\bar{\nu}_\mu$  and  $W^+W^- \rightarrow q\bar{q}\tau\bar{\nu}_\tau$ ) from  $Z^0/\gamma \rightarrow q\bar{q}$  background events. Events passing the likelihood selection are considered to be  $W^+W^- \rightarrow q\bar{q}\ell\bar{\nu}_\ell$  candidates.
- **Event Categorisation:** Having suppressed the background using the relative likelihood selection, a second relative likelihood is applied to the  $W^+W^- \rightarrow q\bar{q}e\bar{\nu}_e$  and  $W^+W^- \rightarrow q\bar{q}\mu\bar{\nu}_\mu$  candidates in order to categorise them as either  $W^+W^- \rightarrow q\bar{q}e\bar{\nu}_e$ ,  $W^+W^- \rightarrow q\bar{q}\mu\bar{\nu}_\mu$  or  $W^+W^- \rightarrow q\bar{q}\tau\bar{\nu}_\tau$  events.

#### 3.3.2 Results and Systematic Errors

Table 4 shows the efficiencies of the selections for  $W^+W^- \rightarrow q\bar{q}\ell\bar{\nu}_\ell$  events after categorisation into the different channels. These efficiencies include corrections which account for observed differences between the data and the Monte Carlo simulation. The uncertainties include both systematic and statistical contributions.

Table 5 lists the sources of the uncertainties evaluated for the selection efficiencies. The respective efficiencies of the  $W^+W^- \rightarrow q\bar{q}e\bar{\nu}_e$ ,  $W^+W^- \rightarrow q\bar{q}\mu\bar{\nu}_\mu$  and  $W^+W^- \rightarrow q\bar{q}\tau\bar{\nu}_\tau$  selections determined from PYTHIA, KORALW, EXCALIBUR and grc4f are found to be consistent within errors. Efficiency corrections and systematic errors arising from discrepancies between data and Monte Carlo simulation were determined by studying data and Monte Carlo “mixed events” formed by superimposing LEP1 hadronic  $Z^0$  decay events and single hemispheres from LEP1 events identified as  $Z^0$  decays to charged lepton pairs. Overall corrections to the efficiencies of  $0.987 \pm 0.006$ ,  $0.999 \pm 0.004$  and  $1.025 \pm 0.007$  were found for the  $W^+W^- \rightarrow q\bar{q}e\bar{\nu}_e$ ,  $W^+W^- \rightarrow q\bar{q}\mu\bar{\nu}_\mu$  and  $W^+W^- \rightarrow q\bar{q}\tau\bar{\nu}_\tau$  selections respectively. The differences between data and Monte Carlo result in a migration of events from the  $W^+W^- \rightarrow q\bar{q}e\bar{\nu}_e$  selection to the  $W^+W^- \rightarrow q\bar{q}\tau\bar{\nu}_\tau$  selection. The main difference arises from the simulation of the electron identification variables used in the relative likelihoods. The efficiencies summarised in Table 4 include these corrections.

Table 6 shows the corrected background cross-sections and total uncertainties for the three selections. The systematic errors on the expected background cross-sections are dominated by differences between data and Monte Carlo for the two-fermion backgrounds and by differences between generators in the case of the four-fermion backgrounds.

The  $W^+W^- \rightarrow q\bar{q}l\bar{\nu}_l$  selection efficiency for  $Z^0/\gamma \rightarrow q\bar{q}$  events is small,  $\sim 0.1\%$ . The background estimate from HERWIG is consistent with that from PYTHIA. Since the efficiency is very low, the Monte Carlo estimate of the background level from this source is likely to be sensitive to the simulation of the tails of distributions. For this reason, the  $Z^0/\gamma \rightarrow q\bar{q}$  background is estimated from the data. The background was found to be  $1.2 \pm 0.5$  times that predicted by the Monte Carlo. This was determined by fitting the observed likelihood distribution in the region 0.25–0.75, for all data recorded away from the  $Z^0$  peak (130–140 GeV, 161 GeV and 172 GeV), with signal and background components where the shapes of the respective likelihood distributions are taken from Monte Carlo. The quoted error includes a systematic component arising from the variation of the fit region.

Four-fermion backgrounds were estimated using the grc4f generator. Differences between the four-fermion background predictions of the grc4f and EXCALIBUR generators were used to assign systematic uncertainties. The W boson pair production cross-section for  $q\bar{q}e\bar{\nu}_e$  was compared with that from the full four-fermion treatment and the difference in the accepted cross-sections taken as the effective background. This is important since the background from  $e^+e^- \rightarrow We\bar{\nu}_e$  can interfere with  $W^+W^- \rightarrow q\bar{q}e\bar{\nu}_e$ . Generator level (*i.e.* without detector simulation) studies using EXCALIBUR indicated that the contributions from non-CC03 diagrams for the  $q\bar{q}\mu\bar{\nu}_\mu$  and  $q\bar{q}\tau\bar{\nu}_\tau$  final states are negligible for the experimental acceptance. Two-photon backgrounds are included in the  $e^+e^-f\bar{f}$  four-fermion background. For the two-photon background and each class of four-fermion background at least two independent Monte Carlo determinations were used and differences between the predicted background cross-sections taken as systematic uncertainties.

In the 172 GeV data sample 19  $W^+W^- \rightarrow q\bar{q}e\bar{\nu}_e$  events, 16  $W^+W^- \rightarrow q\bar{q}\mu\bar{\nu}_\mu$  events and 20  $W^+W^- \rightarrow q\bar{q}\tau\bar{\nu}_\tau$  events were observed in agreement with the expectation shown in Table 3. Figure 2 shows the distribution of lepton energy for accepted events categorised as  $W^+W^- \rightarrow q\bar{q}e\bar{\nu}_e$  and  $W^+W^- \rightarrow q\bar{q}\mu\bar{\nu}_\mu$ . Figure 3 shows four example distributions for selected  $W^+W^- \rightarrow q\bar{q}\tau\bar{\nu}_\tau$  events. The observed distributions for the data are in good agreement with the Monte Carlo expectations.

### 3.4 $W^+W^- \rightarrow q\bar{q}q\bar{q}$ Events

### 3.4.1 Selection

Fully hadronic decays,  $W^+W^- \rightarrow q\bar{q}q\bar{q}$ , which are expected to comprise 46% of the total  $W^+W^-$  cross-section, are characterised by four energetic, hadronic jets and little missing energy. A selection, described in Appendix B, consisting of preselection cuts and a likelihood analysis is used to separate  $W^+W^- \rightarrow q\bar{q}q\bar{q}$  events from the background. The preselection removes events which are likely to be from the process  $Z^0/\gamma \rightarrow q\bar{q}$ . A relative likelihood for an event being from the process  $W^+W^- \rightarrow q\bar{q}q\bar{q}$  rather than from the dominant  $Z^0/\gamma$  background is then estimated using seven kinematic variables. For the selection used in the determination of the mass of the W boson and the studies of  $W^+W^-$  event properties a cut is placed on the value of the relative likelihood. The relative likelihood selection is designed to maximise the product of efficiency and purity while limiting possible distortion of the W mass spectrum.

### 3.4.2 Event Weights

A modified version of the above relative likelihood is used to give a weight,  $w_i$ , to each event reflecting the probability that the event originates from a  $W^+W^- \rightarrow q\bar{q}q\bar{q}$  decay. These event weights, described in more detail in Appendix B.3, are used to reduce the statistical uncertainty on the cross-section measurement. Given the expected average event weights for both  $W^+W^- \rightarrow q\bar{q}q\bar{q}$  and background events,  $\overline{w}_s$  and  $\overline{w}_b$ , the measured  $W^+W^- \rightarrow q\bar{q}q\bar{q}$  cross-section, for an integrated luminosity,  $L$ , can be expressed as

$$\frac{\sum_i w_i - L\sigma_{\text{bgd}}^{\text{pre}}\overline{w}_b}{L\epsilon_{\text{sig}}^{\text{pre}}\overline{w}_s},$$

where the summation over  $i$  corresponds to summing the weights for the observed events which pass the preselection,  $\epsilon_{\text{sig}}^{\text{pre}}$  is the efficiency of the preselection for  $W^+W^- \rightarrow q\bar{q}q\bar{q}$  and  $\sigma_{\text{bgd}}^{\text{pre}}$  is the accepted background cross-section after the preselection. The use of event weights results in a 5% reduction of the expected statistical uncertainty on the measured  $W^+W^- \rightarrow q\bar{q}q\bar{q}$  cross-section.

### 3.4.3 Results and Systematic Errors

The efficiency of the likelihood selection for  $W^+W^- \rightarrow q\bar{q}q\bar{q}$  events is estimated from the KORALW Monte Carlo simulation to be  $(79.8 \pm 0.2 \pm 1.2)\%$ , where the errors are statistical and systematic respectively. The total expected background cross-section,  $\sigma_{\text{bgd}}$ , and the contributions from different processes are given in Table 7. Also shown is the weighted background cross-section which is the expected sum of the event weights for background events passing the preselection. For the event weight method, the other parameters necessary to determine the cross-section are the preselection efficiency for  $W^+W^- \rightarrow q\bar{q}q\bar{q}$  events,  $\epsilon_{\text{sig}}^{\text{pre}} = (90.3 \pm 0.1)\%$ , and the average event weight for  $W^+W^- \rightarrow q\bar{q}q\bar{q}$  events which pass the preselection,  $\overline{w}_s = 0.778 \pm 0.001$ , where the errors are statistical.

The systematic uncertainties evaluated for the  $W^+W^- \rightarrow q\bar{q}q\bar{q}$  selection efficiency are given in Table 8. This table shows uncertainties on the efficiencies and backgrounds for both the likelihood cut selection and for the event weight method. The main systematic uncertainty arises from the QCD modelling of both the  $W^+W^- \rightarrow q\bar{q}q\bar{q}$  process and the dominant background from  $Z^0/\gamma \rightarrow q\bar{q}$ . The likelihood function has been re-evaluated using an alternative QCD Monte Carlo model (HERWIG) and by varying the parameters  $\sigma_q$ ,  $b$ ,  $\Lambda_{QCD}$  and  $Q_0$  of the PYTHIA Monte Carlo by  $\pm$  one standard deviation about their tuned values [29]. The Monte Carlo distributions used for the likelihood probabilities were

rescaled so that the means of the distributions agreed with those observed in the 172 GeV data and the analysis repeated. The numbers of LEP1 data and Monte Carlo events passing the selection, with a modified preselection, were compared. The selection was compared for Monte Carlo events generated at different beam energies and with different W masses. Finally the effect of rebinning the distributions in the likelihood probability calculation was investigated. The differences observed in each case are taken as systematic errors.

The estimated signal efficiency and expected background cross-section are used to determine the expected numbers of signal and background events in Table 9. The observed numbers for the preselection, the likelihood cut and the summed event weight are consistent with the expectations. The statistical error on the observed summed event weight is calculated as the square root of the sum of the squares of the weights for the events passing the preselection.

## 4 $W^+W^-$ Cross-Section and the W Decay Branching Fractions

### 4.1 172 GeV Results

The observed numbers of selected  $W^+W^-$  events have been used to measure the  $W^+W^-$  production cross-section and the W decay branching fractions to leptons and hadrons. The measured cross-section corresponds to that of W pair production from the CC03 diagrams. Additional diagrams can result in the same four-fermion final states as produced in the decays of  $W^+W^-$  and can therefore interfere. When calculating the expected non-CC03 backgrounds for the various event selections the effects of this interference have been included. The expected four-fermion backgrounds, quoted throughout this paper, include both contributions from non-CC03 diagrams and the effects of interference. The four-fermion backgrounds for each final state are calculated from the difference between the accepted four-fermion cross-section including all diagrams, and the accepted CC03 cross-section. For this determination the grc4f Monte Carlo was used. The associated systematic uncertainty is estimated by comparing the predictions of grc4f and EXCALIBUR. At the current level of statistical precision such interference effects are small, but not negligible, for the experimental acceptance. In making the measurement, Standard Model expectations for four-fermion processes are used.

This division into CC03  $W^+W^-$  events and background events is shown in Table 3, for a W mass of 80.33 GeV [1, 2] and a centre-of-mass energy of 172.12 GeV. The data are consistent with the Monte Carlo expectation. The systematic uncertainties on the expected numbers of signal events include contributions from the current errors of  $\pm 0.15$  GeV [1, 2] on  $M_W$  and  $\pm 0.03$  GeV on the beam energy [13] (0.9% and 0.2%, respectively). A  $W^+W^-$  cross-section of 12.4 pb predicted by GENTLE was used, with a theoretical uncertainty of  $\pm 2\%$ . Uncertainties in the selection efficiencies, accepted background cross-sections and luminosity have been given in Sections 2.2–3.4.

The  $W^+W^-$  cross-section and branching fractions are measured using the information from the ten separate channels. For each of the ten final states,  $i$ , the probability of obtaining the number of observed events is calculated as a function of the  $W^+W^-$  cross-section,  $\sigma_{WW}$ , and the W branching fractions. A likelihood  $\mathcal{L}$  is formed from the product of these Poisson probabilities,  $\mathcal{P}_i$ , of observing  $N_i$  events for a Monte Carlo prediction of  $\mu_i$  events:

$$\mathcal{L} = \prod_i \mathcal{P}_i(N_i, \mu_i) = \prod_i \frac{\mu_i^{N_i} e^{-\mu_i}}{N_i!}.$$

For the  $W^+W^- \rightarrow q\bar{q}q\bar{q}$  selection the likelihood is calculated using the summed event weights for the 99 preselected events with a Gaussian error of  $\pm 6.6$  corresponding to the square root of the sum of the

squared event weights. The expected number of events in each of the ten channels,  $\mu_i$ , can be expressed in terms of the luminosity, the total (CC03) cross-section at  $\sqrt{s}$  of 172.12 GeV,  $\sigma_{\text{WW}}(172 \text{ GeV})$ , the W boson branching fractions,  $\text{Br}(W \rightarrow X)$ , the background cross-section in each channel and the efficiency matrix for the  $W^+W^-$  selections,  $\epsilon_{ij}$ . The entries in the matrix,  $\epsilon_{ij}$ , shown in Table 10, are the efficiencies of the event selections  $i$  for a  $W^+W^-$  decay of type  $j$ . The off-diagonal elements of the matrix determine the acceptances of each selection for other  $W^+W^-$  decays.

Three different maximum likelihood fits have been performed. In the first case  $\sigma_{\text{WW}}(172 \text{ GeV})$ ,  $\text{Br}(W \rightarrow e\bar{\nu}_e)$ ,  $\text{Br}(W \rightarrow \mu\bar{\nu}_\mu)$  and  $\text{Br}(W \rightarrow \tau\bar{\nu}_\tau)$  are extracted under the assumption that

$$\text{Br}(W \rightarrow e\bar{\nu}_e) + \text{Br}(W \rightarrow \mu\bar{\nu}_\mu) + \text{Br}(W \rightarrow \tau\bar{\nu}_\tau) + \text{Br}(W \rightarrow q\bar{q}) = 1,$$

giving:

$$\begin{aligned} \text{Br}(W \rightarrow e\bar{\nu}_e) &= 0.107_{-0.022}^{+0.025} \pm 0.004, \\ \text{Br}(W \rightarrow \mu\bar{\nu}_\mu) &= 0.076_{-0.019}^{+0.021} \pm 0.003, \\ \text{Br}(W \rightarrow \tau\bar{\nu}_\tau) &= 0.128_{-0.029}^{+0.032} \pm 0.005, \\ \sigma_{\text{WW}}(172 \text{ GeV}) &= 12.5 \pm 1.3 \pm 0.4 \text{ pb}, \end{aligned}$$

where the first uncertainty is statistical and the second systematic. The systematic error includes contributions from the uncertainties in the efficiency, background cross-section and luminosity. The largest systematic error arises from the uncertainty in the backgrounds in the  $W^+W^-$  selections. The correlations between the above measurements are less than 30%. In the second fit the additional constraint of charged current lepton universality is imposed<sup>5</sup>:

$$\text{Br}(W \rightarrow e\bar{\nu}_e) = \text{Br}(W \rightarrow \mu\bar{\nu}_\mu) = \text{Br}(W \rightarrow \tau\bar{\nu}_\tau) = \text{Br}(W \rightarrow \ell\bar{\nu}_\ell),$$

giving

$$\begin{aligned} \text{Br}(W \rightarrow \ell\bar{\nu}_\ell) &= 0.102_{-0.011}^{+0.012} \pm 0.003, \\ \sigma_{\text{WW}}(172 \text{ GeV}) &= 12.3 \pm 1.3 \pm 0.4 \text{ pb}. \end{aligned}$$

This value for  $\text{Br}(W \rightarrow \ell\bar{\nu}_\ell)$  implies a value for the hadronic branching fraction,  $\text{Br}(W \rightarrow q\bar{q})$ , of

$$\text{Br}(W \rightarrow q\bar{q}) = 0.694_{-0.035}^{+0.033} \pm 0.008.$$

In the final fit, the branching fractions are fixed to their Standard Model values and the CC03 cross-section is determined to be

$$\sigma_{\text{WW}}(172 \text{ GeV}) = 12.3 \pm 1.3 \pm 0.3 \text{ pb}.$$

The CC03 cross-section at 172.12 GeV depends, albeit weakly, on the W mass. Therefore the measured cross-section,  $\sigma_{\text{WW}}(172 \text{ GeV})$ , can be used to obtain a measurement of  $M_W$ :

$$M_W = 80.5_{-2.2-0.6}^{+1.4+0.5} \text{ GeV},$$

where the first uncertainty is statistical and the second is systematic. The latter uncertainty includes a 2% theoretical component. The result of the fit using the Standard Model branching fractions is consistent with that obtained by taking the total number of observed events divided by the luminosity, subtracting the total expected background cross-section and dividing by the overall effective selection

---

<sup>5</sup>For the current level of experimental precision, the effect of  $\text{Br}(W \rightarrow \tau\bar{\nu}_\tau)$  being  $\sim 0.1\%$  lower [4] than  $\text{Br}(W \rightarrow e\bar{\nu}_e)$  and  $\text{Br}(W \rightarrow \mu\bar{\nu}_\mu)$  has been neglected.

efficiency of  $(77.4 \pm 1.0)\%$ . This gives  $\sigma_{\text{WW}} = 12.3_{-1.3}^{+1.4}$  pb, where the error is the combined statistical and systematic uncertainty.

The measured  $W^+W^-$  production cross-section at  $\sqrt{s} = 172.12$  GeV is shown in Figure 4, together with the recent OPAL measurement of  $\sigma_{\text{WW}}$  at  $\sqrt{s} = 161.3$  GeV [5]. The energy dependence of the  $W^+W^-$  production cross-section, as predicted by the GENTLE program for a representative W mass of 80.33 GeV [1, 2], is also given in the figure. The data are seen to be consistent with the Standard Model expectation.

## 4.2 Combination with 161 GeV Results

The branching fraction results from the 172.12 GeV data can be combined with the OPAL data recorded at 161.3 GeV [5]. Simultaneous fits to the CC03 cross-section at 161.3 GeV,  $\sigma_{\text{WW}}(161 \text{ GeV})$ , the CC03 cross-section at 172.12 GeV and the W boson branching fractions are performed in the same way as presented above for the 172.12 GeV data. The event selections, efficiencies, backgrounds and observed numbers of events for the 161.3 GeV data have been described previously [5]. The results of this combination are summarised in Table 11.

Within the framework of the Standard Model, the W boson branching fractions depend on the six elements of the CKM mixing matrix,  $|V_{ij}|$ , which do not involve the top quark [4]

$$\frac{\text{Br}(W \rightarrow q\bar{q})}{(1 - \text{Br}(W \rightarrow q\bar{q}))} = \left(1 + \frac{\alpha_s(M_W)}{\pi}\right) \sum_{i=u,c; j=d,s,b} |V_{ij}|^2,$$

where  $\alpha_s(M_W)$  is taken to be  $0.120 \pm 0.005$ . The effect of finite quark masses,  $m_q$ , on the W branching ratios are of order  $(m_q/M_W)^2$  [4], and are therefore neglected. The result, given in Table 11, for the branching fraction  $\text{Br}(W \rightarrow q\bar{q})$  obtained from the fit assuming lepton universality gives:

$$\sum_{i=u,c; j=d,s,b} |V_{ij}|^2 = 2.22_{-0.34}^{+0.32} \pm 0.07.$$

This is consistent with a value of 2 which is expected from unitarity. Using the experimental knowledge [1] of the sum,  $|V_{ud}|^2 + |V_{us}|^2 + |V_{ub}|^2 + |V_{cd}|^2 + |V_{cb}|^2 = 1.05 \pm 0.01$ , the above result can be interpreted as a measure of  $|V_{cs}|$ , the least well determined of these elements:

$$|V_{cs}| = 1.08_{-0.16}^{+0.15} \pm 0.03.$$

This result is consistent in value with and has a comparable uncertainty to other determinations of  $|V_{cs}|$  which do not invoke unitarity [1, 30].

## 5 Measurement of the Mass and the Decay Width of the W Boson

The W boson mass,  $M_W$ , and decay width,  $\Gamma_W$ , are determined from fits to the reconstructed invariant mass spectrum of W pair candidate events. A kinematic fit is employed to improve the mass resolution for the  $W^+W^- \rightarrow q\bar{q}q\bar{q}$  and  $W^+W^- \rightarrow q\bar{q}\ell\bar{\nu}_\ell$  channels. The fully leptonic final state is underconstrained as it contains at least two neutrinos and is therefore not used. Two different methods are used to fit the reconstructed mass distribution. In the first,  $M_W$  is determined by performing an unbinned likelihood fit which uses a Breit-Wigner function to describe the signal shape. Monte

Carlo events are used to correct the fit result for biases introduced by the event selection, detector resolution and effects of initial state radiation (ISR). In the second method, a reweighting technique is employed to produce Monte Carlo mass spectra, including detector simulation, corresponding to any given mass and width. A binned likelihood fit is used to determine  $M_W$  and  $\Gamma_W$  by comparing the shape of the reconstructed mass distribution from the data to that from the reweighted Monte Carlo spectra. This method takes into account all resolution, acceptance and ISR effects and is free of bias as long as these effects are simulated correctly. In addition, the extension from a one-parameter fit determining  $M_W$  to a two-parameter fit determining both  $M_W$  and  $\Gamma_W$  is straightforward. Therefore, the reweighting method (RW) is used to derive the central results of this paper for  $M_W$  and  $\Gamma_W$ . The simpler Breit-Wigner fit (BW) provides a valuable cross-check of the RW results and systematics. By appropriately choosing the fit normalisations, both methods are made independent of cross-section information and are sensitive only to the shape of the reconstructed mass spectrum.

## 5.1 Invariant Mass Reconstruction

For each selected  $W^+W^-$  event, the masses of the two W bosons can be determined from measured invariant masses of the decay products. Incorporating the constraints of energy and momentum conservation into a kinematic fit significantly improves the invariant mass resolution. The resolution of the kinematic fit is further improved by neglecting the finite W width event-by-event, and constraining the masses of the two W boson candidates to be equal, thus yielding a single reconstructed invariant mass per event,  $m_{\text{rec}}$ . For  $W^+W^-$  events,  $m_{\text{rec}}$  is strongly correlated to the average mass of the two W bosons in the event<sup>6</sup>. Incorporating the measured jet masses into the kinematic fit, rather than treating jets as massless, gives an improved mass resolution and yields a better agreement between the reconstructed and average masses. Cuts on the fit probability remove poorly reconstructed events and reduce background. In addition, there is an ambiguity in the choice of the correct jet-jet pairing in  $W^+W^- \rightarrow q\bar{q}q\bar{q}$  events which leads to a combinatorial background.

### 5.1.1 The $W^+W^- \rightarrow q\bar{q}q\bar{q}$ Channel

In each selected  $W^+W^- \rightarrow q\bar{q}q\bar{q}$  event, four jets are defined using the Durham algorithm [31]. These jets are used as input to a five-constraint kinematic fit requiring energy and momentum conservation and equality of the two W boson masses. For each event, three kinematic fits are performed, corresponding to the three possible jet-jet pairings, and placed in descending order of the resulting fit probabilities  $P_1$ ,  $P_2$ ,  $P_3$ . In Monte Carlo studies, the highest fit probability,  $P_1$ , corresponds to the correct jet-jet pairing in about 68% of  $W^+W^- \rightarrow q\bar{q}q\bar{q}$  events. In approximately 25% of events the second highest probability fit,  $P_2$ , corresponds to the correct combination. The lowest probability fit is dominated by incorrect combinations and is not used. Both fit methods require  $P_1 > 0.01$ . In the BW method, the second fit is also included in the reconstructed mass distribution if  $P_2 > 0.01$  and if  $P_2/P_1 > 1/3$ . This prescription is adopted to optimise the ratio of signal to background. In the RW method, for events in which both  $P_1$  and  $P_2$  exceed 0.01, a two-dimensional distribution,  $(M_1, M_2)$  is used, where  $M_i$  is the reconstructed mass corresponding to the combination having fit probability  $P_i$ . For those events in which only  $P_1$  exceeds 0.01, a one-dimensional spectrum is used. The numbers of selected events used in the mass analyses are listed in Table 12 for the fit ranges discussed in Sections 5.2 and 5.3.

---

<sup>6</sup>At the generator level, the distribution of the average mass of the two W bosons is described by the same Breit-Wigner function as the distribution of the two separate W masses, multiplied by a phase space factor.

### 5.1.2 The $W^+W^- \rightarrow q\bar{q}\ell\bar{\nu}_\ell$ Channel

For the selected  $W^+W^- \rightarrow q\bar{q}\ell\bar{\nu}_\ell$  candidate events ( $\ell = e$  or  $\mu$ ), the reconstructed mass is estimated by defining two jets in the hadronic system and then performing a kinematic fit, including the jets and lepton, using the same constraints as for the  $W^+W^- \rightarrow q\bar{q}q\bar{q}$  channel. Since the three-momentum of the neutrino is not known, this results in a two-constraint fit. Events with fit probability greater than 0.001 are retained for the analysis. The probability cut is lower than for the  $W^+W^- \rightarrow q\bar{q}q\bar{q}$  channel because the semi-leptonic channels have less background. In the case of the  $W^+W^- \rightarrow q\bar{q}\tau\bar{\nu}_\tau$  channel, the energy of the visible tau decay products is often a poor estimate of the tau lepton energy because of the presence of additional neutrinos in the tau decay. To account for this in a kinematic fit, the direction of the tau lepton is taken to be that of the identified tau jet and the energy of the tau lepton is set to half the beam energy, with an error large enough to cover the kinematically allowed range. However, Monte Carlo studies show that the mass resolution of this fit is not significantly better than that obtained by dividing the invariant mass of the hadronic system by the ratio of the visible energy of the hadronic system to the beam energy. Furthermore, the fit introduces more bias and therefore both the BW and the RW method use the reconstructed mass as determined by the scaling method for the  $W^+W^- \rightarrow q\bar{q}\tau\bar{\nu}_\tau$  channel. To reduce background and remove poorly reconstructed events, the BW method requires that the kinematic fit probability be greater than 0.01 for  $W^+W^- \rightarrow q\bar{q}\tau\bar{\nu}_\tau$  events. The numbers of selected events in these channels are listed in Table 12.

## 5.2 Breit-Wigner Fit to the Reconstructed Invariant Mass Spectrum

The first method used to determine the W mass involves fitting an analytic function to the distribution of the masses obtained from the kinematic fit. Because of biases introduced by event selection, detector resolution, ISR, and phase-space effects, the method has been calibrated by performing similar fits to Monte Carlo samples generated with known W masses.

### 5.2.1 Signal Shape

A variety of analytic forms to describe the signal and background shapes were investigated. From Monte Carlo studies the signal shape is found to be well described up to  $m_{\text{rec}} \sim 84$  GeV by a function based on a relativistic Breit-Wigner function with fixed width,

$$S(m_{\text{rec}}) = \frac{m_{\text{rec}}^2 \Gamma^2}{(m_{\text{rec}}^2 - m_0^2)^2 + m_{\text{rec}}^2 \Gamma^2},$$

where  $m_0$  and  $\Gamma$  are characteristic parameters of the signal peak. The fits are limited to the range 40–84 GeV, where the lower boundary is determined by considerations regarding the background normalisation and is discussed below. The width,  $\Gamma$ , should be regarded as a parameter which embodies both the width of the W boson and experimental effects and is fixed to the value predicted by the Monte Carlo, 3.8 GeV.

### 5.2.2 Background Shape

Background arises mainly in the  $W^+W^- \rightarrow q\bar{q}q\bar{q}$  channel, both from  $Z^0/\gamma \rightarrow q\bar{q}$  events, and from incorrect combinations in  $W^+W^- \rightarrow q\bar{q}q\bar{q}$  events. Monte Carlo studies show that a quadratic form in  $m_{\text{rec}}$  describes the combinatorial background well up to  $m_{\text{rec}} \sim 84$  GeV. The  $Z^0/\gamma \rightarrow q\bar{q}$  background



has a different shape. It was found that this can be described by the function  $Ap^\alpha e^{-\beta p}$ , where  $p = \sqrt{E_{\text{beam}}^2 - m_{\text{rec}}^2}$  is the momentum with which a W pair of mass  $m_{\text{rec}}$  would have been produced and where  $\alpha$  and  $\beta$  are positive parameters. The shapes and relative normalisation of the background contributions are determined from Monte Carlo samples, but their overall normalisation is allowed to vary in the fit. Extending the allowed fit range down to 40 GeV improves the determination of the background fraction in the peak region, as this low mass region is dominated by background.

### 5.2.3 Results of the Breit-Wigner Fit Method

To extract  $M_W$  from the reconstructed mass distribution, an unbinned maximum likelihood fit to a relativistic Breit-Wigner plus background function is used. The fit is performed using the reconstructed mass distribution from all channels combined. For comparison, it is also performed on the  $W^+W^- \rightarrow q\bar{q}q\bar{q}$  and  $W^+W^- \rightarrow q\bar{q}\ell\bar{\nu}_\ell$  channels separately<sup>7</sup>. The fit results are given in Table 13, and compared with the data in Figure 5. The expected statistical error has been studied using independent subsamples of Monte Carlo events corresponding to the same integrated luminosity as the data. These studies demonstrate that the error returned by the fit accurately reflects the r.m.s. spread of the  $m_0$  distribution.

The correction for bias in the BW method is estimated using PYTHIA Monte Carlo events corresponding to various input values of  $M_W$  and the beam energy,  $E_{\text{beam}}$ . Small samples of Monte Carlo signal and background events corresponding to the integrated luminosity of the data are processed through the same event selection, mass reconstruction, and fitting routines as the data. The mean correction is determined by fitting a Gaussian to the resulting distribution of  $(m_0^{\text{fit}} - m_W^{\text{true}})$  where  $m_W^{\text{true}}$  is the W boson mass with which the Monte Carlo sample is generated. This correction is found to depend linearly on  $(E_{\text{beam}} - m_W^{\text{true}})$ , as shown in Figure 6. A straight line fit yields:

$$\begin{aligned} W^+W^- \rightarrow q\bar{q}q\bar{q} : \quad m_0^{\text{fit}} - m_W^{\text{true}} &= -0.363 + 0.0911(E_{\text{beam}} - m_W^{\text{true}}) \\ W^+W^- \rightarrow q\bar{q}\ell\bar{\nu}_\ell : \quad m_0^{\text{fit}} - m_W^{\text{true}} &= -0.107 + 0.0768(E_{\text{beam}} - m_W^{\text{true}}) \\ \text{Combined} : \quad m_0^{\text{fit}} - m_W^{\text{true}} &= -0.193 + 0.0779(E_{\text{beam}} - m_W^{\text{true}}) \end{aligned}$$

with the masses and energies expressed in GeV. These relations are used to correct the fitted mass for all biases. The fitted masses, corrections and corrected masses are given in Table 13.

## 5.3 Fit to the Reconstructed Mass Spectrum using a Reweighting Method

In the second method, the W boson mass and width are extracted by directly comparing the reconstructed mass distribution of the data to mass spectra estimated from fully simulated Monte Carlo events corresponding to various values of  $M_W$  and  $\Gamma_W$ . A likelihood fit is used to extract  $M_W$  and  $\Gamma_W$  by determining which Monte Carlo spectrum gives the best description of the data. In order to obtain the Monte Carlo spectrum for arbitrary values of  $M_W$  and  $\Gamma_W$ , a Monte Carlo reweighting technique is employed.

### 5.3.1 The Monte Carlo Reweighting Technique

For a sample of CC03 W pair Monte Carlo events produced with a given mass and width,  $(M_W^{\text{MC}}, \Gamma_W^{\text{MC}})$ , the detector level mass spectrum corresponding to a different mass and width,  $(M_W^{\text{new}}, \Gamma_W^{\text{new}})$ ,

<sup>7</sup>The widths are fixed to different values in the two channels.

is estimated by assigning to each event a reweighting factor with which it enters the new spectrum. This factor is the ratio of the probability that the event would be produced assuming the new values of  $(M_W^{\text{new}}, \Gamma_W^{\text{new}})$  to the probability that this same event would be produced for the input values  $(M_W^{\text{MC}}, \Gamma_W^{\text{MC}})$ . These production probabilities are given by the W pair production cross-section [32]

$$P(M_W, \Gamma_W; m_1, m_2) \propto \mathcal{BW}(M_W, \Gamma_W; m_1) \mathcal{BW}(M_W, \Gamma_W; m_2) \sigma_0(m_1, m_2, s),$$

where  $m_1$  and  $m_2$  are the generator level masses of the two W bosons produced in the event and  $\sigma_0$  is the Born level cross-section for producing a pair of W bosons with masses  $(m_1, m_2)$  at a centre-of-mass energy  $\sqrt{s}$ . The values  $m_1$  and  $m_2$  are distributed according to the running-width, relativistic Breit-Wigner function,

$$\mathcal{BW}(M_W, \Gamma_W; m) = \frac{1}{\pi} \frac{\frac{m^2}{M_W} \Gamma_W}{(m^2 - M_W^2)^2 + \frac{m^4}{M_W^2} \Gamma_W^2}.$$

The reweighting factor for the  $i$ th event,  $f_i$ , is then given by

$$f_i = \frac{\mathcal{BW}(M_W^{\text{new}}, \Gamma_W^{\text{new}}; m_1^i) \mathcal{BW}(M_W^{\text{new}}, \Gamma_W^{\text{new}}; m_2^i)}{\mathcal{BW}(M_W^{\text{MC}}, \Gamma_W^{\text{MC}}; m_1^i) \mathcal{BW}(M_W^{\text{MC}}, \Gamma_W^{\text{MC}}; m_2^i)}.$$

The Born level cross-section cancels in the ratio since it depends only on  $m_1$ ,  $m_2$  and  $\sqrt{s}$ .

An estimate of the detector level reconstructed mass spectrum for any  $(M_W^{\text{new}}, \Gamma_W^{\text{new}})$  can be obtained from one such sample alone with a given input  $(M_W^{\text{MC}}, \Gamma_W^{\text{MC}})$ . In general, deviations from unity in the reweighting factors increase as  $M_W^{\text{new}}$  and  $\Gamma_W^{\text{new}}$  differ from  $M_W^{\text{MC}}$  and  $\Gamma_W^{\text{MC}}$ , respectively. For very large  $f_i$ , the reweighted spectrum becomes sensitive to statistical fluctuations in the input sample. To reduce the sensitivity to large reweighting factors, a total of 850 000 events from all  $W^+W^-$  Monte Carlo samples with full detector simulation are used (PYTHIA, HERWIG, EXCALIBUR, KORALW and grc4f Monte Carlo generators). These samples cover a range of input  $(M_W^{\text{MC}}, \Gamma_W^{\text{MC}})$  values, spanning  $M_W = 78.33$  GeV to  $M_W = 82.33$  GeV and widths of 1.7 GeV to 2.5 GeV. The inclusion of all of these samples ensures that the reweighted spectra are reasonably smooth over a large range of  $(M_W^{\text{new}}, \Gamma_W^{\text{new}})$  values.

### 5.3.2 The Signal and Background Shapes

The normalised reweighted mass spectra of the individual Monte Carlo samples are combined into a single reweighted spectrum by taking the weighted average, bin-by-bin. As an example of the performance of this procedure, Figure 7 compares the reweighted mass distribution for the  $W^+W^- \rightarrow q\bar{q}\ell\nu_\ell$  channel for  $(M_W^{\text{new}}, \Gamma_W^{\text{new}}) = (79.33, 2.047)$  GeV to the spectrum from the fully-simulated PYTHIA MC sample generated with  $(M_W^{\text{MC}}, \Gamma_W^{\text{MC}}) = (79.33, 2.047)$  GeV. Good agreement is found.

The background mass spectra are taken from Monte Carlo and are assumed to be independent of  $M_W$  and  $\Gamma_W$ . The background distributions are normalised to the expected number of background events. The reweighted signal spectra are then normalised such that the total number of signal plus background events corresponds to the observed number of events. This is done separately for each channel. For this purpose, the  $W^+W^- \rightarrow q\bar{q}q\bar{q}$  events in which both the first and second highest probability fits are used are treated as a separate channel from those  $W^+W^- \rightarrow q\bar{q}q\bar{q}$  events in which only the highest probability fit is used.

Most of the Monte Carlo events have been produced for a beam energy of  $E_{\text{beam}}^{\text{MC}} = 85.50$  GeV, whereas the luminosity weighted average beam energy of the data is  $E_{\text{beam}}^{\text{data}} = 86.06$  GeV. In order to

correct for this, the mass  $M_W^{\text{new}}$  used for reweighting is modified to

$$M_W^{\text{new}} \rightarrow M_W^{\text{new}} - (E_{\text{beam}}^{\text{data}} - E_{\text{beam}}^{\text{MC}}),$$

while shifting the resulting spectrum by  $(E_{\text{beam}}^{\text{data}} - E_{\text{beam}}^{\text{MC}})$ . Since not all the fully simulated samples are produced with the same centre-of-mass energy, this is done for each sample separately before combining the reweighted spectra. A corresponding shift is made to the background spectra.

### 5.3.3 Results of the Reweighting Method

A binned likelihood is formed from the product of the Poisson probabilities for obtaining the numbers of events observed in the data in each bin of mass (and width) using the Monte Carlo expectation for  $(M_W, \Gamma_W)$ . The log-likelihood curve is determined separately for each of the different channels. Since the channels are statistically independent, the results are combined by adding together these likelihood curves. The resulting log-likelihood distribution as a function of the mass and the width allows the determination of  $M_W$  and  $\Gamma_W$  and their associated statistical uncertainties.

To reduce further the sensitivity to statistical fluctuations in the determination of the expected number of events, only events with a reconstructed mass in the range  $65 \text{ GeV} < m_{\text{rec}} < E_{\text{beam}}$  are included in the fit. For the two-dimensional mass spectrum of the  $W^+W^- \rightarrow q\bar{q}q\bar{q}$  channel, at least one of the two reconstructed masses is required to be greater than 70 GeV and the sum of the two masses must exceed 120 GeV. The rather limited mass range is further motivated by the fact that events with small reconstructed masses have very little sensitivity to  $M_W$  and  $\Gamma_W$ .

The results of the fit to  $M_W$  and  $\Gamma_W$  using  $W^+W^- \rightarrow q\bar{q}q\bar{q}$  and  $W^+W^- \rightarrow q\bar{q}\ell\bar{\nu}_\ell$  events are:

$$\begin{aligned} M_W &= 80.30 \pm 0.27 \pm 0.09 \text{ GeV}, \\ \Gamma_W &= 1.30_{-0.55}^{+0.62} \pm 0.18 \text{ GeV}, \end{aligned}$$

where the errors are statistical and systematic, respectively. The correlation coefficient between  $M_W$  and  $\Gamma_W$  is 0.06. The systematic errors are discussed in Section 5.4. The mass spectra of the individual channels together with the fitted reweighted spectra are shown in Figure 8. The likelihood contours for the statistical errors are displayed in Figure 9 together with the Standard Model prediction. From the shape of the contours and the asymmetric errors on the width, it can be seen that the errors on  $\Gamma_W$  for the present statistics are non-Gaussian. The two standard deviation errors on  $\Gamma_W$  are  ${}_{-1.21}^{+1.64} \text{ GeV}$ .

A one-parameter fit for the mass is performed by constraining the width using the Standard Model relation [4]

$$\Gamma_W = (2.0817 \text{ GeV}) \frac{M_W^3}{(80.26 \text{ GeV})^3},$$

giving:

$$\begin{aligned} W^+W^- \rightarrow q\bar{q}q\bar{q} : \quad M_W &= 80.08 \pm 0.44 \pm 0.14 \text{ GeV}, \\ W^+W^- \rightarrow q\bar{q}\ell\bar{\nu}_\ell : \quad M_W &= 80.53 \pm 0.41 \pm 0.10 \text{ GeV}, \\ \text{Combined} : \quad M_W &= 80.32 \pm 0.30 \pm 0.09 \text{ GeV}. \end{aligned}$$

The error on the fitted mass is correlated with the width of the reconstructed mass distribution. Consequently, the statistical error on the mass resulting from the one-parameter fit is larger than that

resulting from the two-parameter fit. Since this measurement is principally intended to determine  $M_W$  as a Standard Model parameter, the result of the one-parameter fit is taken as the central result of this paper for the mass of the W boson as determined from the direct reconstruction method. The value of  $M_W$  obtained from the BW fit is consistent with that obtained using the RW method, thus providing a useful cross check of the RW analysis.

## 5.4 Systematic Uncertainties

The main sources of systematic uncertainty on  $M_W$  and  $\Gamma_W$  are studied by changing some feature of the analysis. The effect of this can typically be assessed in two ways – either by repeating the fit to the reconstructed mass spectrum and observing the change in the fit results, or by determining the average of the event-by-event change in the reconstructed mass. The latter method tends to have greater statistical sensitivity, but does not readily yield a determination of the error on  $\Gamma_W$ . For this reason, the former method was generally preferred in the RW analysis, and the latter in the BW analysis. Despite these differences, the overall systematic errors calculated for the two analyses are in good agreement. The following descriptions concentrate on the procedure used to estimate the uncertainty in the RW fit method. The estimated errors are summarised in Table 14.

**Beam Energy:** Uncertainties in the LEP beam energy affect the reconstructed mass spectrum through the energy constraints imposed by the kinematic fit. The precision on the beam energy is estimated to be  $\pm 30$  MeV [13]. The influence of this uncertainty on the fit results has been estimated by changing the beam energy in independent samples of signal and background Monte Carlo before performing the kinematic fits. In addition, the effect of a possible asymmetry between the  $e^+$  and  $e^-$  energies is found to be negligible.

**Initial State Radiation:** The effect of initial state radiation is to increase systematically the reconstructed invariant mass, and consequently the resulting fitted mass, due to biases introduced through the energy conservation constraint of the kinematic fit. This bias is taken into account in both the RW and BW fit methods to the extent that ISR is accurately modelled in the Monte Carlo. The KORALW generator is used to estimate the systematic error associated with the incomplete modelling of ISR for the RW fits. Distributions of the mean<sup>8</sup>  $M_W$  per event are compared in two samples, one including only first order corrections and one including the full second order ISR corrections. From fits to these generator level distributions systematic uncertainties of 20 MeV for the mass and 60 MeV for the width are assigned.

**Hadronisation:** Sensitivity of the results to the choice of the hadronisation model was studied in two ways. In the first approach, a single sample of  $W^+W^-$  four-fermion final states was hadronised separately by both PYTHIA and HERWIG and the fit results compared. By using the same four-fermion final states the comparison is sensitive only to differences in hadronisation. Alternatively, the mean difference between the reconstructed mass and the generator level average mass is determined for the PYTHIA and HERWIG  $W^+W^-$  samples separately. No significant difference is observed in either comparison and the statistical precisions of the tests are taken as the systematic errors. Varying the hadronisation model for the background is found to have a negligible effect.

**Four-fermion Interference Effects:** The Monte Carlo samples used to calibrate the BW method and in the reweighting procedure of the RW method include only the CC03 diagrams. In order

---

<sup>8</sup>At the generator level, the average mass of two W bosons is used as an approximation to the results of the five-constraint kinematic fit at the detector level.

to test the sensitivity of the results to the interference between  $W^+W^-$  diagrams and other four-fermion processes, the fit results of a sample generated including the full set of interfering four-fermion diagrams are compared to one restricted to the CC03  $W^+W^-$  diagrams alone. The comparison is made using both the `grc4f` generator and the `EXCALIBUR` generator. A small mass shift was found when using `EXCALIBUR`, while no such indication was found using `grc4f`. The assigned uncertainties accommodate the results from these two models.

**Detector Effects:** The effects of detector mis-calibrations and deficiencies in the Monte Carlo simulation of the data have been investigated by varying the inputs to the kinematic fit over reasonable ranges. The range is determined in each case from a detailed comparison of data and Monte Carlo using approximately  $1.2 \text{ pb}^{-1}$  of data recorded at  $\sqrt{s} \sim M_Z$  during 1996. The following effects are considered:

- The jet energy scale is determined to be accurate to within 1%. The effect on both data and Monte Carlo reconstructed masses is found to be negligible.
- The calibration of the lepton momentum or energy scale is accurate to within 1%. The corresponding changes for the semi-leptonic ( $e/\mu$ ) channels are taken as systematic errors.
- The results of the kinematic fit depend on the covariance matrix of the input parameters, which have been determined using Monte Carlo events. Studies of  $Z^0$  decays indicate that the jet energy errors in the data are understood to within 3%. No indication of mis-modelling of the errors associated with the jet angles or of the corresponding lepton parameters was found. As an estimate of the associated uncertainty, each parameter of the covariance matrix was varied within its estimated uncertainty.
- The algorithm used to correct jet energies and angles combines information from tracks, and electromagnetic and hadron calorimeter clusters. Three possible variants in the procedure are studied. Firstly, the mass reconstruction is repeated with the hadron calorimeter removed from the analysis. Secondly, an alternative parametrisation of the jet errors is employed. Finally, a different correction algorithm for the combination of track and calorimetric information is used. The standard correction procedure combines all tracks and clusters into jets and then applies an average correction based on parametrisations of the total energy in each detector component contributing to the jet. The alternative algorithm first associates tracks with clusters then subtracts the associated charged particle energy from the individual clusters prior to jet finding. In all of these checks, the mean and r.m.s. of the shifts in the reconstructed masses observed in the data are compatible with the expectations from Monte Carlo. The statistical precision of each comparison is taken as the associated uncertainty, and the largest of these is included in the total systematic error.

The errors from all of these checks are added in quadrature to give the total systematic error due to uncertainties associated with detector mis-calibrations and mis-modelling. This is the dominant experimental systematic uncertainty.

**Fitting Procedure and Background Treatment, RW Fit Method:**

Using 800 fully simulated Monte Carlo subsamples with input values of  $(M_W, \Gamma_W) = (80.33 \text{ GeV}, 2.085 \text{ GeV})$ , each corresponding to the same integrated luminosity as the data sample, it was verified that both the one-parameter and the two-parameter fits have no observed bias at the precision studied. In addition, 2000 Monte Carlo test samples, each corresponding to the same integrated luminosity as the data, were used to study the reliability of the fit errors, the validity of the contour levels, and correlations between the various fitted parameters and their associated errors. Test samples were constructed by randomly sampling a parametrisation of the reconstructed mass spectrum (including detector simulation) in each channel.

The possibility of residual bias is further investigated as follows:

- To check for any biases in the reweighting procedure that could depend on the input mass or width, fits are performed on PYTHIA Monte Carlo samples with input  $W$  masses between 78.33 GeV and 82.33 GeV. Only the PYTHIA samples are used in the reweighting procedure, excluding the sample being fitted. An equivalent test is done with the different width samples. No significant shifts between the fitted and input values are found in the  $W^+W^- \rightarrow q\bar{q}\ell\bar{\nu}_\ell$  channels and the statistical precision of this test is taken as a systematic error. In the  $W^+W^- \rightarrow q\bar{q}q\bar{q}$  channel there is an indication of a small systematic effect which is believed to be an artifact of finite Monte Carlo statistics of the samples employed in the reweighting procedure. For values of  $M_W$  in the range of interest,  $80.33 \pm 0.50$  GeV, this bias is  $\pm 20$  MeV, which is taken as the systematic error.
- The effect of the finite Monte Carlo statistics in the background samples is estimated by comparing the results of repeated fits to a Monte Carlo sample using only fractions of the background sample.
- Variations in the normalisation of the predicted backgrounds, based upon uncertainties in the background cross-sections and efficiencies discussed in Section 3, were studied. The combined background is varied by 20% in the  $W^+W^- \rightarrow q\bar{q}q\bar{q}$  channel, and 40% in the  $W^+W^- \rightarrow q\bar{q}\ell\bar{\nu}_\ell$  channels. The observed shifts in the fit results are taken as systematic uncertainties.
- The procedure to correct for the difference between the actual beam energy and the beam energy with which the Monte Carlo samples are generated was checked by fitting the value for  $M_W$  in a PYTHIA sample generated with  $\sqrt{s} = 172$  GeV using only the PYTHIA samples generated with  $\sqrt{s} = 171$  GeV for the reweighting and background estimation. No significant bias is observed. The statistical accuracy of this test is taken as a systematic error.

The errors from all of these checks are added in quadrature to give the total systematic error due to uncertainties associated with the fitting procedure and background treatment.

### Fitting Procedure and Background Treatment, BW Fit Method:

The effects of using different analytic functions to describe the signal and background shapes, of fixing various fitted parameters, and of varying the fit range are investigated. In each case, the shift in the fit mass observed in the data is compared with the expected shift estimated using 400 Monte Carlo subsamples, each corresponding to the same integrated luminosity as the data. The following variations are considered:

- A simple non-relativistic Breit-Wigner is used for the signal.
- The relativistic Breit-Wigner is multiplied by a factor  $p^\alpha$ , where  $\alpha$  is a free parameter, and  $p$  is the centre-of-mass momentum of a pair of particles of mass  $m_{\text{rec}}$ .<sup>9</sup> In this case, the data are fitted up to the kinematic limit in  $m_{\text{rec}}$  with  $\alpha$  fixed to the value determined from Monte Carlo.
- The width parameter,  $\Gamma$ , is left as a free parameter in the fit.
- The background is represented by a quadratic in  $m_{\text{rec}}$ , with parameters determined in the fit to the data.
- The background normalisation is fixed to that expected from Monte Carlo.
- The relative normalisation of the combinatorial and  $Z^0/\gamma \rightarrow q\bar{q}$  backgrounds is varied by  $\pm 50\%$ .
- The masses of the combinatorial and  $Z^0/\gamma \rightarrow q\bar{q}$  backgrounds are displaced by 1 GeV.

---

<sup>9</sup>The mass distribution would be expected to be modified by a phase-space factor  $\propto p$ . However, this fails to describe the reconstructed Monte Carlo distribution, while a factor  $p^\alpha$  gives a reasonable fit up to the kinematic limit.

In each case, the shift in fitted mass observed in the data is consistent with that estimated from the Monte Carlo. The r.m.s. deviation of the differences of the observed shift between the data and Monte Carlo is taken as a systematic error.

**Colour Reconnection Effects and Bose-Einstein Correlations:** As discussed in [4] and references therein, a significant bias to the apparent  $W$  mass measured in the  $W^+W^- \rightarrow q\bar{q}q\bar{q}$  channel could arise from the effects of colour reconnection and Bose-Einstein correlations between the decay products of the  $W^+$  and  $W^-$ . Neither of these effects are included in the various hadronisation models used. There is no consensus as to the magnitude of such effects, though in some models they produce a shift in the measured  $M_W$  by as much as +100 MeV [4]. In some models, colour reconnection also affects other properties of  $W^+W^- \rightarrow q\bar{q}q\bar{q}$  events, for example, the charged particle multiplicity. As will be discussed in Section 6, with the sensitivity afforded by the present statistics, no indication of such reconnection effects is observed. In the absence of an experimental limit to the biases associated with these phenomena, a systematic uncertainty of  $\pm 100$  MeV is assigned to the  $W^+W^- \rightarrow q\bar{q}q\bar{q}$  channel due to these effects. As the  $W^+W^- \rightarrow q\bar{q}q\bar{q}$  channel comprises approximately half the total signal sample an uncertainty of  $\pm 50$  MeV is assigned in the combined analysis. One possible test of such effects is to compare  $M_W$  measured in the  $W^+W^- \rightarrow q\bar{q}q\bar{q}$  channel with that determined from  $W^+W^- \rightarrow q\bar{q}\ell\bar{\nu}_\ell$ . Within the present experimental errors the results are compatible. Monte Carlo studies on colour reconnection effects indicate that possible effects on the width are typically of the same size as on the mass. Thus, a corresponding error of  $\pm 50$  MeV is assigned to the width as determined from a combined fit to all channels.

## 5.5 Combination with Cross-section Measurements

The measurements of  $M_W$  from direct reconstruction and from the measurement of the  $W^+W^-$  production cross-section at  $\sqrt{s}=172.12$  GeV, as presented in this paper, may be combined with the value obtained from the  $W^+W^-$  production cross-section at  $\sqrt{s}=161.3$  GeV [5],

$$M_W = 80.40_{-0.41}^{+0.44} {}_{-0.10}^{+0.09} \pm 0.03 \text{ GeV},$$

where the errors are the statistical, systematic and beam energy uncertainties, respectively. The uncertainty of the LEP beam energy has been updated since Reference [5] as described in Reference [13]. The systematic effects of the three measurements are quite different, and therefore they are combined assuming that they are uncorrelated, apart from the uncertainty associated with the LEP beam energy, which is taken to be fully correlated. The result obtained is:

$$M_W = 80.35 \pm 0.24 \pm 0.06 \pm 0.03 \pm 0.03 \text{ GeV},$$

where the errors are the statistical, systematic, reconnection effects and beam energy uncertainties, respectively.

## 6 Properties of $W$ Pair Events

Hadronic data in  $e^+e^-$  collisions can be characterised by event shape distributions and inclusive observables such as charged particle multiplicities and momentum spectra. In  $e^+e^- \rightarrow W^+W^-$  events, although relatively little data have been collected, it is useful to study such characteristics. In addition to tests of Monte Carlo models, measurement of the properties of the hadronic sector of  $W^+W^-$  decays

allows the question of colour reconnection to be addressed experimentally. At present there is general consensus that observable effects of interactions between the colour singlets during the perturbative phase are expected to be small. In contrast, significant interference in the hadronisation process is considered to be a real possibility. With the current knowledge of non-perturbative QCD, such interference can be estimated only in the context of specific models [19, 20, 33–37].

It has been suggested [34, 35] that simple observable quantities, such as the charged multiplicity in restricted rapidity intervals, may be sensitive to the effects of colour reconnection. Such effects were predicted to be undetectable with data samples corresponding to  $10 \text{ pb}^{-1}$ . More recently [38] it was suggested that the effect on the inclusive charged multiplicity itself may be larger than previously considered and that the mean hadronic multiplicity in  $W^+W^- \rightarrow q\bar{q}q\bar{q}$  events,  $\langle n_{\text{ch}}^{4q} \rangle$ , may be as much as 10% smaller than twice the hadronic multiplicity in  $W^+W^- \rightarrow q\bar{q}\ell\bar{\nu}_\ell$  events,  $\langle n_{\text{ch}}^{\text{qq}\ell\nu} \rangle$ . The visible effects of such phenomena are expected to manifest themselves most clearly in low momentum regions. Therefore studies of the fragmentation function, i.e. the distribution of the scaled momentum,  $x_p = p/E_{\text{beam}}$ , are also relevant.

Most studies of sensitivity to colour reconnection have been estimated within the context of a given model, comparing “reconnection” to “no reconnection” scenarios; in general, both the size and sign of any changes are strongly dependent upon the model considered. At the expense of a reduction in statistical sensitivity, such model dependence can be avoided by comparing directly the properties of the hadronic part of  $W^+W^- \rightarrow q\bar{q}\ell\bar{\nu}_\ell$  events with  $W^+W^- \rightarrow q\bar{q}q\bar{q}$  events. In the current study, the inclusive charged multiplicity and the fragmentation function are measured and compared for  $W^+W^- \rightarrow q\bar{q}q\bar{q}$  and  $W^+W^- \rightarrow q\bar{q}\ell\bar{\nu}_\ell$  events. The quantities  $\Delta\langle n_{\text{ch}} \rangle = \langle n_{\text{ch}}^{4q} \rangle - 2\langle n_{\text{ch}}^{\text{qq}\ell\nu} \rangle$  and  $\Delta\langle x_p \rangle = \langle x_p^{4q} \rangle - \langle x_p^{\text{qq}\ell\nu} \rangle$  are also examined. By way of characterising the global properties of  $W^+W^- \rightarrow q\bar{q}q\bar{q}$  events themselves, mean values of the thrust distribution,  $\langle (1 - T)^{4q} \rangle$ , and the rapidity distribution relative to the thrust axis,  $\langle |y^{4q}| \rangle$ , are also measured in this channel. Mean values are used for these comparisons due to the relatively small size of the current data sample.

The models of colour reconnection implemented<sup>10</sup> in the event generators PYTHIA, HERWIG and ARIADNE [36] were used to assess the sensitivities of the quantities above to such effects. Observables such as  $\langle (1 - T)^{4q} \rangle$  and  $\langle |y^{4q}| \rangle$ , considered in earlier studies of colour reconnection, had a predicted sensitivity that was sufficiently small as to be unobservable at present. The models ARIADNE and a ‘colour octet’ variant<sup>11</sup> of HERWIG [39] predict shifts in  $\langle n_{\text{ch}}^{4q} \rangle$  and  $\langle x_p^{4q} \rangle$  similar in size to the statistical uncertainty observed on these quantities in the current data.

## 6.1 Correction Procedure

The distributions of  $n_{\text{ch}}$ ,  $x_p$ ,  $1 - T$  and  $y$  are corrected for background contamination using a bin-by-bin subtraction of the expected background, based on Monte Carlo estimates. Corrections are then applied for finite acceptance and the effects of detector resolution, after which mean values of the distributions are calculated. Each observable is evaluated using two samples of Monte Carlo events. The first includes full simulation of the OPAL detector and contains only those events which pass the cuts applied to the data (detector level). The second does not include initial state radiation or detector effects and allows all particles with lifetimes shorter than  $3 \times 10^{-10} \text{ s}$  to decay (hadron level). Both samples are generated at the same  $\sqrt{s}$ . Distributions normalised to the number of events at the detector and the hadron level are compared to derive bin-by-bin correction factors which are used to

<sup>10</sup>No retuning of any model was performed in generating events in the various reconnection scenarios.

<sup>11</sup>Merging of partons to form clusters was performed on a nearest neighbour basis, as a partial emulation of the model of Reference [37].



correct the observed distributions of  $x_p$ ,  $1 - T$  and  $y$ .

This correction method is not appropriate for the multiplicity distribution, since resolution and acceptance effects cause significant migration of charged tracks between bins. Instead, a matrix correction is used to correct for detector resolution effects, followed by a bin-by-bin correction which accounts for the effects due to acceptance cuts and residual initial state radiation, as in previous OPAL multiplicity studies [40].

The uncorrected multiplicity and thrust distributions for the  $W^+W^-$  candidate events before background subtraction are illustrated in Figures 10 and 11, together with the predictions of Monte Carlo events including detector simulation. The background prediction is the sum of all Standard Model processes, as described by the models used in Section 3. Good agreement is seen between the data and predictions from the models. The simulated  $W^+W^-$  events do not include colour reconnection effects.

## 6.2 Systematic Uncertainties

A number of systematic uncertainties have been considered in the analysis, as summarised in Table 15. Each systematic uncertainty is taken as a symmetric error and the total uncertainty is defined by adding the individual contributions in quadrature. The dependence of the correction procedure on the Monte Carlo model is evaluated by comparing results obtained using PYTHIA, KORALW or HERWIG as the  $W^+W^-$  signal samples. In each case, the same model is used for the subtraction of the small  $W^+W^-$  background contamination in each channel:  $W^+W^- \rightarrow q\bar{q}q\bar{q}$  or  $W^+W^- \rightarrow \ell^+\nu_\ell\ell'^-\bar{\nu}_{\ell'}$  events selected as  $W^+W^- \rightarrow q\bar{q}\ell\bar{\nu}_\ell$ , for example. Uncertainties arising from the selection of charged tracks are estimated by varying the track selection cuts and repeating the analysis. The maximum allowed values of the distances of closest approach to the interaction region in  $r$ - $\phi$  and  $z$  are varied from 2 cm to 5 cm and from 25 cm to 50 cm, respectively, and the minimum number of hits on tracks is varied from 20 to 40. The dependence on charged track quality cuts is the sum in quadrature of these three effects.

To test the dependence of the results on the event selection, alternative selections were considered. The  $W^+W^- \rightarrow q\bar{q}\ell\bar{\nu}_\ell$  selection was replaced by a cut-based selection similar to that used in [5], which has a lower efficiency but comparable purity to the likelihood selection. For the  $W^+W^- \rightarrow q\bar{q}q\bar{q}$  case, the standard likelihood selection is modified by adding a cut on the jet resolution parameter  $y_{34}$  such that 10% of the selected signal Monte Carlo events are removed from the sample. The entire analysis was repeated with the alternative selections.

The background estimates presented in Section 3 have overall uncertainties of order 25% for the  $q\bar{q}q\bar{q}$  and  $q\bar{q}\ell\bar{\nu}_\ell$  channels. These were taken into account by scaling the background by  $\pm 25\%$  before subtraction from the data. An additional uncertainty was included to allow for the fact that bin contents could become negative after background subtraction due to low statistics in the data.

An uncertainty was evaluated for the Monte Carlo tuning or model dependence of the  $Z^0/\gamma$  background by shifting the multiplicity distribution by  $\pm 1$  unit or comparing PYTHIA with HERWIG. These gave similar shifts in  $\langle n_{\text{ch}} \rangle$ . Other background contributions were also varied by considering alternative two-photon Monte Carlo samples from PYTHIA, HERWIG or TWOGEN, by comparing the corrected values when treating grc4f  $W^+W^-$  or four-fermion events as data, or by neglecting the  $Z^0/\gamma \rightarrow \tau^+\tau^-$  background. The corresponding systematic uncertainty was taken to be the sum in quadrature of the uncertainties from; the four-fermion study, the effect of neglecting the  $Z^0/\gamma \rightarrow \tau^+\tau^-$  background and the largest shift from the use of any two-photon sample.

Since most of the Monte Carlo samples used in the study were generated at  $\sqrt{s} = 171$  GeV, the analysis was repeated with  $W^+W^-$  and  $Z^0/\gamma$  samples generated at 172 GeV. The effect of varying the signal and background cross-sections over the range expected at these centre-of-mass energies was found to be negligible.

As a further systematic check, the mean values  $\langle n_{\text{ch}}^{4\text{q}} \rangle$ ,  $\langle n_{\text{ch}}^{\text{qq}\ell\nu} \rangle$ ,  $\langle x_p^{\text{qq}\ell\nu} \rangle$ ,  $\langle x_p^{4\text{q}} \rangle$ ,  $\langle (1-T)^{4\text{q}} \rangle$  and  $\langle |y^{4\text{q}}| \rangle$  were evaluated by applying a correction factor to each of the uncorrected values. This correction is the ratio between the PYTHIA prediction without detector simulation or initial state radiation, to the corresponding prediction for the same observable when these two effects are included. The change in the corrected value is included as an estimate of the systematic error due to the unfolding process. For  $\langle (1-T)^{4\text{q}} \rangle$ , this is the largest single contribution to the systematic uncertainty, as the event selection in the  $W^+W^- \rightarrow \text{q}\bar{\text{q}}\text{q}\bar{\text{q}}$  channel rejects events having two-jet like characteristics which are similar to the dominant  $Z^0/\gamma \rightarrow \text{q}\bar{\text{q}}$  background. Hence, part of the thrust distribution is unmeasured in data.

### 6.3 Results

The mean values of the event properties are as follows, where in each case the first uncertainty is statistical and the second systematic.

$$\begin{aligned}
\langle n_{\text{ch}}^{4\text{q}} \rangle &= 38.3 \pm 1.1 \pm 0.6 \\
\langle n_{\text{ch}}^{\text{qq}\ell\nu} \rangle &= 18.4 \pm 0.9 \pm 0.4 \\
\Delta\langle n_{\text{ch}} \rangle &= +1.5 \pm 2.2 \pm 0.8 \\
\langle x_p^{4\text{q}} \rangle &= (3.22 \pm 0.13 \pm 0.08) \times 10^{-2} \\
\langle x_p^{\text{qq}\ell\nu} \rangle &= (3.60 \pm 0.20 \pm 0.11) \times 10^{-2} \\
\Delta\langle x_p \rangle &= (-0.38 \pm 0.23 \pm 0.10) \times 10^{-2} \\
\langle (1-T)^{4\text{q}} \rangle &= 0.227 \pm 0.036 \pm 0.021 \\
\langle |y^{4\text{q}}| \rangle &= 1.033 \pm 0.042 \pm 0.025
\end{aligned}$$

The values of  $\langle (1-T)^{4\text{q}} \rangle$  and  $\langle |y^{4\text{q}}| \rangle$  agree well with the predictions of models, which are 0.219 and 1.031 for PYTHIA, and 0.216 and 1.032 for HERWIG, respectively. It is interesting to compare the mean charged particle multiplicity in  $W^+W^-$  events with that in  $Z^0/\gamma \rightarrow \text{q}\bar{\text{q}}$  events at  $\sqrt{s} = 172$  GeV, which has a value of approximately 26 [41].

The difference in mean charged multiplicities in hadronic W decays in  $\text{q}\bar{\text{q}}\text{q}\bar{\text{q}}$  and  $\text{q}\bar{\text{q}}\ell\bar{\nu}_\ell$  events,  $\Delta\langle n_{\text{ch}} \rangle$ , is found to be consistent with zero at the current level of statistical precision. Similarly, the measurements of the mean scaled charged particle momenta are consistent in the two channels. Figures 12(a) and (b) show the corrected fragmentation functions for the  $W^+W^- \rightarrow \text{q}\bar{\text{q}}\text{q}\bar{\text{q}}$  and  $W^+W^- \rightarrow \text{q}\bar{\text{q}}\ell\bar{\nu}_\ell$  channels, together with predictions from the PYTHIA and HERWIG models. The models are in good agreement within statistical uncertainties in both cases. An alternative measurement of the mean charged multiplicity may be obtained from the integral of the fragmentation function. The values determined in this way are  $\langle n_{\text{ch}}^{4\text{q}} \rangle = 38.2$  and  $\langle n_{\text{ch}}^{\text{qq}\ell\nu} \rangle = 18.2$ . Figure 12(c) shows the ratio of the  $x_p^{4\text{q}}$  distribution to twice the  $x_p^{\text{qq}\ell\nu}$  distribution for low particle momenta,  $x_p < 0.2$ . The ratio is slightly greater than unity in the high statistics region, in agreement with the positive value of  $\Delta\langle n_{\text{ch}} \rangle$  measured above.

In summary, the  $W^+W^-$  event properties presented here are in good agreement with expectations of standard QCD models. From studies of reconnection phenomena implemented with the HERWIG, ARIADNE and PYTHIA models, changes up to approximately one statistical standard deviation in

the current data may be expected in  $\langle n_{\text{ch}}^{4\text{q}} \rangle$  and  $\langle x_p^{4\text{q}} \rangle$ . Shifts several times larger have also been predicted for  $\langle n_{\text{ch}}^{4\text{q}} \rangle$  [38]. Defining  $\Delta\langle n_{\text{ch}} \rangle$  and  $\Delta\langle x_p \rangle$  using data alone provides a model independent test of possible reconnection effects. The maximum shifts in these variables predicted by the models considered are at the level 0.5–1.5 standard deviations for the current data set. There is no indication of the effects of colour reconnection on these observables at the current level of statistical precision.

## 7 Summary

W pair events produced in  $e^+e^-$  collisions at 172.12 GeV were analysed. A Monte Carlo based reweighting method was used to fit the reconstructed mass spectra of the selected hadronic and semi-leptonic W pair events to obtain the following values for the mass and decay width of the W boson:

$$\begin{aligned} M_W &= 80.30 \pm 0.27 \pm 0.09 \text{ GeV}, \\ \Gamma_W &= 1.30_{-0.55}^{+0.62} \pm 0.18 \text{ GeV}, \end{aligned}$$

where the first uncertainty is statistical and the second is systematic. The fitted width is approximately one standard deviation below the Standard Model prediction for this value of  $M_W$ . Constraining  $\Gamma_W$  to its Standard Model relation gives a measurement of the mass of

$$M_W = 80.32 \pm 0.30 \pm 0.09 \text{ GeV}.$$

These results are consistent with a recent result [42]. A Breit-Wigner fit to the reconstructed mass spectra was used to check the reweighting method for the extraction of  $M_W$ , and found to give a consistent result. Combining the above value for  $M_W$  with the OPAL threshold measurement [5] of the W boson mass and that derived from the measurement of  $\sigma_{\text{WW}}(172 \text{ GeV})$ , gives

$$M_W = 80.35 \pm 0.24 \pm 0.06 \pm 0.03 \pm 0.03 \text{ GeV},$$

where the uncertainties are statistical, systematic, colour reconnection and Bose-Einstein, and beam energy, respectively.

The production cross-section for  $W^+W^-$  events at this energy was found to be

$$\sigma_{\text{WW}}(172 \text{ GeV}) = 12.3 \pm 1.3 \pm 0.3 \text{ pb}.$$

The decay branching fractions of the W boson were measured assuming only Standard Model W decay modes. When combined with the previous OPAL results at  $\sqrt{s}=161.3 \text{ GeV}$  the following leptonic branching fractions for the W boson are obtained:

$$\begin{aligned} \text{Br}(W \rightarrow e\bar{\nu}_e) &= 0.098_{-0.020}^{+0.022} \pm 0.003, \\ \text{Br}(W \rightarrow \mu\bar{\nu}_\mu) &= 0.073_{-0.017}^{+0.019} \pm 0.002, \\ \text{Br}(W \rightarrow \tau\bar{\nu}_\tau) &= 0.140_{-0.028}^{+0.030} \pm 0.005. \end{aligned}$$

If charged current lepton universality is assumed then the leptonic and hadronic branching fractions are determined to be

$$\begin{aligned} \text{Br}(W \rightarrow \ell\bar{\nu}_\ell) &= 0.101_{-0.010}^{+0.011} \pm 0.002, \\ \text{Br}(W \rightarrow \text{q}\bar{\text{q}}) &= 0.698_{-0.032}^{+0.030} \pm 0.007, \end{aligned}$$

where the errors are 100% anti-correlated. The hadronic branching fraction result gives a direct measurement of the sum of squares of kinematically accessible elements of the CKM matrix,

$$\sum_{i=u,c;j=d,s,b} |V_{ij}|^2 = 2.22_{-0.34}^{+0.32} \pm 0.07.$$

This can in turn be interpreted as a measurement of the element  $|V_{cs}|$ ,

$$|V_{cs}| = 1.08_{-0.16}^{+0.15} \pm 0.03,$$

by using measured values of the other  $|V_{ij}|^2$  parameters. The measurement of  $|V_{cs}|$  is consistent in value with and has a comparable uncertainty to other determinations which do not invoke unitarity [1]. The above cross section and branching fraction measurements are consistent with the Standard Model expectations and with recent results [30].

The predicted effects of colour reconnection and Bose-Einstein phenomena in the fully hadronic channel, and also their influence on  $M_W$ , are model dependent. A first investigation of these effects was performed in data alone by comparing the distribution of the fragmentation function,  $x_p$ , and mean values of the charged particle multiplicity and  $x_p$  for  $W^+W^- \rightarrow q\bar{q}q\bar{q}$  and the non-leptonic component of  $W^+W^- \rightarrow q\bar{q}\ell\bar{\nu}_\ell$  events. The mean values obtained in the two channels are found to be consistent, with differences:

$$\begin{aligned} \Delta\langle n_{\text{ch}} \rangle &= \langle n_{\text{ch}}^{4q} \rangle - 2\langle n_{\text{ch}}^{qq\ell\nu} \rangle = +1.5 \pm 2.2 \pm 0.8 \\ \Delta\langle x_p \rangle &= \langle x_p^{4q} \rangle - \langle x_p^{qq\ell\nu} \rangle = (-0.38 \pm 0.23 \pm 0.10) \times 10^{-2}. \end{aligned}$$

In addition, mean values of rapidity and thrust are determined for  $W^+W^- \rightarrow q\bar{q}q\bar{q}$  events. All measurements are in agreement with predictions of standard QCD models. At the current level of statistical precision no evidence for colour reconnection effects was found in the observables studied.

## 8 Acknowledgements

We particularly wish to thank the SL Division for the efficient operation of the LEP accelerator at all energies and for their continuing close cooperation with our experimental group. We thank our colleagues from CEA, DAPNIA/SPP, CE-Saclay for their efforts over the years on the time-of-flight and trigger systems which we continue to use. In addition to the support staff at our own institutions we are pleased to acknowledge the

Department of Energy, USA,

National Science Foundation, USA,

Particle Physics and Astronomy Research Council, UK,

Natural Sciences and Engineering Research Council, Canada,

Israel Science Foundation, administered by the Israel Academy of Science and Humanities,

Minerva Gesellschaft,

Benoziyo Center for High Energy Physics,

Japanese Ministry of Education, Science and Culture (the Monbusho) and a grant under the Monbusho International Science Research Program,

German Israeli Bi-national Science Foundation (GIF),

Bundesministerium für Bildung, Wissenschaft, Forschung und Technologie, Germany,

National Research Council of Canada,

Hungarian Foundation for Scientific Research, OTKA T-016660, T023793 and OTKA F-023259.

## Appendices

### A $W^+W^- \rightarrow q\bar{q}\ell\bar{\nu}_\ell$ Event Selection

The selection of each flavour of  $W^+W^- \rightarrow q\bar{q}\ell\bar{\nu}_\ell$  events is divided into four distinct stages as discussed in Section 3.3, namely identification of a charged lepton candidate, preselection, relative likelihood selection to separate signal from the remaining background, and event categorisation. Details of each of these stages are given below. Only events which fail the  $W^+W^- \rightarrow \ell^+\nu_\ell\ell'^-\bar{\nu}_{\ell'}$  selection are considered as possible  $W^+W^- \rightarrow q\bar{q}\ell\bar{\nu}_\ell$  candidates.

#### A.1 Identification of the Candidate Electron and Muon

In order to maximise efficiency no explicit lepton identification is required. Instead, the track in the event which is most consistent with being an electron (muon) from the decay  $W \rightarrow e\bar{\nu}_e$  ( $W \rightarrow \mu\bar{\nu}_\mu$ ) is taken to be the candidate lepton. This track is identified using two types of variables: a) lepton identification variables, for example, number of hits in the hadron calorimeter or specific energy loss in the central tracking chamber; and b) variables representing the probability that the lepton arose from a  $W$  decay, for example, energy and isolation. These variables are used to calculate, for each track, the probability that the track arose from a  $W \rightarrow e\bar{\nu}_e$  decay,  $P(e)$ , or from a  $W \rightarrow \mu\bar{\nu}_\mu$  decay,  $P(\mu)$ . These probabilities are the products of probabilities from the individual variables, which are determined using probability density functions obtained from  $W^+W^-$  Monte Carlo. The track with the highest value of  $P(e)$  is taken to be the candidate electron in the  $W^+W^- \rightarrow q\bar{q}e\bar{\nu}_e$  selection and the track with the highest value of  $P(\mu)$  is taken to be the candidate muon in the  $W^+W^- \rightarrow q\bar{q}\mu\bar{\nu}_\mu$  selection. Each event will yield one candidate electron track and one candidate muon track.

#### A.2 Definition of Variables

Having selected the most likely electron and muon candidates, variables are constructed which are used in the preselection and, subsequently, in the likelihood selection. The following variables are used:

- $E_{\text{lept}}$ , the energy of the candidate lepton. For electrons this is calculated using the electromagnetic calorimeter energy; for muons the track momentum is used,
- $\cos\theta_{\text{lpmis}}$ , the cosine of the angle between the lepton track and the missing momentum vector,
- $|\cos\theta_{\text{mis}}|$ , the cosine of the angle the missing momentum vector makes with the beam axis,
- $E_{200}$ , the energy in a cone of 200 mrad around the candidate lepton evaluated using tracks and ECAL clusters,
- $P(e)$  or  $P(\mu)$ , the electron or muon identification probability for the candidate lepton track,
- $R_{\text{vis}}$ , the visible energy of the event scaled by  $\sqrt{s}$ ,
- $y_{23}$ , where  $y_{ij}$  is the value of the jet resolution parameter (Durham scheme [31]) at which an event is reclassified from  $i$  jets to  $j$  jets,

- $\sum p_T$ , the transverse momentum of the event relative to the beam axis, calculated using tracks, ECAL clusters and HCAL clusters,
- $P(s')$ , the probability from a kinematic fit which estimates the invariant mass of the event,  $\sqrt{s'}$ ,
- $\theta_{\text{jet}}$ , the angle between the lepton candidate and the jet axis of the nearest hadronic jet.

### A.3 Preselection

Preselection cuts are applied to remove events which are clearly inconsistent with  $W^+W^- \rightarrow q\bar{q}\ell\bar{\nu}_\ell$  decays. In particular, the preselections are designed to remove most two-photon events and a significant fraction of the  $Z^0/\gamma \rightarrow q\bar{q}$  background. Slightly different preselection cuts are applied in the  $W^+W^- \rightarrow q\bar{q}e\bar{\nu}_e$  and  $W^+W^- \rightarrow q\bar{q}\mu\bar{\nu}_\mu$  selections. Firstly, events are required to have more than five charged tracks and more than seven electromagnetic calorimeter clusters. In addition, the main preselection cuts are:  $E_{\text{lept}} > 10.0$  GeV,  $0.30 < R_{\text{vis}} < 1.05$ , the total energy in the forward luminosity monitors  $< 40$  GeV,  $\cos\theta_{\text{lpmis}} < 0.0$  and the energy of the highest energy isolated photon in the event  $< (E_{\text{ISR}} - 10)$  GeV, where  $E_{\text{ISR}}$  is the expected energy of an initial state photon for radiative events with  $\sqrt{s'} \sim M_{Z^0}$ . An isolated photon is defined as an ECAL cluster which is not associated to a track and which satisfies the isolation requirement of less than 2.5 GeV of energy in a 200 mrad cone around the cluster. Finally, loose cuts are made on the lepton identification probabilities and, in the case of the  $W^+W^- \rightarrow q\bar{q}e\bar{\nu}_e$  selection, several cuts are made to reduce the background from converting photons. The preselection is approximately 92% efficient for  $W^+W^- \rightarrow q\bar{q}e\bar{\nu}_e$  and  $W^+W^- \rightarrow q\bar{q}\mu\bar{\nu}_\mu$  events, where about half the loss in efficiency arises from cases where the lepton is outside the experimental acceptance for well reconstructed charged tracks. The preselection cuts remove approximately 90% of the  $Z^0/\gamma \rightarrow q\bar{q}$  background.

### A.4 Relative Likelihood Selection

For events passing the electron preselection, a relative likelihood method is used to distinguish  $W^+W^- \rightarrow q\bar{q}e\bar{\nu}_e$  events from the background of  $Z^0/\gamma \rightarrow q\bar{q}$  events. After the preselection cuts there is still a signal to background ratio of less than 0.1. The likelihoods are based on a set of variables,  $x_i$ , where the observed values are compared to the expected distributions (obtained from Monte Carlo) for  $W^+W^- \rightarrow q\bar{q}e\bar{\nu}_e$  events from which the probabilities,  $P_i(x_i)$ , are obtained. The likelihood,  $L^{\text{q}\bar{q}e\bar{\nu}_e}$ , is calculated as the product of these probabilities for the individual variables used in the analysis. The background likelihood,  $L^{\text{q}\bar{q}}$ , is obtained in the same manner using Monte Carlo distributions for  $Z^0/\gamma \rightarrow q\bar{q}$  events. The relative likelihood,  $\mathcal{L}^{\text{q}\bar{q}e\bar{\nu}_e}$ , is calculated as:

$$\mathcal{L}^{\text{q}\bar{q}e\bar{\nu}_e} = \frac{L^{\text{q}\bar{q}e\bar{\nu}_e}}{L^{\text{q}\bar{q}e\bar{\nu}_e} + f \times L^{\text{q}\bar{q}}},$$

where the normalisation factor,  $f$ , is the ratio of preselected background to signal cross-sections from Monte Carlo. The variables used in the  $W^+W^- \rightarrow q\bar{q}e\bar{\nu}_e$  likelihood are:  $E_{\text{lept}}$ ,  $E_{200}$ ,  $P(e)$ ,  $y_{23}$ ,  $R_{\text{vis}}$ ,  $|\cos\theta_{\text{mis}}|$ ,  $\sum p_T$ ,  $\cos\theta_{\text{lpmis}}$ ,  $P(s')$  and  $\theta_{\text{jet}}$ . The  $q\bar{q}\mu\bar{\nu}_\mu$  relative likelihood,  $\mathcal{L}^{\text{q}\bar{q}\mu\bar{\nu}_\mu}$ , is obtained in the same manner with a slightly modified set of variables; with  $P(\mu)$  replacing  $P(e)$  and by not using  $\theta_{\text{jet}}$ . The inclusion of  $\theta_{\text{jet}}$  in the  $q\bar{q}e\bar{\nu}_e$  likelihood was observed to improve the signal and background separation whereas in the  $q\bar{q}\mu\bar{\nu}_\mu$  selection this was not the case. Figure 13 shows the distributions of a number of these variables where each plot shows the combination of the distributions for events passing the  $W^+W^- \rightarrow q\bar{q}e\bar{\nu}_e$  and  $W^+W^- \rightarrow q\bar{q}\mu\bar{\nu}_\mu$  preselections.

Figure 14(a) shows the distribution of  $\mathcal{L}^{q\bar{q}e\bar{\nu}_e}$  for events passing the  $W^+W^- \rightarrow q\bar{q}e\bar{\nu}_e$  preselection. The value of the relative likelihood peaks at around one for  $W^+W^- \rightarrow q\bar{q}e\bar{\nu}_e$  events and zero for  $Z^0/\gamma \rightarrow q\bar{q}$  events. Figure 14(b) shows the equivalent distribution of  $\mathcal{L}^{q\bar{q}\mu\bar{\nu}_\mu}$  for events passing the  $W^+W^- \rightarrow q\bar{q}\mu\bar{\nu}_\mu$  preselection. Events with  $\mathcal{L}^{q\bar{q}e\bar{\nu}_e} > 0.5$  or  $\mathcal{L}^{q\bar{q}\mu\bar{\nu}_\mu} > 0.5$  are selected as  $W^+W^- \rightarrow q\bar{q}e\bar{\nu}_e$  or  $W^+W^- \rightarrow q\bar{q}\mu\bar{\nu}_\mu$  candidates, respectively. The combination of preselection and likelihood selection rejects about 99.95% of the  $Z^0/\gamma \rightarrow q\bar{q}$  background and is approximately 90% efficient for  $W^+W^- \rightarrow q\bar{q}e\bar{\nu}_e$  and  $W^+W^- \rightarrow q\bar{q}\mu\bar{\nu}_\mu$  events.

## A.5 Event Categorisation

Although the above likelihood selections were optimised to separate  $W^+W^- \rightarrow q\bar{q}e\bar{\nu}_e$  and  $W^+W^- \rightarrow q\bar{q}\mu\bar{\nu}_\mu$  events from the  $Z^0/\gamma \rightarrow q\bar{q}$  background, they also select approximately 25% of  $W^+W^- \rightarrow q\bar{q}\tau\bar{\nu}_\tau$  decays. For this reason events passing the  $q\bar{q}e\bar{\nu}_e$  selection are re-classified as either  $W^+W^- \rightarrow q\bar{q}e\bar{\nu}_e$  or  $W^+W^- \rightarrow q\bar{q}\tau\bar{\nu}_\tau$  and events passing the  $q\bar{q}\mu\bar{\nu}_\mu$  selection are re-classified as either  $q\bar{q}\mu\bar{\nu}_\mu$  or  $q\bar{q}\tau\bar{\nu}_\tau$ . This assignment enables separate cross-sections for the three  $W^+W^- \rightarrow q\bar{q}\ell\bar{\nu}_\ell$  channels to be evaluated cleanly. The predominant  $W^+W^- \rightarrow q\bar{q}\tau\bar{\nu}_\tau$  contamination in the  $q\bar{q}e\bar{\nu}_e$  selection arises from cases where the tau lepton decays to an electron or decays into a one prong hadronic final state. Therefore, for events identified as  $W^+W^- \rightarrow q\bar{q}e\bar{\nu}_e$ , two relative likelihoods, analogous to those described in Section A.4, are constructed using the same variables as were used in the  $W^+W^- \rightarrow q\bar{q}e\bar{\nu}_e$  likelihood selection. The first relative likelihood attempts to separate  $W^+W^- \rightarrow q\bar{q}\tau\bar{\nu}_\tau \rightarrow q\bar{q}(e\bar{\nu}_e\nu_\tau)\bar{\nu}_\tau$  decays from  $W^+W^- \rightarrow q\bar{q}e\bar{\nu}_e$  decays and the second attempts to separate  $W^+W^- \rightarrow q\bar{q}\tau\bar{\nu}_\tau \rightarrow q\bar{q}(\pi^\pm n\pi^0\nu_\tau)\bar{\nu}_\tau$  from  $W^+W^- \rightarrow q\bar{q}e\bar{\nu}_e$ . If either of these relative likelihoods is greater than 0.5 the event is re-categorised as  $W^+W^- \rightarrow q\bar{q}\tau\bar{\nu}_\tau$ . A similar procedure is applied to events passing the  $W^+W^- \rightarrow q\bar{q}\mu\bar{\nu}_\mu$  selection. The result of the event categorisation is that all events passing the  $q\bar{q}e\bar{\nu}_e$  and  $q\bar{q}\mu\bar{\nu}_\mu$  selections are categorised as either  $W^+W^- \rightarrow q\bar{q}e\bar{\nu}_e$ ,  $W^+W^- \rightarrow q\bar{q}\mu\bar{\nu}_\mu$  or  $W^+W^- \rightarrow q\bar{q}\tau\bar{\nu}_\tau$ .

## A.6 $W^+W^- \rightarrow q\bar{q}\tau\bar{\nu}_\tau$ Event Selection

A relative likelihood selection designed to separate  $W^+W^- \rightarrow q\bar{q}\tau\bar{\nu}_\tau$  from  $Z^0/\gamma \rightarrow q\bar{q}$  background is applied to events which fail the  $W^+W^- \rightarrow q\bar{q}e\bar{\nu}_e$  and  $W^+W^- \rightarrow q\bar{q}\mu\bar{\nu}_\mu$  selections described in Sections A.1–A.4. Approximately 25% of all events finally selected as  $W^+W^- \rightarrow q\bar{q}\tau\bar{\nu}_\tau$  are from the analysis given in Sections A.1–A.5, the remaining events being selected as summarised below. The  $W^+W^- \rightarrow q\bar{q}\tau\bar{\nu}_\tau$  event selection proceeds in a similar manner to the  $W^+W^- \rightarrow q\bar{q}e\bar{\nu}_e$  selection described above, *i.e.* ‘lepton’ identification, preselection and relative likelihood selection. In this case no additional event categorisation is performed. The selection has been designed to be sensitive to the four main tau decay classes: electron, muon, hadronic one prong and hadronic three prong. Consequently four separate selections are applied. The lepton identification of the  $W^+W^- \rightarrow q\bar{q}e\bar{\nu}_e$  selection is replaced by the identification of the track most consistent with being from  $W \rightarrow \tau\bar{\nu}_\tau \rightarrow (e\bar{\nu}_e\nu_\tau)\bar{\nu}_\tau$ ,  $W \rightarrow \tau\bar{\nu}_\tau \rightarrow (\mu\bar{\nu}_\mu\nu_\tau)\bar{\nu}_\tau$  and  $W \rightarrow \tau\bar{\nu}_\tau \rightarrow (\pi^\pm n\pi^0\nu_\tau)\bar{\nu}_\tau$  decays. To be sensitive to three prong tau decays, the combination of three tracks which is most consistent with a  $W \rightarrow \tau\bar{\nu}_\tau \rightarrow (2\pi^\pm\pi^\mp\nu_\tau)\bar{\nu}_\tau$  decay is also identified. The  $W^+W^- \rightarrow q\bar{q}\tau\bar{\nu}_\tau$  selection then proceeds as four preselections, one for each of the above cases, and four corresponding likelihood selections. The variables used in the likelihood are similar to those used above but include more information about the track (or tracks) identified as the tau decay *e.g.* the invariant mass of all tracks and clusters within a 200 mrad cone around the track. Figure 15 shows a sample of the variables used in the likelihood selections. An event with a relative likelihood greater than 0.75 for any one of the four tau likelihoods, is categorised as a  $W^+W^- \rightarrow q\bar{q}\tau\bar{\nu}_\tau$  event. Events passing more than one of the  $W^+W^- \rightarrow q\bar{q}\tau\bar{\nu}_\tau$  likelihood selections enter the final event sample only once.

## B $W^+W^- \rightarrow q\bar{q}q\bar{q}$ Selection

The selection of  $W^+W^- \rightarrow q\bar{q}q\bar{q}$  events described below is divided into two parts, namely a preselection and a likelihood based discriminant formed from the combination of seven observables. A modified version of this selection, which uses the same preselection and likelihood observables, is used to obtain a weight for each event to be a  $W^+W^- \rightarrow q\bar{q}q\bar{q}$  event. This variant, described in Section B.3, leads to a small reduction in the predicted uncertainty this channel contributes to the  $W^+W^-$  cross-section measurement and is therefore used in the analysis of cross-sections and branching fractions.

### B.1 Preselection

Candidate events are required to be classified as hadronic [43] and not be selected by either the  $W^+W^- \rightarrow \ell^+\nu_\ell\ell'^-\bar{\nu}_{\ell'}$  or  $W^+W^- \rightarrow q\bar{q}\ell\bar{\nu}_\ell$  selections. Tracks and calorimeter clusters are combined into four jets using the Durham [31] jet-finding algorithm, and the total momentum and energy of each of the jets are corrected for double-counting of energy [44]. To remove events which are clearly inconsistent with  $W^+W^- \rightarrow q\bar{q}q\bar{q}$  events, predominantly radiative  $Z^0/\gamma$  events, candidate events are required to satisfy the following preselection criteria:

- $\sqrt{s'}$ , the fitted invariant mass of the hadronic system, must be greater than 140 GeV.
- The energy of the most energetic isolated photon must be less than  $0.3\sqrt{s}$ .
- The visible energy of the event must be greater than  $0.70\sqrt{s}$ .
- $y_{34} > 0.003$ , where  $y_{ij}$  is the value of the jet resolution parameter at which an event is reclassified from  $i$  jets to  $j$  jets.
- Each jet is required to contain at least one charged track.
- A kinematic fit, which imposes energy and momentum conservation and equality of the W masses, is performed on all three possible assignments of jets to W candidates in the event. At least one of these combinations must result in a convergent fit.

The efficiency of these preselection requirements for  $W^+W^- \rightarrow q\bar{q}q\bar{q}$  events,  $\epsilon_{sig}^{pre}$ , is 90.3%, whilst rejecting 96.6% of the  $Z^0/\gamma \rightarrow q\bar{q}$  events. The total background cross-section after the preselection,  $\sigma_{bgd}^{pre}$ , is estimated to be 4.5 pb. The preselection accepts 99 events in data.

### B.2 Likelihood Variables

Events satisfying the preselection criteria are subjected to a likelihood selection, which discriminates between signal and the remaining four-jet-like QCD background. The likelihoods are based on a set of seven variables,  $y_i$ . Probability density distributions are determined for each  $y_i$ , using both simulated  $W^+W^- \rightarrow q\bar{q}q\bar{q}$  and  $Z^0/\gamma \rightarrow q\bar{q}$  events. Each of these  $y_i$  distributions are used to construct probabilities corresponding to the hypotheses that a given event in data is either  $W^+W^- \rightarrow q\bar{q}q\bar{q}$  or  $Z^0/\gamma \rightarrow q\bar{q}$ . The likelihoods,  $L^{q\bar{q}q\bar{q}}$  and  $L^{q\bar{q}}$ , are calculated as the product of these probabilities. The relative likelihood discriminant itself,  $\mathcal{L}^{q\bar{q}q\bar{q}}$ , is defined in terms of these two likelihoods as:

$$\mathcal{L}^{q\bar{q}q\bar{q}} = \frac{L^{q\bar{q}q\bar{q}}}{L^{q\bar{q}q\bar{q}} + L^{q\bar{q}}}.$$



The value of  $\mathcal{L}^{\text{q}\bar{\text{q}}\text{q}\bar{\text{q}}}$ , between zero and one, is used to discriminate between signal and background events.

The following seven variables, which use the characteristic four-jet-like nature, momentum balance and angular structure of  $W^+W^- \rightarrow \text{q}\bar{\text{q}}\text{q}\bar{\text{q}}$  to distinguish events from the remaining background, are used to construct the likelihoods:

- the logarithm of  $y_{34}$ ,
- the logarithm of  $y_{45}$ ,
- the sphericity of the event,
- the quantity  $J_{\text{mom}}$ , defined as

$$J_{\text{mom}} = \frac{(p_1 + p_2 - p_3 - p_4)}{\sqrt{s}},$$

where  $p_i$  are the jet momenta, and the jets are ordered by energy such that  $p_1$  is the momentum of the most energetic jet,

- the cosine of the modified Nachtmann-Reiter angle,  $\cos \theta_{N-R}$  (see [45]),
- the cosine of the angle between the two least energetic jets,  $\cos \theta_{34}$ ,
- the logarithm of the QCD event weight,  $qcd_{420}$  [46], which is calculated using the tree level matrix element for the processes  $e^+e^- \rightarrow \text{q}\bar{\text{q}}\text{q}\bar{\text{q}}, \text{q}\bar{\text{q}}gg$  [46]. This quantity should have large values for hadronic  $Z^0/\gamma$  decays and smaller values for  $W^+W^-$  events.

The distributions of data passing the preselection criteria for each of these quantities is shown in Figure 16, together with the predictions of the PYTHIA Monte Carlo for  $W^+W^- \rightarrow \text{q}\bar{\text{q}}\text{q}\bar{\text{q}}$  and hadronic  $Z^0/\gamma$  decays. Good agreement is seen. The resulting likelihood distribution is given in Figure 17(a). A cut value of  $> 0.2$  on the likelihood is used for the measurements of the mass and event properties.

### B.3 $W^+W^- \rightarrow \text{q}\bar{\text{q}}\text{q}\bar{\text{q}}$ Event Weights

For the  $W^+W^-$  cross-section and  $W$  branching fraction measurements the 99 events passing the  $W^+W^- \rightarrow \text{q}\bar{\text{q}}\text{q}\bar{\text{q}}$  preselection are assigned weights, between zero and one, reflecting the probability that the event is from  $W^+W^- \rightarrow \text{q}\bar{\text{q}}\text{q}\bar{\text{q}}$  rather than background. The use of event weights results in a 5% smaller statistical uncertainty on these measurements<sup>12</sup>. The weighting method of event classification is discussed in [47]. The optimal choice of event weight is the probability that the event arose from signal rather than background. In the absence of correlations between the likelihood variables, the relative likelihood gives the probability of an event being  $W^+W^- \rightarrow \text{q}\bar{\text{q}}\text{q}\bar{\text{q}}$ . The likelihood variables described in Section B.2 are not uncorrelated. For this reason a linear transformation is applied to the likelihood variables, in order to obtain a new set of variables where the off-diagonal elements of the covariance matrix are zero. These transformed variables are then used to construct the relative likelihood function which is used as an event weight. The transformation is performed using the orthogonal matrix which results in transformed variables with diagonal covariance matrices for both

<sup>12</sup> In the case of the  $W^+W^- \rightarrow \text{q}\bar{\text{q}}\ell\bar{\nu}_\ell$  selection the discrimination between signal and background is much greater and event weights give a negligible improvement in statistical uncertainty and are therefore not used.

the signal and background separately. The event weight,  $w_i$ , calculated using these transformed variables is defined:

$$w_i = \frac{N_{q\bar{q}q\bar{q}}L^{q\bar{q}q\bar{q}}}{N_{q\bar{q}q\bar{q}}L^{q\bar{q}q\bar{q}} + N_{q\bar{q}}L^{q\bar{q}}},$$

where  $N_{q\bar{q}q\bar{q}}$  and  $N_{q\bar{q}}$  are the expected numbers of preselected  $W^+W^- \rightarrow q\bar{q}q\bar{q}$  and background events respectively. The weights for the preselected events are compared to the Monte Carlo expectation in Figure 17(b). In calculating the event weights, the small background contributions from  $(Z^0/\gamma)(Z^0/\gamma) \rightarrow q\bar{q}q\bar{q}$  and  $W^+W^- \rightarrow q\bar{q}\ell\bar{\nu}_\ell$  are included with the dominant  $Z^0/\gamma \rightarrow q\bar{q}$  background in the background covariance matrix and the probability density distributions.

## References

- [1] The Particle Data Group, R.M. Barnett *et al.*, Phys. Rev. **D54** (1996) 1.
- [2] CDF Collaboration, F. Abe *et al.*, Phys. Rev. Lett. **75** (1995) 11, Phys. Rev. **D52** (1995) 4784; CDF Collaboration, F. Abe *et al.*, Phys. Rev. Lett. **65** (1990) 2243, Phys. Rev. **D43** (1991) 2070; UA2 Collaboration, J. Alitti *et al.*, Phys. Lett. **B276** (1992) 354; UA1 Collaboration, C. Albajar *et al.*, Z. Phys. **C44** (1989) 15.
- [3] D0 Collaboration, S. Abachi *et al.*, Phys. Rev. Lett. **77** (1996) 3309.
- [4] Proceedings of CERN LEP2 Workshop, CERN 96-01, Vols. 1 and 2, eds. G. Altarelli, T. Sjöstrand and F. Zwirner, February 1996.
- [5] OPAL Collaboration, K. Ackerstaff *et al.*, Phys. Lett. **B389** (1996) 416.
- [6] DELPHI Collaboration, P. Abreu *et al.*, Phys. Lett. **B397** (1997) 158.
- [7] L3 Collaboration, M. Acciarri *et al.*, Phys. Lett. **B398** (1997) 223.
- [8] ALEPH Collaboration, R. Barate *et al.*, Phys. Lett. **B401** (1997) 347.
- [9] OPAL Collaboration, K. Ahmet *et al.*, Nucl. Instr. Meth. **A305** (1991) 275; P.P. Allport *et al.*, Nucl. Instr. Meth. **A324** (1993) 34; P.P. Allport *et al.*, Nucl. Instr. Meth. **A346** (1994) 476.
- [10] M. Hauschild *et al.*, Nucl. Instr. Meth. **A314** (1992) 74; O. Biebel *et al.*, Nucl. Instr. Meth. **A323** (1992) 169.
- [11] B.E. Anderson *et al.*, IEEE Transactions on Nuclear Science, **41** (1994) 845.
- [12] OPAL Collaboration, K. Ackerstaff *et al.*, *Tests of the Standard Model and Constraints on New Physics from Measurements of Fermion-pair Production at 130–172 GeV at LEP*, CERN-PPE/97-101, Submitted to Z. Phys. C.
- [13] LEP Energy Working Group, *LEP Energy Calibration in 1996*, LEP Energy Group/97-01, 20th March 1997.
- [14] D. Bardin *et al.*, Nucl. Phys. B, Proc. Suppl. **37B** (1994) 148; D. Bardin *et al.*, *GENTLE/4fan v. 2.0: A Program for the Semi-Analytic Calculation of Predictions for the Process  $e^+e^- \rightarrow 4f$* , DESY 96-233, `\protect\vrule width0pt\protect\href{http://arxiv.org/abs/hep-ph/9612409}{hep-ph/9612409}`.
- [15] J. Allison *et al.*, Nucl. Instr. Meth. **A317** (1992) 47.
- [16] Program KORALW, M. Skrzypek *et al.*, Comput. Phys. Commun. **94** (1996) 216; M. Skrzypek *et al.*, Phys. Lett. **B372** (1996) 289.
- [17] Program EXCALIBUR, F.A. Berends, R. Pittau and R. Kleiss, Comput. Phys. Commun. **85** (1995) 437.
- [18] J. Fujimoto *et al.*, *GRC4F V1.1: A four fermion event generator for  $e^+e^-$  collisions*, Comput. Phys. Commun. **100** (1997) 128.
- [19] T. Sjöstrand, Comput. Phys. Commun. **82** (1994) 74.
- [20] Program HERWIG, G. Marchesini *et al.*, Comput. Phys. Commun. **67** (1992) 465.

- [21] S. Jadach *et al.*, Comput. Phys. Commun. **79** (1994) 503.
- [22] S. Jadach, W. Placzek, B.F.L. Ward, Phys. Lett. **B390** (1997) 298.
- [23] J. Hilgart, R. Kleiss and F. Le Diberder, Comput. Phys. Commun. **75** (1993) 191.
- [24] R. Engel and J. Ranft, Phys. Rev. **D54** (1996) 4244;  
R. Engel, Z. Phys. **C66** (1995) 203.
- [25] A. Buijs, W.G.J. Langeveld, M.H. Lehto and D.J. Miller, Comput. Phys. Commun. **79** (1994) 523.
- [26] J.A.M. Vermaseren, Nucl. Phys. **B229** (1983) 347.
- [27] OPAL Collaboration, K. Ackerstaff *et al.*, *Search for Anomalous Production of Di-lepton Events with Significant Missing Transverse Momentum in  $e^+e^-$  Collisions at  $\sqrt{s}=161$  and  $172$  GeV*, to be submitted to Z. Phys. C.
- [28] OPAL Collaboration, R. Akers *et al.*, Z. Phys. **C63** (1994) 197.
- [29] OPAL Collaboration, G. Alexander *et al.*, Z. Phys. **C69** (1996) 543.
- [30] ALEPH Collaboration, R. Barate *et al.*, Measurement of the W-pair cross section in  $e^+e^-$  collisions at 172 GeV, CERN-PPE/97-102, submitted to Phys. Lett. B;  
L3 Collaboration, M. Acciarri *et al.*, *Measurement of W-Pair Cross Sections in  $e^+e^-$  Interactions at  $\sqrt{s}=172$  GeV and W-Decay Branching Fractions*, CERN-PPE/97-67, submitted to Phys. Lett. B.
- [31] N. Brown and W.J. Stirling, Phys. Lett. **B252** (1990) 657;  
S. Bethke, Z. Kunszt, D. Soper and W.J. Stirling, Nucl. Phys. **B370** (1992) 310;  
S. Catani *et al.*, Phys. Lett. **B269** (1991) 432;  
N. Brown and W.J. Stirling, Z. Phys. **C53** (1992) 629.
- [32] T. Muta, R. Najima, S. Wakaizumi, Mod. Phys. Lett. **A1** (1986) 203.
- [33] G. Gustafson, U. Petterson and P.M. Zerwas, Phys. Lett. **B209** (1988) 90.
- [34] T. Sjöstrand and V.A. Khoze, Z. Phys. **C62** (1993) 281.
- [35] G. Gustafson, J. Häkkinen, Z. Phys. **C64** (1994) 659;  
C. Friberg, G. Gustafson and J. Häkkinen, Nucl. Phys. **B490** (1997) 289.
- [36] L. Lönnblad, Z. Phys. **C70** (1996) 107.
- [37] J. Ellis and K. Geiger, Phys. Rev. **D54** (1996) 1967.
- [38] J. Ellis and K. Geiger, CERN-TH/97-46.
- [39] B.R. Webber, private communication.
- [40] OPAL Collaboration, G. Alexander *et al.*, Z. Phys. **C72** (1996) 191.
- [41] S. Kluth, *QCD at LEP 1 and 2*, to be published in the proceedings of Les Rencontres de Physique de la Vallée d'Aoste, La Thuile, March 2-8 1997.
- [42] L3 Collaboration, M. Acciarri *et al.*, *Measurements of Mass, Width and Gauge Couplings of the W Boson at LEP*, CERN-PPE/97-98, submitted to Phys. Lett. B.

- [43] OPAL Collaboration, G. Alexander *et al.*, Z. Phys. **C52** (1991) 175.
- [44] OPAL Collaboration, M.Z. Akrawy *et al.*, Phys. Lett. **B253** (1990) 511.
- [45] O. Nachtmann and A. Reiter, Z. Phys. **C16** (1982) 45;  
M. Bengtsson, Z. Phys. **C42** (1989) 75.
- [46] S. Catani and M.H. Seymour, Phys. Lett. **B378** (1996) 287.
- [47] R. Barlow, J. Computat. Phys. **72** (1987) 202.

$W^+W^- \rightarrow$	Efficiency (%)
$e^+\nu_e e^-\bar{\nu}_e$	$82.4 \pm 1.1 \pm 3.2$
$e^+\nu_e \mu^-\bar{\nu}_\mu$	$83.8 \pm 0.8 \pm 2.2$
$e^+\nu_e \tau^-\bar{\nu}_\tau$	$76.8 \pm 0.9 \pm 2.2$
$\mu^+\nu_\mu \mu^-\bar{\nu}_\mu$	$86.7 \pm 1.0 \pm 2.2$
$\mu^+\nu_\mu \tau^-\bar{\nu}_\tau$	$77.0 \pm 0.9 \pm 2.2$
$\tau^+\nu_\tau \tau^-\bar{\nu}_\tau$	$60.6 \pm 1.4 \pm 4.6$

Table 1: Efficiency for selecting each  $\ell^+\nu_\ell \ell'^-\bar{\nu}_{\ell'}$  final state, evaluated using the KORALW Monte Carlo program, after correcting for detector occupancy. The errors are statistical and systematic respectively.

Source	Cross-section (fb)
ff (f = e, $\mu$ , $\tau$ , $\nu$ , q)	$9 \pm 1$
$e^+e^-f\bar{f}$ (f = e, $\mu$ , $\tau$ , q)	$32 \pm 19$
$\ell_1^+\ell_1^-\ell_2^+\ell_2^-$ ( $\ell_i = \mu, \tau$ )	$1.2 \pm 0.5$
$\ell\bar{\ell}q\bar{q}$ ( $\ell = \mu, \tau, \nu_e, \nu_\mu, \nu_\tau$ )	$0.6 \pm 0.3$
$q\bar{q}e\bar{\nu}_e$	$0.4 \pm 0.3$
$\ell_1^+\ell_1^-\nu_{\ell_2}\bar{\nu}_{\ell_2}$ ( $\ell_i = e, \mu, \tau$ ) ( $\ell_1 \neq \ell_2$ )	$18 \pm 2$
$\ell_1^+\nu_{\ell_1}\ell_2^-\bar{\nu}_{\ell_2}$ ( $\ell_i = e, \mu, \tau$ ) ( $\ell_1\ell_2 \neq \mu\tau$ )	$16 \pm 13$
Total	$77 \pm 24$

Table 2: Expected background cross-sections for different processes, assuming an average centre-of-mass energy of 172.12 GeV. The uncertainties include statistical and systematic components.

Selected as	Expected signal	Expected back.	Total	Observed
$W^+W^- \rightarrow e^+\nu_e e^-\bar{\nu}_e$	$1.3 \pm 0.1$	$0.1 \pm 0.0$	$1.4 \pm 0.1$	2
$W^+W^- \rightarrow e^+\nu_e \mu^-\bar{\nu}_\mu$	$2.6 \pm 0.1$	$0.1 \pm 0.1$	$2.7 \pm 0.1$	2
$W^+W^- \rightarrow e^+\nu_e \tau^-\bar{\nu}_\tau$	$2.3 \pm 0.1$	$0.2 \pm 0.1$	$2.6 \pm 0.1$	1
$W^+W^- \rightarrow \mu^+\nu_\mu \mu^-\bar{\nu}_\mu$	$1.4 \pm 0.1$	$0.0 \pm 0.0$	$1.5 \pm 0.1$	0
$W^+W^- \rightarrow \mu^+\nu_\mu \tau^-\bar{\nu}_\tau$	$2.2 \pm 0.1$	$0.1 \pm 0.1$	$2.3 \pm 0.1$	1
$W^+W^- \rightarrow \tau^+\nu_\tau \tau^-\bar{\nu}_\tau$	$0.9 \pm 0.1$	$0.1 \pm 0.0$	$1.0 \pm 0.1$	2
$W^+W^- \rightarrow q\bar{q}e\bar{\nu}_e$	$16.8 \pm 0.4$	$1.2 \pm 0.4$	$18.0 \pm 0.6$	19
$W^+W^- \rightarrow q\bar{q}\mu\bar{\nu}_\mu$	$17.4 \pm 0.4$	$0.6 \pm 0.1$	$17.9 \pm 0.4$	16
$W^+W^- \rightarrow q\bar{q}\tau\bar{\nu}_\tau$	$13.5 \pm 0.4$	$2.7 \pm 0.7$	$16.2 \pm 0.8$	20
$W^+W^- \rightarrow q\bar{q}q\bar{q}$	$41.3 \pm 1.5$	$13.1 \pm 2.0$	$54.4 \pm 2.5$	54.1
Combined	$99.7 \pm 2.6$	$18.3 \pm 2.2$	$117.9 \pm 3.4$	117.1

Table 3: Observed numbers of candidate events in each  $W^+W^-$  decay channel for an integrated luminosity of  $10.36 \pm 0.06 \text{ pb}^{-1}$  at  $172.12 \pm 0.06 \text{ GeV}$ , together with expected numbers of signal and background events, assuming  $M_W = 80.33 \pm 0.15 \text{ GeV}$ . The numbers for the  $W^+W^- \rightarrow q\bar{q}q\bar{q}$  channel are the sums of the event weights for the 99 events passing the preselection (see text). The predicted numbers of signal events include systematic uncertainties from the efficiency, luminosity, beam energy,  $W^+W^-$  cross-section and  $M_W$ , while the background estimates include selection and luminosity uncertainties. The errors on the combined numbers account for correlations.

Selected as	Generated as		
	$W^+W^- \rightarrow q\bar{q}e\bar{\nu}_e$	$W^+W^- \rightarrow q\bar{q}\mu\bar{\nu}_\mu$	$W^+W^- \rightarrow q\bar{q}\tau\bar{\nu}_\tau$
$W^+W^- \rightarrow q\bar{q}e\bar{\nu}_e$	$85.1 \pm 0.9\%$	$0.1 \pm 0.1\%$	$3.9 \pm 0.3\%$
$W^+W^- \rightarrow q\bar{q}\mu\bar{\nu}_\mu$	$0.2 \pm 0.1\%$	$87.6 \pm 0.8\%$	$4.4 \pm 0.3\%$
$W^+W^- \rightarrow q\bar{q}\tau\bar{\nu}_\tau$	$4.7 \pm 0.5\%$	$5.2 \pm 0.5\%$	$61.4 \pm 1.2\%$

Table 4: Selection efficiencies for the different  $W^+W^- \rightarrow q\bar{q}\ell\bar{\nu}_\ell$  channels after event categorisation showing the cross contamination in each selection. The efficiencies, based on KORALW, have been corrected for differences between data and Monte Carlo. The errors include both statistical and systematic uncertainties.

Source of uncertainty	Signal efficiency error (%)		
	$W^+W^- \rightarrow q\bar{q}e\bar{\nu}_e$	$W^+W^- \rightarrow q\bar{q}\mu\bar{\nu}_\mu$	$W^+W^- \rightarrow q\bar{q}\tau\bar{\nu}_\tau$
Statistical	0.3	0.3	0.5
Comparison of MC models	0.4	0.2	0.2
Data/Monte Carlo	0.6	0.4	0.7
$M_W$ dependence ( $\pm 150 \text{ MeV}$ )	0.1	0.3	0.1
Beam energy dependence	0.5	0.5	0.8
Total	0.9	0.8	1.2

Table 5: Sources of uncertainty on the  $W^+W^- \rightarrow q\bar{q}\ell\bar{\nu}_\ell$  selection efficiencies.

Source	Background cross-sections (fb)		
	$W^+W^- \rightarrow q\bar{q}e\bar{\nu}_e$	$W^+W^- \rightarrow q\bar{q}\mu\bar{\nu}_\mu$	$W^+W^- \rightarrow q\bar{q}\tau\bar{\nu}_\tau$
$q\bar{q}e\bar{\nu}_e$	$0 \pm 25$	$1 \pm 2$	$42 \pm 19$
$q\bar{q}f\bar{f}$	$1 \pm 1$	$24 \pm 5$	$40 \pm 4$
$e^+e^-f\bar{f}$	$82 \pm 27$	$6 \pm 2$	$31 \pm 10$
$Z^0/\gamma \rightarrow q\bar{q}$	$29 \pm 13$	$23 \pm 10$	$143 \pm 61$
$Z^0/\gamma \rightarrow \tau^+\tau^-$	$6 \pm 1$	$1 \pm 1$	$1 \pm 1$
Combined	$118 \pm 39$	$55 \pm 12$	$257 \pm 65$

Table 6: Background cross-sections for the  $W^+W^- \rightarrow q\bar{q}\ell\bar{\nu}_\ell$  selections in fb. The four-fermion backgrounds have been split into final states containing no electron ( $q\bar{q}f\bar{f}$ ), where f refers to a fermion other than an electron, one electron ( $q\bar{q}e\bar{\nu}_e$ ) and two electrons ( $e^+e^-f\bar{f}$ ). The background from  $e^+e^-f\bar{f}$  final states includes two-photon processes. The  $Z^0/\gamma \rightarrow q\bar{q}$  background includes the uncertainty on the background correction factor of  $1.2 \pm 0.5$ . All errors include both statistical and systematic contributions.

	Background cross-section (fb)	
	Likelihood cut $\sigma_{\text{bgd}}$	Event weight $\sigma_{\text{bgd}}^{\text{pre}}\bar{w}_b$
$q\bar{q}\ell\bar{\nu}_\ell$	$1 \pm 1$	$1 \pm 1$
$q\bar{q}$	$1237 \pm 281$	$1142 \pm 181$
$q\bar{q}f\bar{f}(f \neq e)$	$127 \pm 46$	$108 \pm 47$
$q\bar{q}e^+e^-$	$18 \pm 3$	$14 \pm 3$
Combined	$1380 \pm 280$	$1260 \pm 190$

Table 7: Background cross-sections for the  $W^+W^- \rightarrow q\bar{q}q\bar{q}$  channel in fb, assuming an average centre-of-mass energy of 172.12 GeV. The uncertainties include systematic contributions.

Source of uncertainty	Selection			
	Likelihood cut		Event weight	
	$\Delta\epsilon_{\text{sig}}$ (%)	$\Delta\sigma_{\text{bgd}}$ (pb)	$\Delta(\epsilon_{\text{sig}}^{\text{pre}}\bar{w}_s)$ (%)	$\Delta(\sigma_{\text{bgd}}^{\text{pre}}\bar{w}_b)$ (pb)
Monte Carlo models	0.30	0.08	0.21	0.07
QCD parameter variation	0.93	0.12	1.14	0.12
Data/Monte Carlo $\sqrt{s} = 172$ GeV	0.70	0.18	1.59	0.02
Data/Monte Carlo $\sqrt{s} = 91.2$ GeV	—	0.11	—	0.09
Beam energy dependence	0.25	0.11	0.34	0.06
$M_W$ dependence ( $\pm 150$ MeV)	0.03	0.00	0.17	0.00
Binning effects	0.15	0.04	0.32	0.02
Total	1.24	0.28	2.03	0.18

Table 8: Sources of systematic error on the signal efficiency and expected background cross-section for the  $W^+W^- \rightarrow q\bar{q}q\bar{q}$  likelihood selection, which is used in the W mass and event properties analyses. The systematic errors on the event weight based quantities used for the cross-section measurement are also given. The total is the quadrature sum of all uncertainties.



$W^+W^- \rightarrow q\bar{q}q\bar{q}$ Selection	Expected signal	Expected back.	Total	Observed
Preselection	$53.0 \pm 1.5$	$46.7 \pm 2.1$	$99.7 \pm 2.6$	99
Likelihood cut	$46.8 \pm 1.2$	$14.3 \pm 2.9$	$61.0 \pm 3.1$	57
Event weight	$41.3 \pm 1.5$	$13.1 \pm 2.0$	$54.4 \pm 2.5$	$54.1 \pm 6.6$

Table 9: Comparison of expected and observed numbers of events in the  $W^+W^- \rightarrow q\bar{q}q\bar{q}$  channel, based on an integrated luminosity of  $10.36 \text{ pb}^{-1}$ ,  $M_W = 80.33 \text{ GeV}$  and a total  $W^+W^-$  production cross-section of  $12.4 \text{ pb}$ . Results are given for the preselection cuts, for the likelihood cut selection used in the mass and event properties analyses and for the event weight analysis used in the cross-section measurement. The errors on the expected numbers of events include contributions arising from luminosity,  $\sigma_{WW}$  and  $M_W$  uncertainties. The error on the observed event weight is calculated as the square root of the sum of the event weights squared for the 99 events passing the preselection.

Event selection	Efficiencies[%] for $W^+W^- \rightarrow$							$q\bar{q}e\bar{\nu}_e$	$q\bar{q}\mu\bar{\nu}_\mu$	$q\bar{q}\tau\bar{\nu}_\tau$	$q\bar{q}q\bar{q}$
	$e^+\nu_e e^-\bar{\nu}_e$	$e^+\nu_e \mu^-\bar{\nu}_\mu$	$e^+\nu_e \tau^-\bar{\nu}_\tau$	$\mu^+\nu_\mu \mu^-\bar{\nu}_\mu$	$\mu^+\nu_\mu \tau^-\bar{\nu}_\tau$	$\tau^+\nu_\tau \tau^-\bar{\nu}_\tau$					
$e^+\nu_e e^-\bar{\nu}_e$	72.3	0.1	5.9	0.0	0.0	0.2	0.0	0.0	0.0	0.0	
$e^+\nu_e \mu^-\bar{\nu}_\mu$	1.9	74.1	4.6	0.3	5.3	1.0	0.0	0.0	0.0	0.0	
$e^+\nu_e \tau^-\bar{\nu}_\tau$	7.6	4.3	62.8	0.0	1.3	9.0	0.0	0.0	0.0	0.0	
$\mu^+\nu_\mu \mu^-\bar{\nu}_\mu$	0.0	1.0	0.1	78.3	6.4	0.3	0.0	0.0	0.0	0.0	
$\mu^+\nu_\mu \tau^-\bar{\nu}_\tau$	0.1	3.8	0.4	7.9	60.3	5.9	0.0	0.0	0.0	0.0	
$\tau^+\nu_\tau \tau^-\bar{\nu}_\tau$	0.3	0.3	2.9	0.2	3.7	44.3	0.0	0.0	0.0	0.0	
$q\bar{q}e\bar{\nu}_e$	0.0	0.0	0.3	0.0	0.0	0.0	85.1	0.1	3.9	0.0	
$q\bar{q}\mu\bar{\nu}_\mu$	0.0	0.0	0.0	0.0	0.0	0.0	0.2	87.6	4.4	0.1	
$q\bar{q}\tau\bar{\nu}_\tau$	0.0	0.0	0.0	0.0	0.0	0.3	4.7	5.2	61.4	0.2	
$q\bar{q}q\bar{q}$	0.0	0.0	0.0	0.0	0.0	0.0	0.0	0.0	0.4	70.3	

Table 10: Efficiency matrix,  $\epsilon_{ij}$ , for the 172 GeV event selections determined using KORALW (CC03) Monte Carlo events. Each entry represents the percentage of generated events in decay channel  $i$  which are accepted by the selection for channel  $j$ . The numbers for the  $q\bar{q}\ell\bar{\nu}_\ell$  selections have been corrected for differences between data and Monte Carlo. The  $q\bar{q}q\bar{q}$  numbers are calculated as the preselection efficiency multiplied by the average event weight for each event type. The  $\ell^+\nu_\ell\ell'^-\bar{\nu}_{\ell'}$  efficiencies have been corrected by a factor 0.99 to account for detector occupancy.

Fitted parameter	Fit assumptions :		
		Lepton universality	SM branching fractions
Br(W $\rightarrow$ e $\bar{\nu}_e$ )	$0.098^{+0.022}_{-0.020} \pm 0.003$		
Br(W $\rightarrow$ $\mu\bar{\nu}_\mu$ )	$0.073^{+0.019}_{-0.017} \pm 0.002$		
Br(W $\rightarrow$ $\tau\bar{\nu}_\tau$ )	$0.140^{+0.030}_{-0.028} \pm 0.005$		
Br(W $\rightarrow$ $\ell\bar{\nu}_\ell$ )		$0.101^{+0.011}_{-0.010} \pm 0.002$	
Br(W $\rightarrow$ q $\bar{q}$ )	$0.690^{+0.030}_{-0.032} \pm 0.007$	$0.698^{+0.030}_{-0.032} \pm 0.007$	
$\sigma_{\text{WW}}(161 \text{ GeV})$ [pb]	$3.9^{+1.0}_{-0.9} \pm 0.2$	$3.7^{+0.9}_{-0.8} \pm 0.2$	$3.6^{+0.9}_{-0.8} \pm 0.2$
$\sigma_{\text{WW}}(172 \text{ GeV})$ [pb]	$12.6 \pm 1.3 \pm 0.4$	$12.3 \pm 1.3 \pm 0.4$	$12.3 \pm 1.3 \pm 0.3$

Table 11: Summary of cross-section and branching fraction results from the combined 161.3 GeV and 172.12 GeV data. The results from three different fits described in the text are shown. The correlations between the branching fraction measurements from the fit without the assumption of lepton universality are less than 30%.

Channel	Selected events in fit range	
	BW method	RW method
W <sup>+</sup> W <sup>-</sup> $\rightarrow$ q $\bar{q}$ q $\bar{q}$ (1 jet-jet pairing per event)	30	22
W <sup>+</sup> W <sup>-</sup> $\rightarrow$ q $\bar{q}$ q $\bar{q}$ (2 jet-jet pairings per event)	12	21
W <sup>+</sup> W <sup>-</sup> $\rightarrow$ q $\bar{q}$ e $\bar{\nu}_e$ + W <sup>+</sup> W <sup>-</sup> $\rightarrow$ q $\bar{q}$ $\mu\bar{\nu}_\mu$	28	31
W <sup>+</sup> W <sup>-</sup> $\rightarrow$ q $\bar{q}$ $\tau\bar{\nu}_\tau$	14	17
Total	84	91

Table 12: Numbers of selected events in each channel for use in the W mass determination. For the W<sup>+</sup>W<sup>-</sup>  $\rightarrow$  q $\bar{q}$ q $\bar{q}$  process, up to two jet-jet pairings are used in each event. For the BW method, only events with a reconstructed mass of  $40 \text{ GeV} < m_{\text{rec}} < 84 \text{ GeV}$  are included, while for the RW method, reconstructed masses from 65 GeV up to the kinematic limit are used.

	W <sup>+</sup> W <sup>-</sup> $\rightarrow$ q $\bar{q}$ q $\bar{q}$	W <sup>+</sup> W <sup>-</sup> $\rightarrow$ q $\bar{q}$ $\ell\bar{\nu}_\ell$	combined
Fitted mass (GeV)	$80.19 \pm 0.39$	$80.80 \pm 0.37$	$80.50 \pm 0.27$
MC correction (GeV)	$-0.19 \pm 0.01$	$-0.32 \pm 0.01$	$-0.26 \pm 0.01$
Corrected mass (GeV)	$80.01 \pm 0.43 \pm 0.14$	$80.48 \pm 0.40 \pm 0.12$	$80.24 \pm 0.30 \pm 0.10$

Table 13: Summary of fit results and Monte Carlo corrections to  $M_W$  for the BW fit method. The errors on the fitted mass and corrections are statistical only, while for the corrected mass the statistical and systematic errors are both listed (see Section 5.4 for details).

Systematic errors (MeV)	BW-fit to $M_W$ fixed width			RW-fit to $M_W$ SM constrained width			RW-fit to $M_W$ and $\Gamma_W$	
	$q\bar{q}q\bar{q}$	$q\bar{q}\ell\bar{\nu}_\ell$	comb.	$q\bar{q}q\bar{q}$	$q\bar{q}\ell\bar{\nu}_\ell$	comb.	$M_W$	$\Gamma_W$
Beam Energy	27	27	27	30	30	30	30	15
ISR	22	22	22	20	20	20	20	61
Hadronisation	16	16	12	52	26	20	21	52
Four-fermion	42	37	37	42	48	42	35	70
Detector Effects	67	87	54	62	76	48	48	98
Fit procedure and Background	33	65	36	32	28	25	25	85
Colour Reconnection and Bose-Einstein	100	0	50	100	0	50	50	50
Total systematic error	137	121	96	144	104	94	92	175

Table 14: Summary of the systematic errors for the various fit methods. For the one-parameter fits to determine  $M_W$ , uncertainties are given for the fits to  $W^+W^- \rightarrow q\bar{q}q\bar{q}$ ,  $W^+W^- \rightarrow q\bar{q}\ell\bar{\nu}_\ell$  and for the combined sample. For the two-parameter fit, the uncertainties for  $M_W$  and  $\Gamma_W$  are listed separately only for the fits to the combined sample.

Systematic variation	$\langle n_{\text{ch}}^{4q} \rangle$	$\langle n_{\text{ch}}^{qq\ell\nu} \rangle$	$\Delta\langle n_{\text{ch}} \rangle$	$\langle x_p^{4q} \rangle$ $\times 10^2$	$\langle x_p^{qq\ell\nu} \rangle$ $\times 10^2$	$\Delta\langle x_p \rangle$ $\times 10^2$	$\langle (1-T)^{4q} \rangle$	$\langle  y^{4q}  \rangle$
$W^+W^-$ model dependence	0.30	0.16	0.19	0.018	0.035	0.027	0.005	0.006
Track quality cuts	0.28	0.18	0.26	0.043	0.055	0.065	—	0.011
Event selection	0.15	0.25	0.52	0.047	0.067	0.020	0.008	0.017
Background scaling	0.05	0.06	0.15	0.018	0.005	0.054	0.008	0.011
Z/ $\gamma$ background	0.27	0.03	0.22	0.012	0.005	0.017	0.007	0.005
Other backgrounds	0.06	0.07	0.11	0.017	0.009	0.022	0.001	0.002
Beam energy dependence	0.15	0.01	0.18	0.001	0.015	0.016	0.004	0.002
Unfolding procedure	0.15	0.22	0.29	0.025	0.051	0.026	0.015	0.001
Total	0.56	0.42	0.75	0.076	0.11	0.10	0.021	0.025

Table 15: Individual contributions to the systematic uncertainties on the average event properties.

# OPAL

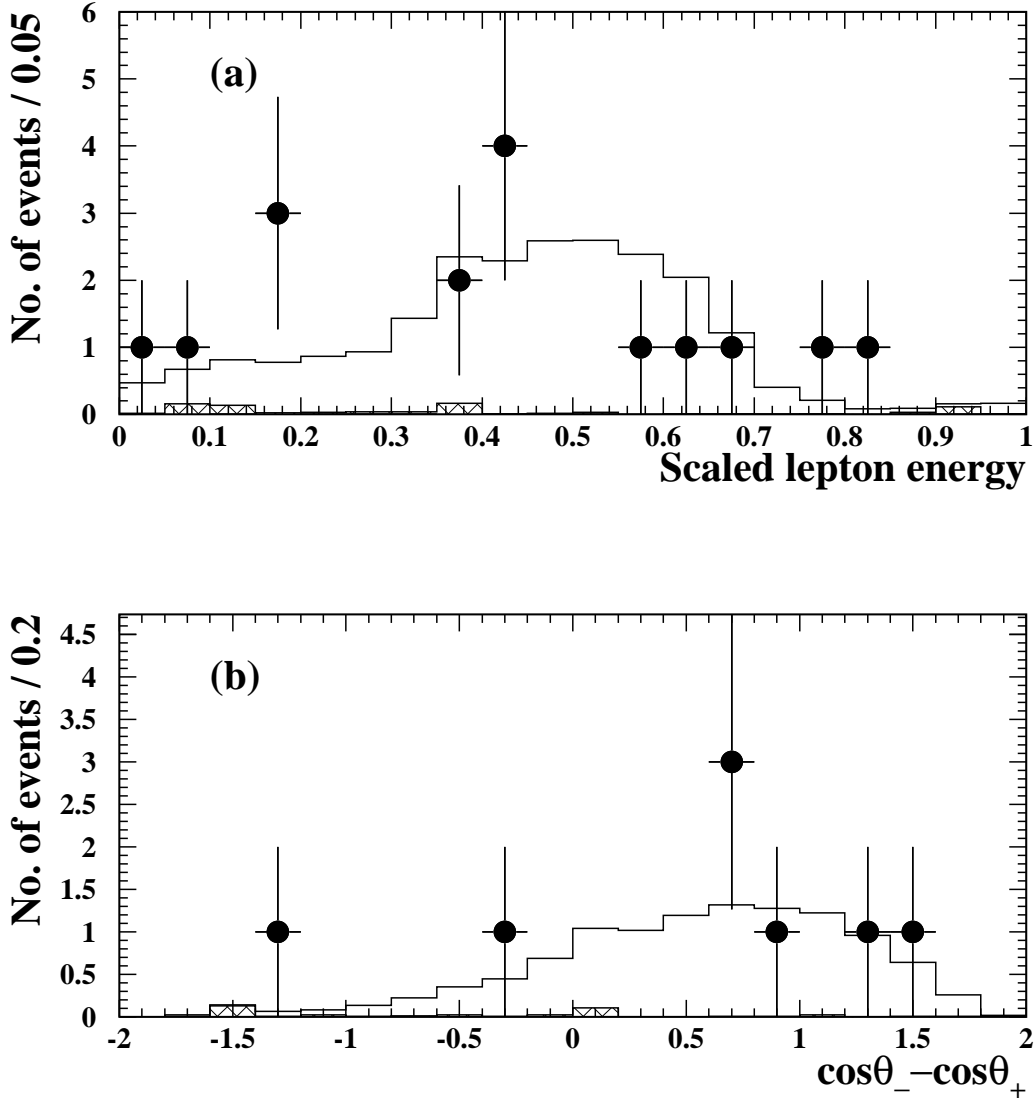


Figure 1: Distributions of kinematic variables for selected  $W^+W^- \rightarrow \ell^+\nu_\ell\ell'^-\bar{\nu}_{\ell'}$  events, showing: (a) the lepton energy divided by the beam energy, and (b)  $\cos\theta_- - \cos\theta_+$ . The data are shown as points with error bars. The Monte Carlo prediction for the sum of  $W^+W^-$  and all other Standard Model processes is shown as the open histogram, while the non- $W^+W^-$  processes are represented by a doubly hatched histogram. The Monte Carlo samples have been normalised to the collected integrated luminosity of  $10.36 \text{ pb}^{-1}$ .

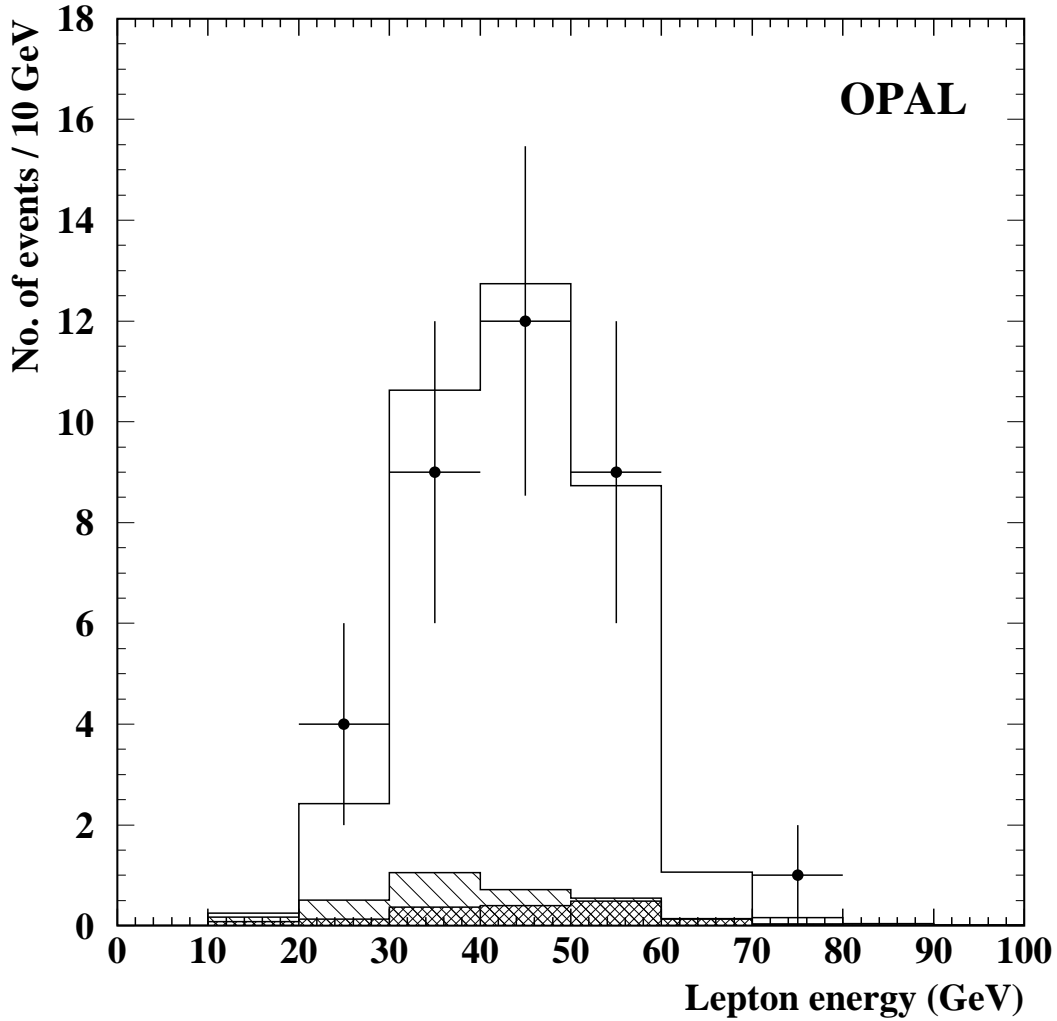


Figure 2: The energy of the lepton for events selected as  $W^+W^- \rightarrow q\bar{q}e\bar{\nu}_e$  or  $W^+W^- \rightarrow q\bar{q}\mu\bar{\nu}_\mu$  after categorisation. For electrons this is determined using the ECAL energy and for muons using the track momentum. The open histogram shows the Monte Carlo prediction (PYTHIA) for an integrated luminosity of  $10.36 \text{ pb}^{-1}$  and total  $W^+W^-$  cross-section of  $12.4 \text{ pb}$ . The contribution from  $W^+W^- \rightarrow q\bar{q}\tau\bar{\nu}_\tau$  decays is shown as the single hatched histogram and the contribution from background processes as the doubly hatched histogram. The data are shown as the points with error bars.

## OPAL

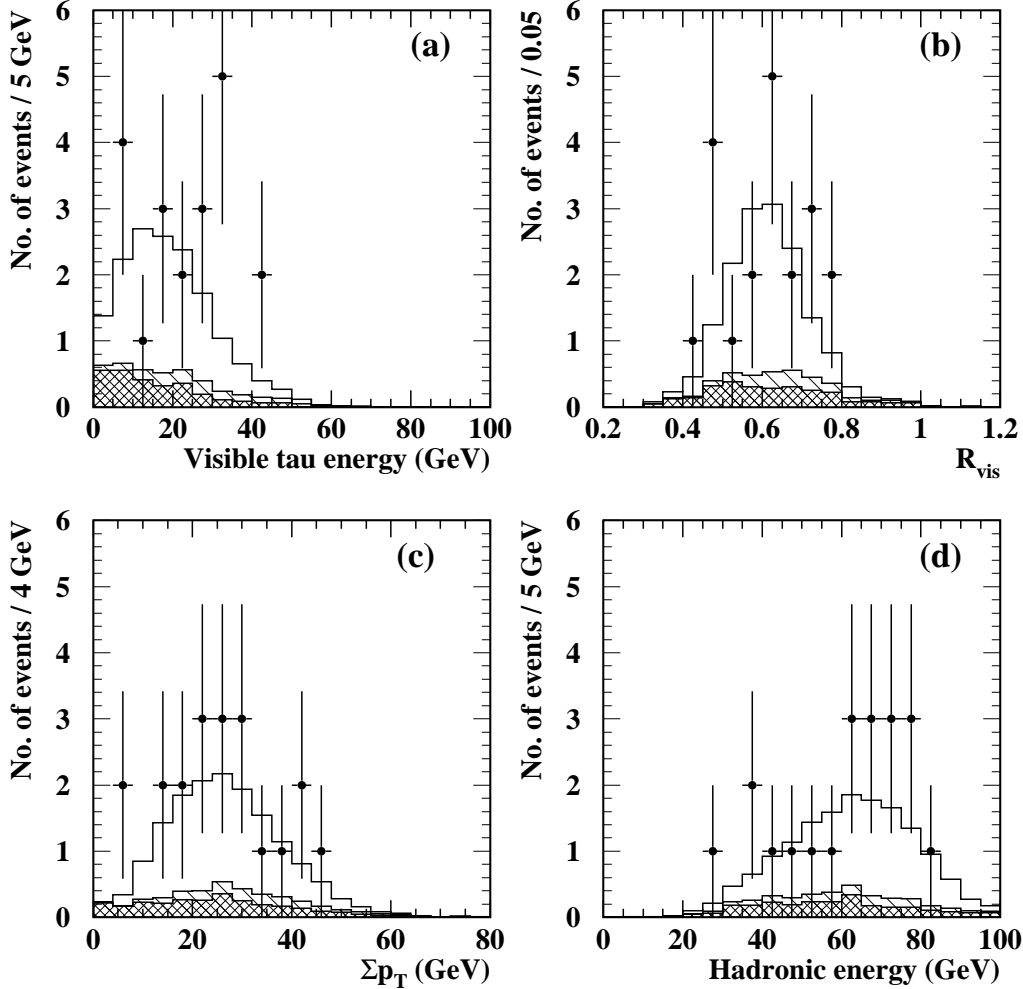


Figure 3: Distributions of kinematic variables for selected  $W^+W^- \rightarrow q\bar{q}\tau\bar{\nu}_\tau$  events, showing: (a) estimated visible energy of the tau decay, excluding the energy of the neutrino(s), (b) visible energy of the event divided by  $\sqrt{s} R_{vis}$ , (c) net transverse momentum  $\Sigma p_T$  of the event, and (d) uncorrected energy of the two hadronic jets in the event, calculated using tracks and unassociated ECAL clusters, when the jet containing the tau candidate is excluded (this variable is not used in the likelihood). The open histogram shows the Monte Carlo prediction (PYTHIA) for an integrated luminosity of  $10.36 \text{ pb}^{-1}$  and total  $W^+W^-$  cross-section of  $12.4 \text{ pb}$ . The contribution from  $W^+W^- \rightarrow q\bar{q}e\bar{\nu}_e$  and  $W^+W^- \rightarrow q\bar{q}\mu\bar{\nu}_\mu$  decays is shown by the single hatched histogram and the contribution from background sources as the doubly hatched histogram. The data are shown as the points with error bars.

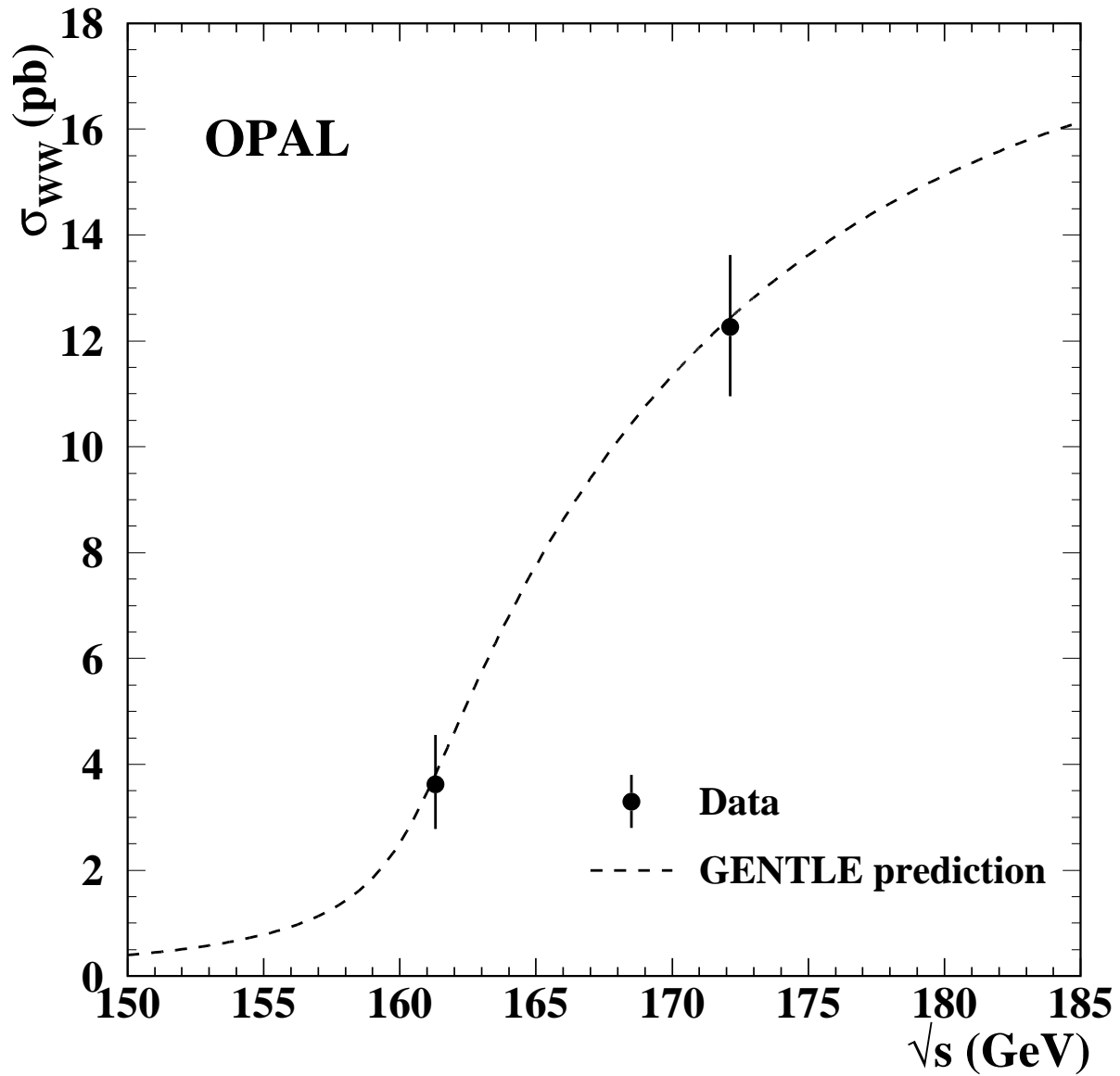


Figure 4: The dependence of  $\sigma_{WW}$  on  $\sqrt{s}$ , as predicted by GENTLE for  $M_W = 80.33$  GeV. The  $W^+W^-$  cross-sections measured at  $\sqrt{s} = 172.12$  GeV (this paper) and at  $\sqrt{s} = 161.3$  GeV [5], are shown. The error bars include statistical and systematic contributions.

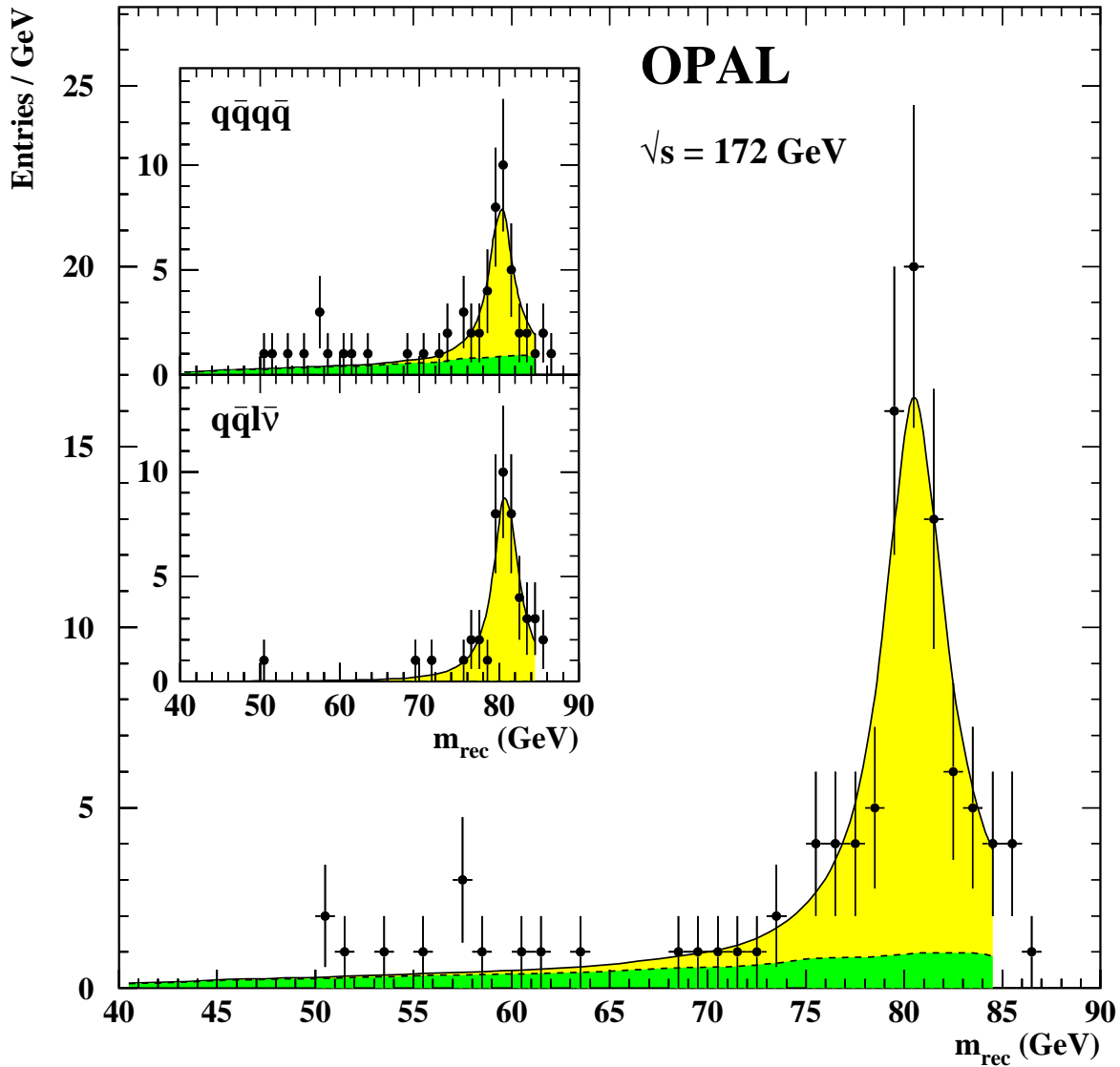


Figure 5: Reconstructed mass distributions for the data. The main plot shows the  $W^+W^- \rightarrow q\bar{q}q\bar{q}$  and  $W^+W^- \rightarrow q\bar{q}\ell\nu_\ell$  samples combined, and the insets present them separately. The solid curves display the results of unbinned maximum likelihood fits to a relativistic Breit-Wigner signal plus background in the range 40-84 GeV as described in the text. The background function alone is shown by the dark shaded region.



## OPAL Monte Carlo

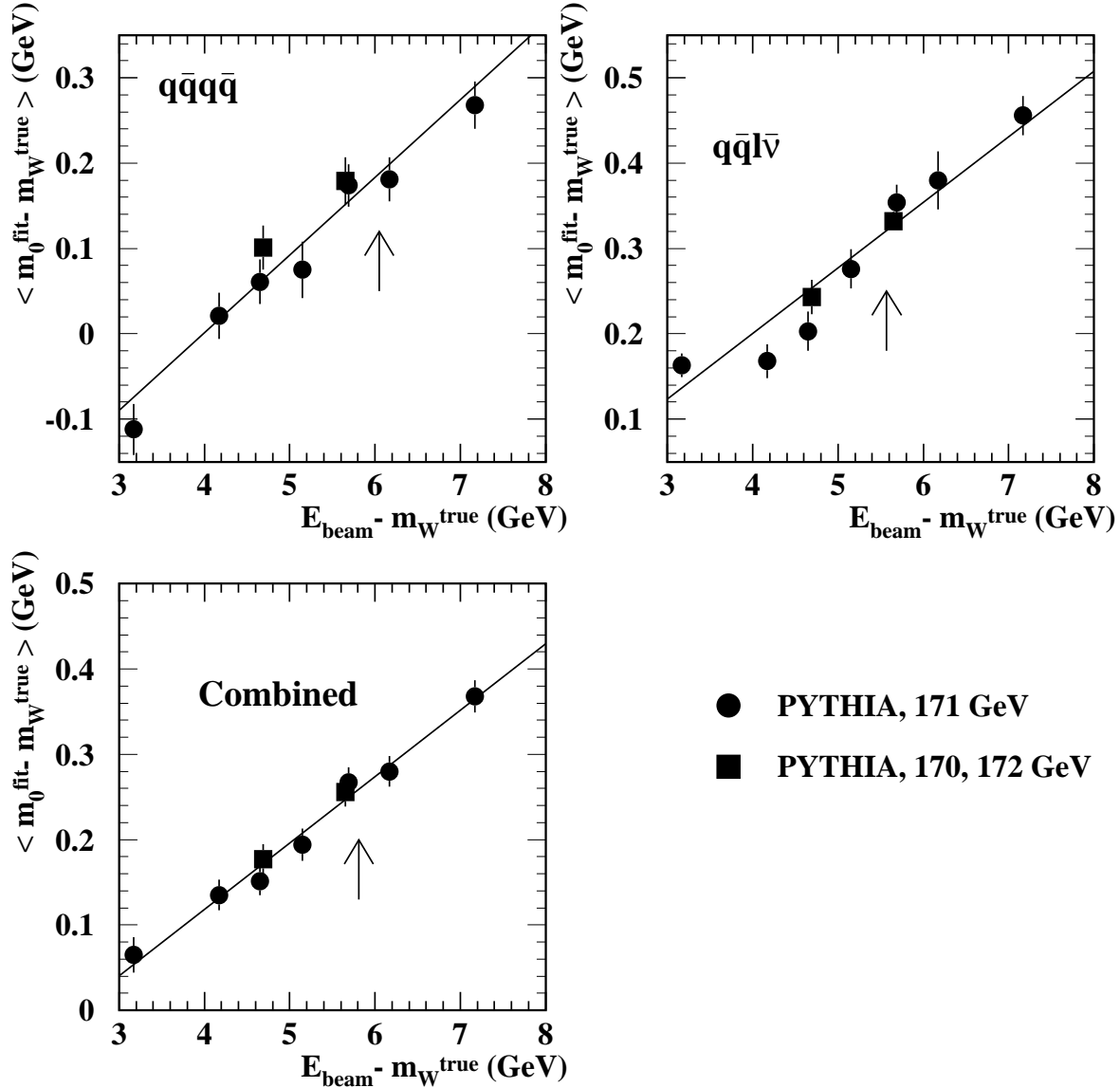


Figure 6: Mean of the difference between fitted and true mass from fits to many Monte Carlo sub-samples, for PYTHIA Monte Carlo events generated with various input W masses and at different beam energies, plotted as a function of the difference between beam energy and true mass. The  $W^+W^- \rightarrow q\bar{q}q\bar{q}$  and  $W^+W^- \rightarrow q\bar{q}\ell\bar{\nu}_\ell$  samples are shown separately, as well as both combined. The lines represent fits to the points, with parameters given in the text. The arrows indicate the actual corrections applied.

## OPAL Monte Carlo

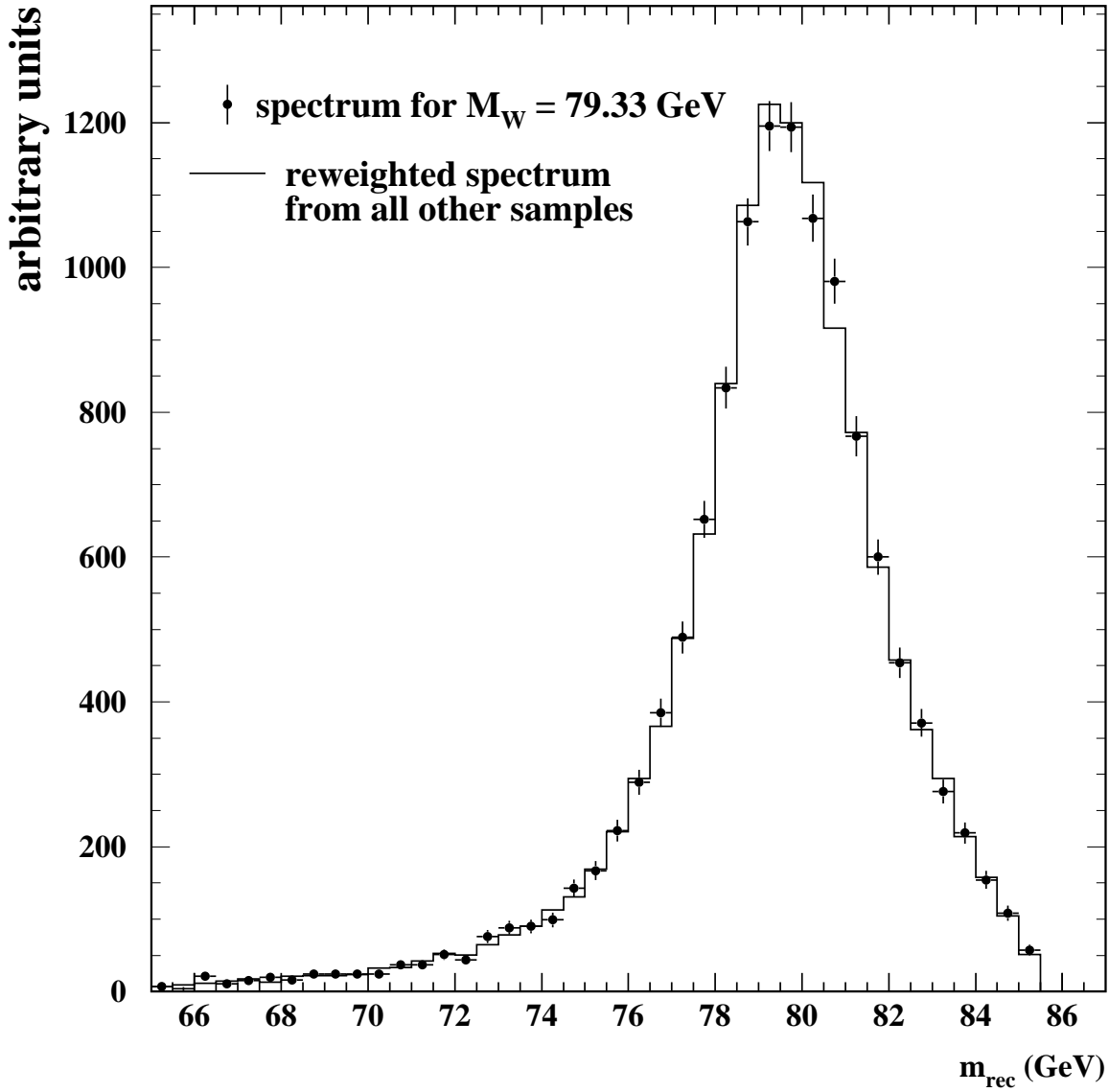


Figure 7: Illustration of the reweighting procedure for the reconstructed mass spectrum of the  $W^+W^- \rightarrow q\bar{q}\ell\nu_\ell$  signal events. The spectrum of a sample produced with  $M_W = 79.33$  GeV is compared with the reweighted spectrum obtained from samples with W boson masses between  $M_W = 78.33$  GeV and  $M_W = 82.33$  GeV. Only samples produced with the same Monte Carlo generator (PYTHIA) are used for this comparison and the  $M_W = 79.33$  GeV sample has not been included in the reweighting procedure. The Monte Carlo statistics for the final fit including all samples, will be larger by more than a factor of 3.

# OPAL

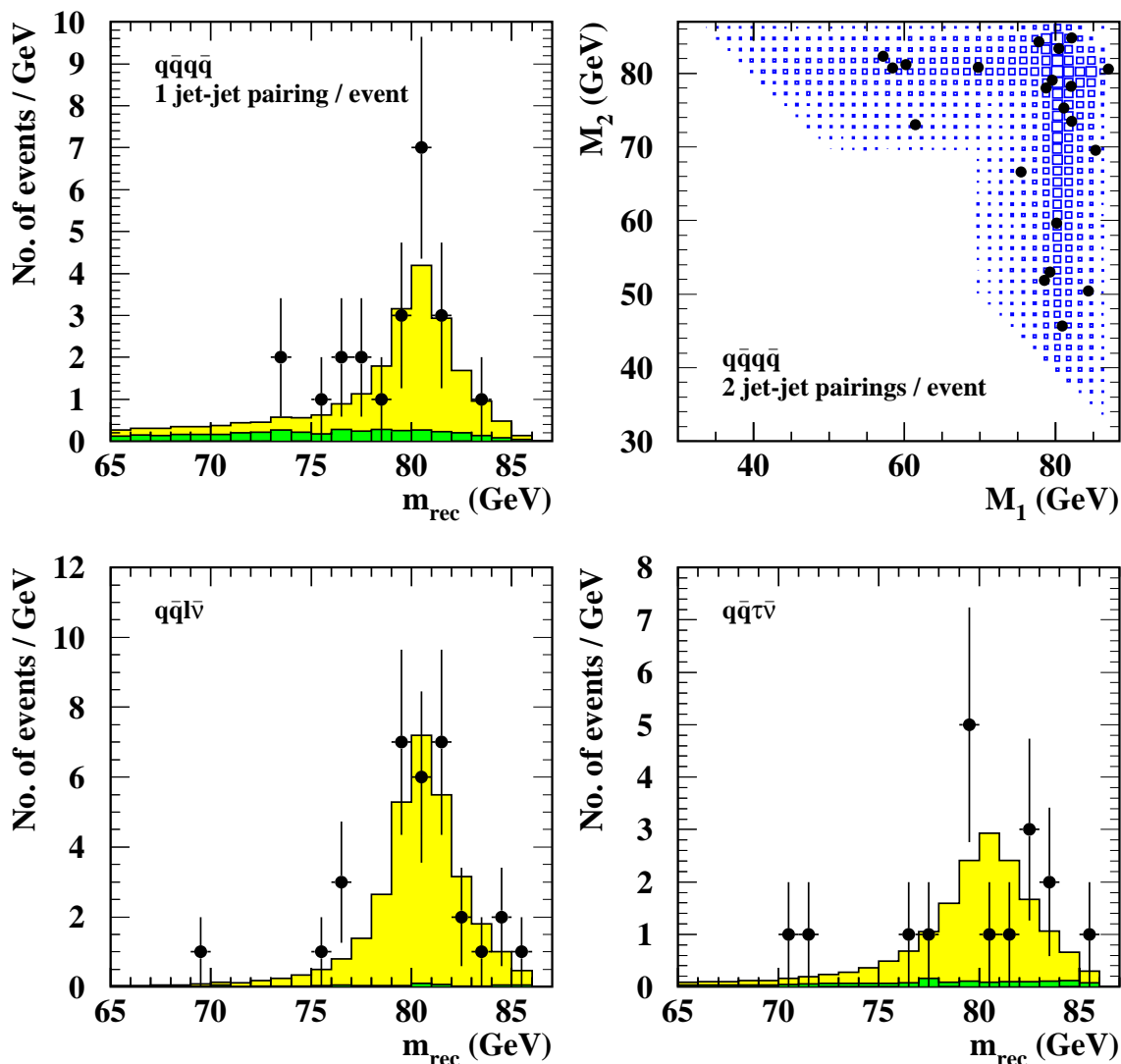


Figure 8: Fits to the mass spectra of the different channels using the reweighting method. The dots represent the data, the lightly shaded histograms the result from the fit for  $(M_W, \Gamma_W)$  and the darkly shaded ones the background contributions to it. For the  $W^+W^- \rightarrow q\bar{q}q\bar{q}$  candidates in which two jet-jet pairings per event are used, the underlying histogram represents the fit result. For clarity, the bin size used for the one-dimensional histograms is twice that used for the fit.

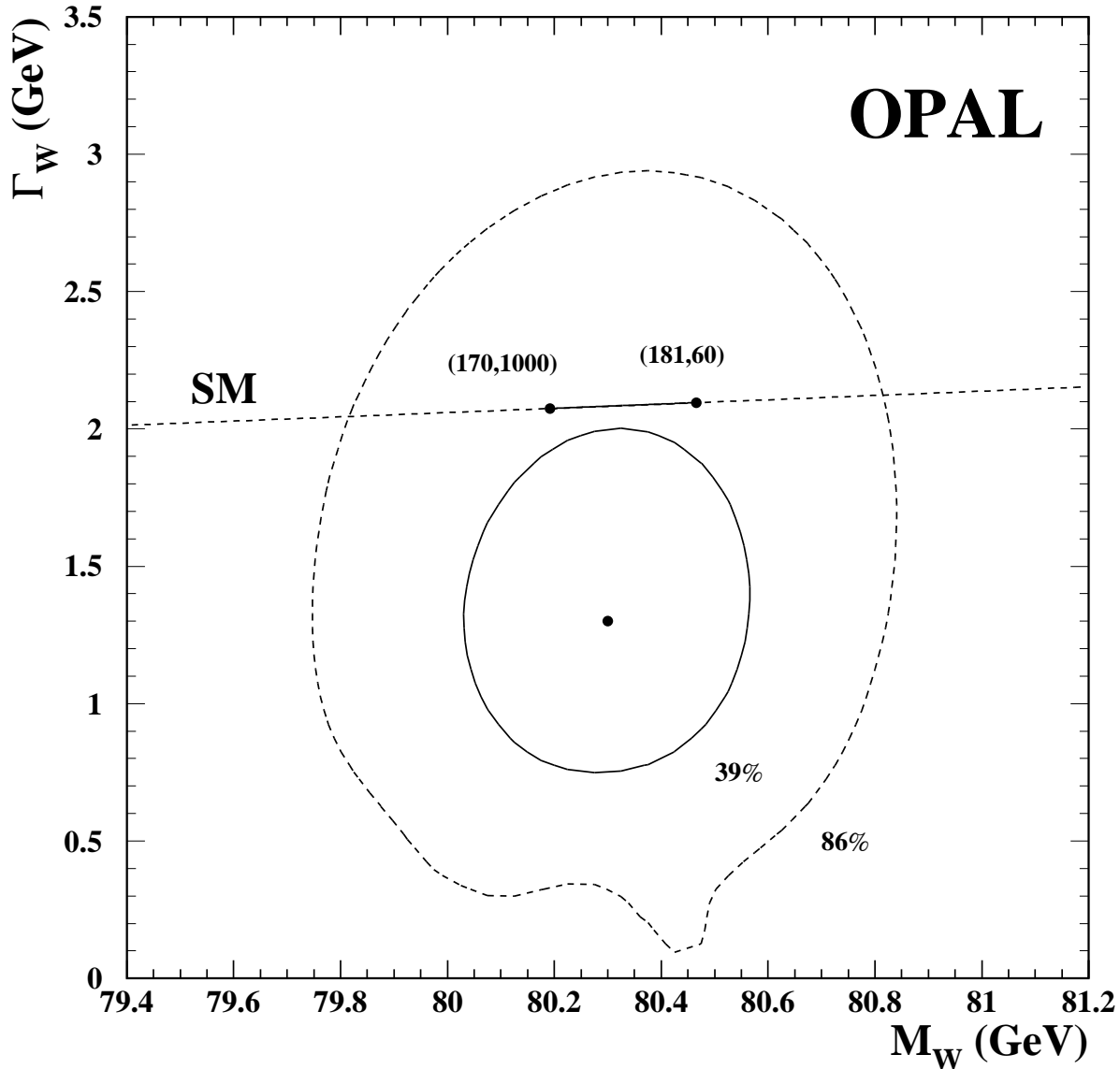


Figure 9: The 39% and 86% contour levels of the two-parameter fit using the reweighting method. The projections of these contours onto the axes give the one and two standard deviation errors quoted in the text. The straight dashed line gives the dependence of the width on the mass according to the Standard Model. The one-parameter fit for the mass alone is constrained to this line. The solid line is the Standard Model prediction for variations of  $(M_{\text{top}}, M_{\text{Higgs}})$ , both given in GeV. For small fitted values of  $\Gamma_W$ , the 86% contour is very sensitive to the particular distribution of masses observed in the data.

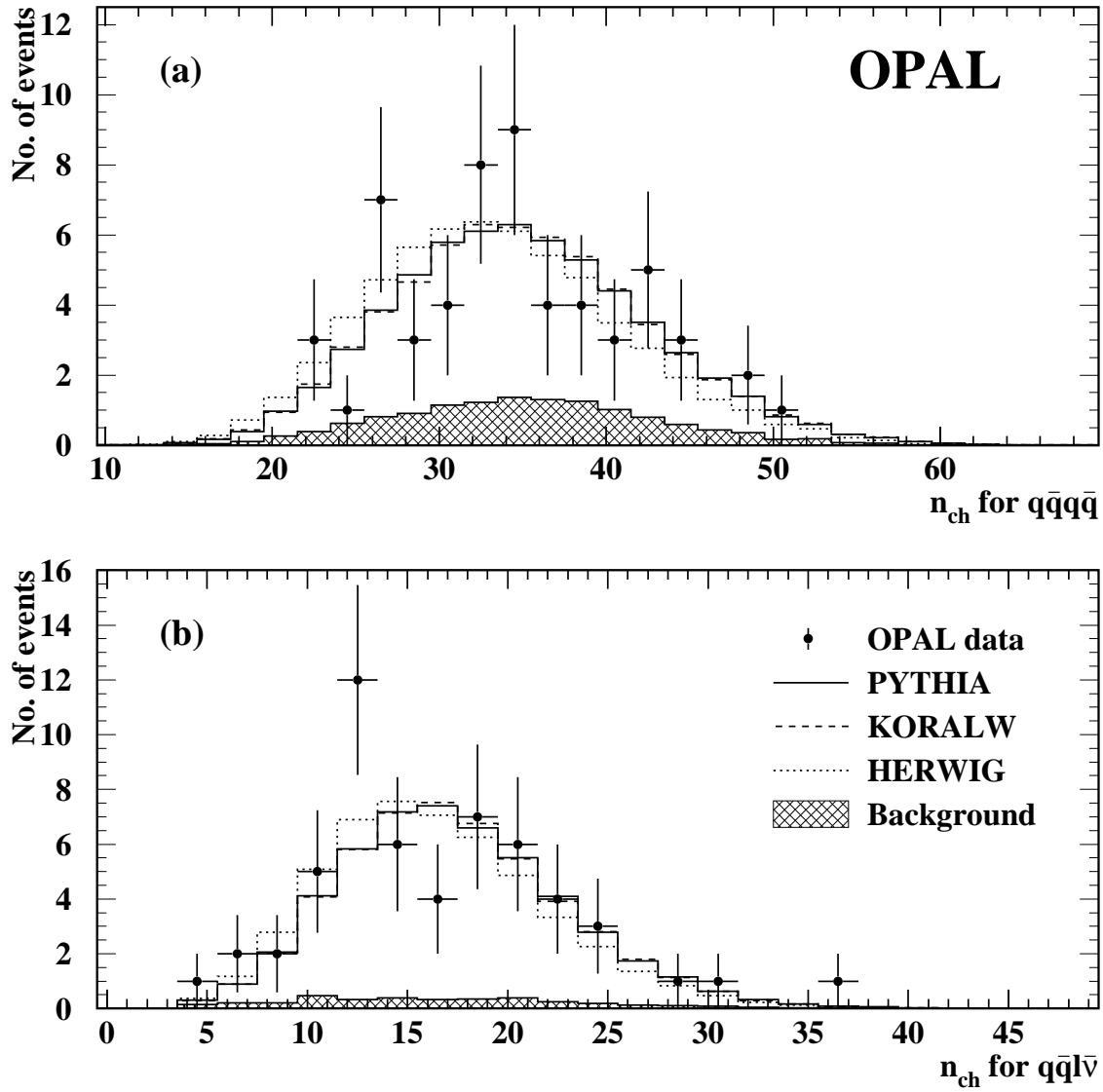


Figure 10: Uncorrected charged multiplicity distributions for (a)  $W^+W^- \rightarrow q\bar{q}q\bar{q}$  events and (b) the hadronic part of  $W^+W^- \rightarrow q\bar{q}l\nu_{\bar{l}}$  events. The points indicate the data, the histograms show the total expected signal and background contribution for various signal models, and the hatched histogram shows the expected background. The bins are two units wide.

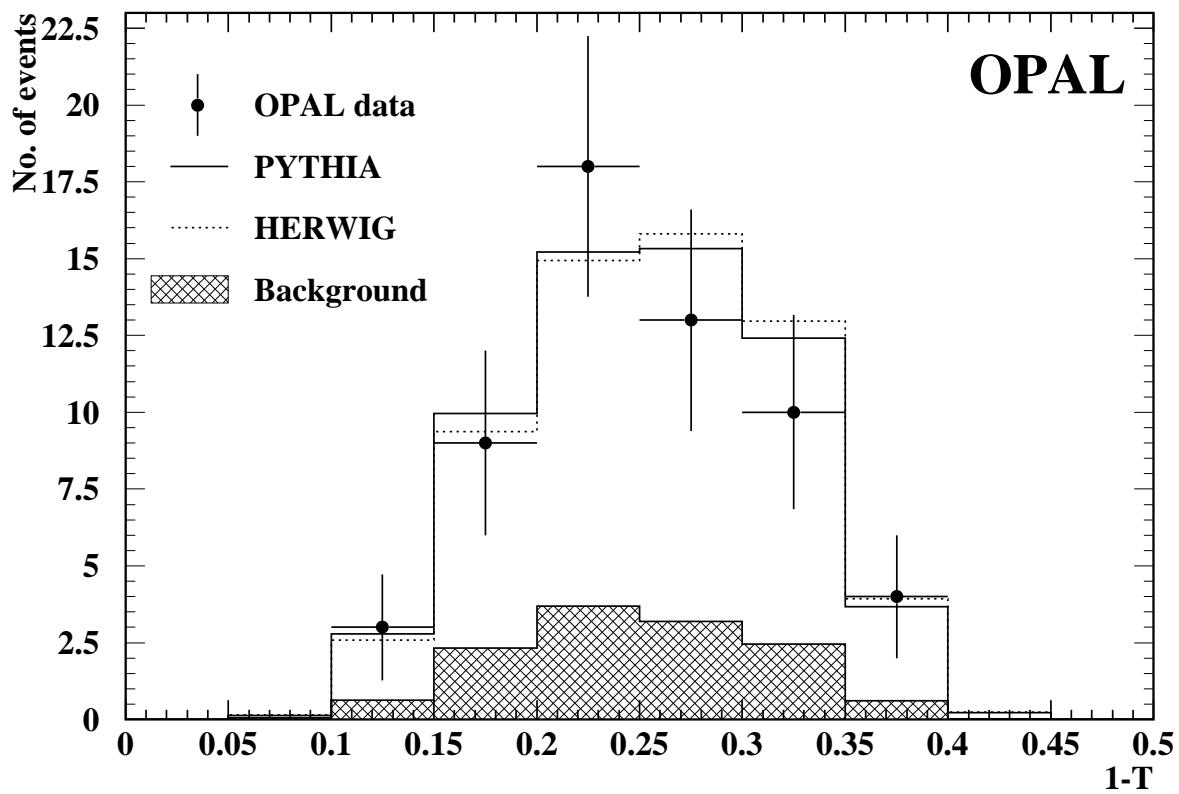


Figure 11: Uncorrected thrust distribution for  $W^+W^- \rightarrow q\bar{q}q\bar{q}$  events. The points indicate the data, the histograms show the total expected signal and background contribution for various signal models, and the hatched histogram shows the expected background.

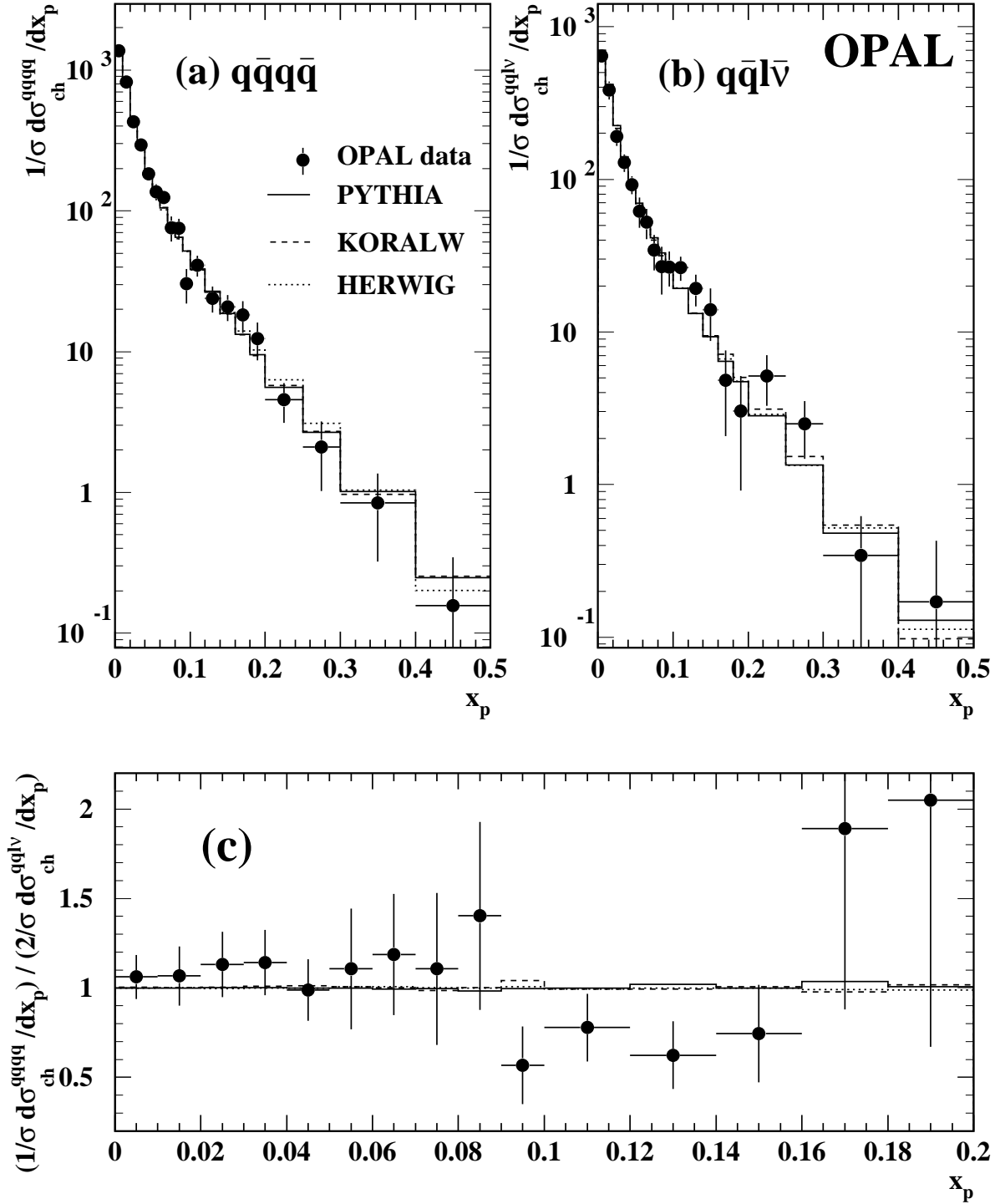


Figure 12: Corrected  $x_p$  distributions for (a)  $W^+W^- \rightarrow q\bar{q}q\bar{q}$  events, (b) the hadronic part of  $W^+W^- \rightarrow q\bar{q}l\bar{\nu}_\ell$  events and (c) the ratio of the  $W^+W^- \rightarrow q\bar{q}q\bar{q}$  distribution to twice the  $W^+W^- \rightarrow q\bar{q}l\bar{\nu}_\ell$  distribution. The points indicate the data, with statistical and systematic uncertainties added in quadrature, and the predictions of various Monte Carlo models (without colour reconnection) are shown as histograms.

## OPAL

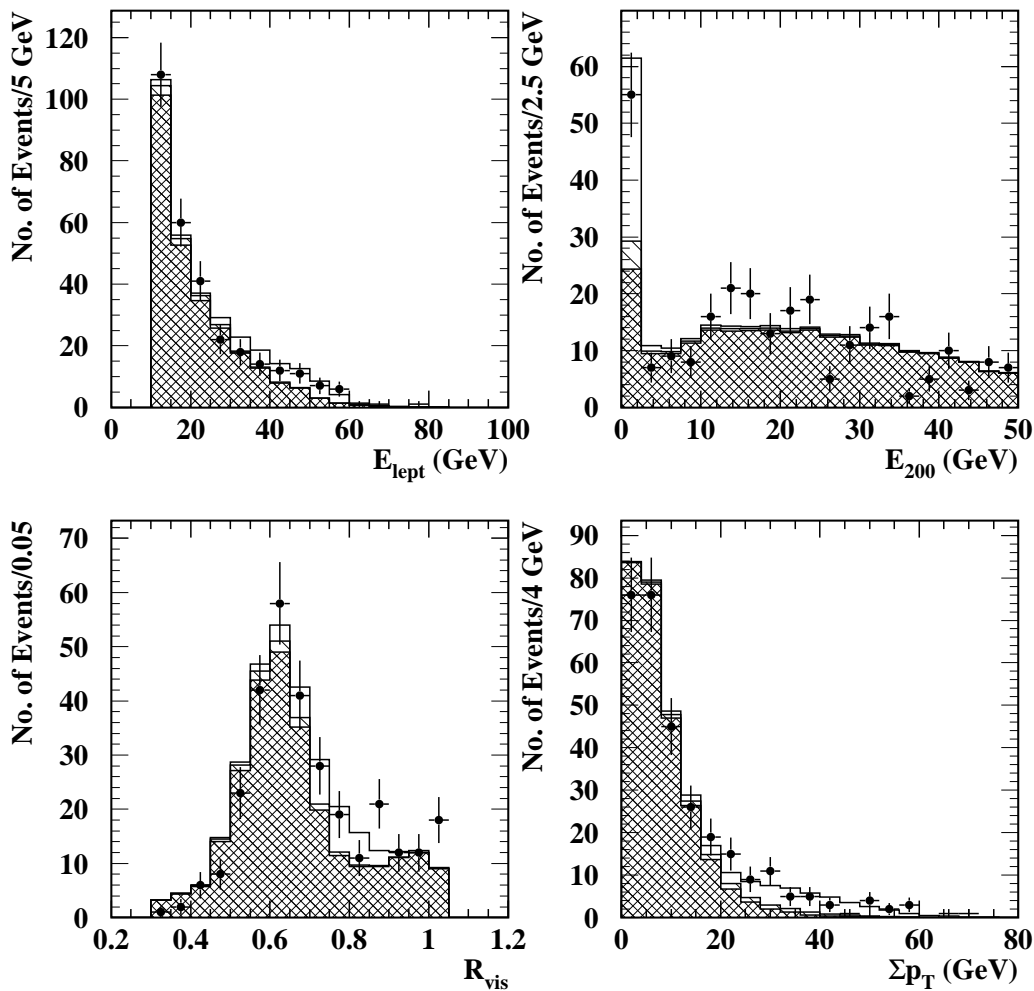


Figure 13: Distributions of some of the variables used in the  $W^+W^- \rightarrow q\bar{q}e\bar{\nu}_e$  and  $W^+W^- \rightarrow q\bar{q}\mu\bar{\nu}_\mu$  selections for events passing either the  $W^+W^- \rightarrow q\bar{q}e\bar{\nu}_e$  or the  $W^+W^- \rightarrow q\bar{q}\mu\bar{\nu}_\mu$  preselection cuts. The contribution from  $W^+W^- \rightarrow q\bar{q}\tau\bar{\nu}_\tau$  decays is shown as the single hatched histogram and the contribution from background processes as the doubly hatched histogram. The data are shown as the points with error bars.



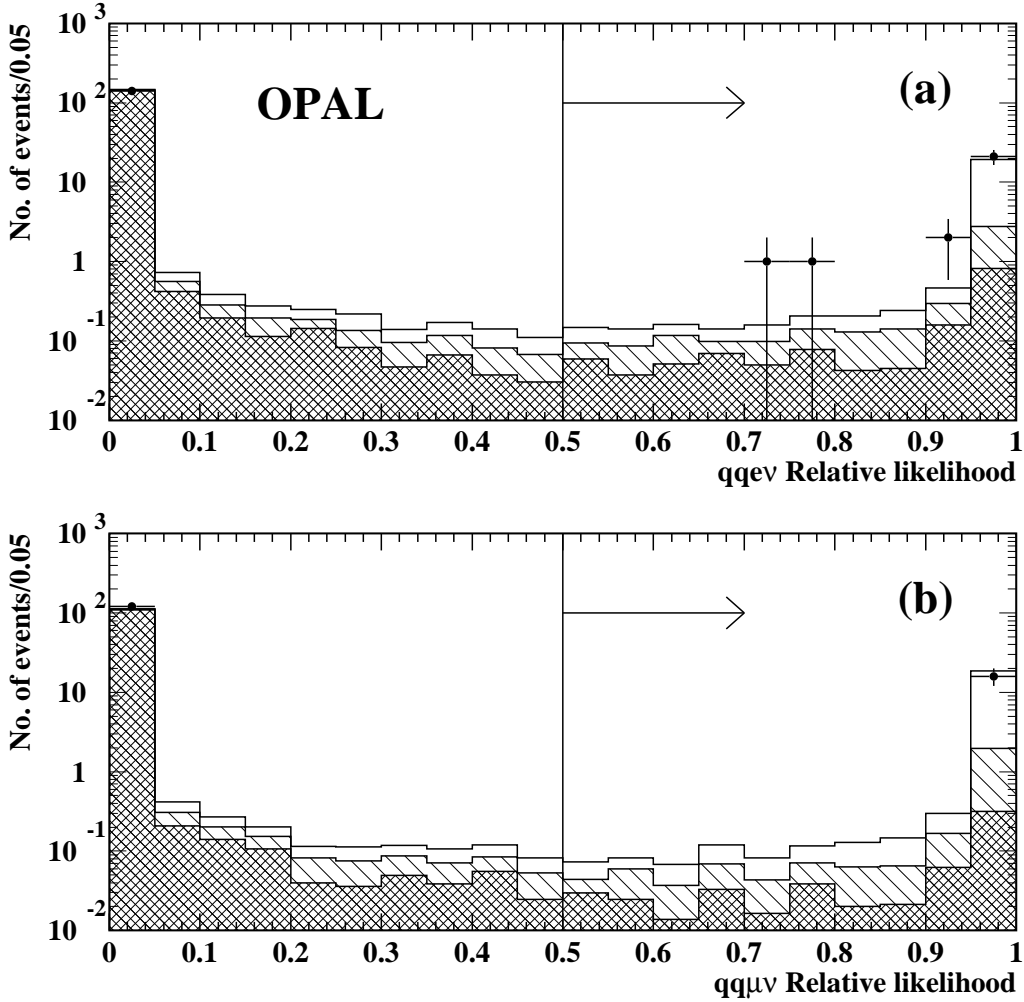


Figure 14: Values of the  $W^+W^- \rightarrow q\bar{q}e\bar{\nu}_e$  and  $W^+W^- \rightarrow q\bar{q}\mu\bar{\nu}_\mu$  relative likelihoods,  $\mathcal{L}^{q\bar{q}e\bar{\nu}_e}$  and  $\mathcal{L}^{q\bar{q}\mu\bar{\nu}_\mu}$ , for events passing the  $W^+W^- \rightarrow q\bar{q}e\bar{\nu}_e$  and  $W^+W^- \rightarrow q\bar{q}\mu\bar{\nu}_\mu$  preselection cuts respectively. The contribution from  $W^+W^- \rightarrow q\bar{q}\tau\bar{\nu}_\tau$  decays is shown as the single hatched histogram and the contribution from background processes as the doubly hatched histogram. The peaks in the background distributions near one arise predominantly from four-fermion background. The data are shown as the points with error bars. Events having relative likelihood values greater than 0.5 are selected, as indicated shown by the arrows.

# OPAL

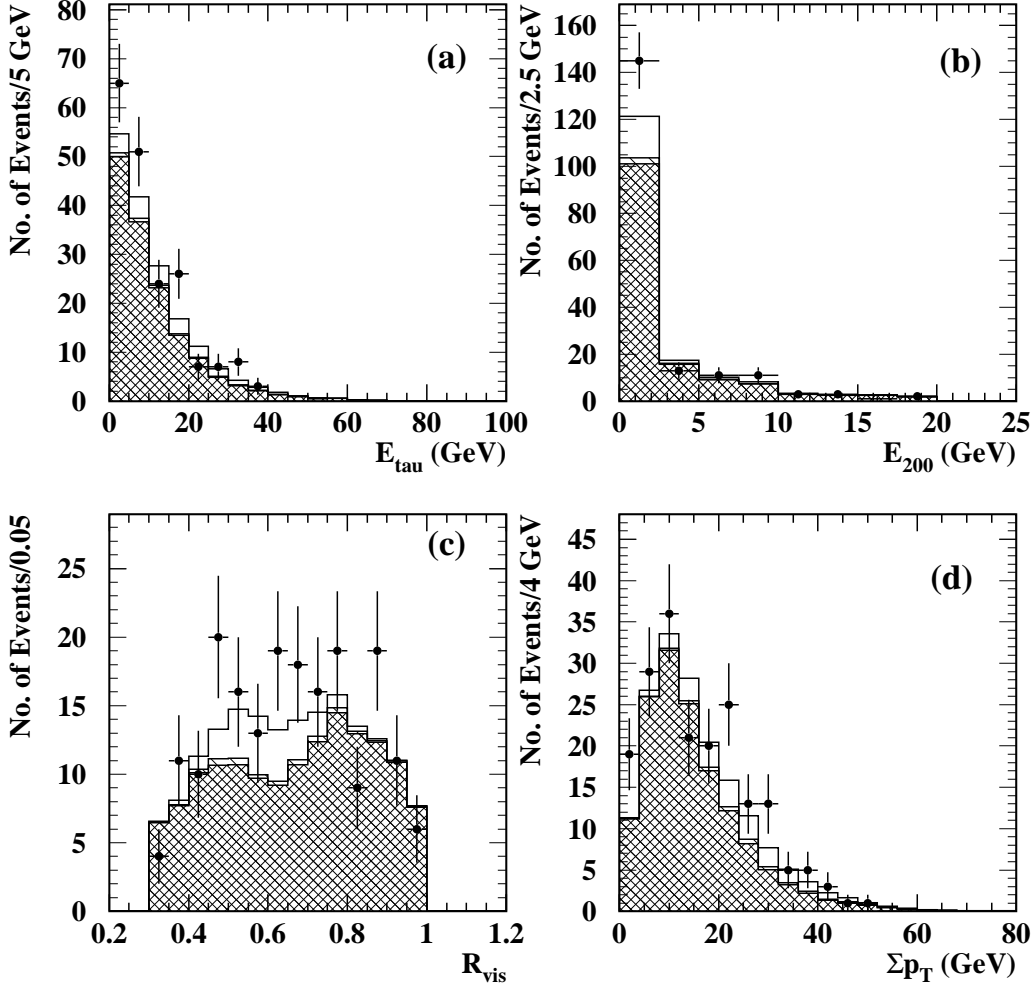


Figure 15: Distributions of some of the variables used in the  $W^+W^- \rightarrow q\bar{q}\tau\bar{\nu}_\tau$  selections for events passing the  $W^+W^- \rightarrow q\bar{q}\tau\bar{\nu}_\tau$  preselection cuts. Some events appear more than once in the plot since they can satisfy more than one of the  $W^+W^- \rightarrow q\bar{q}\tau\bar{\nu}_\tau$  preselections. The variables shown are; (a) the energy of the tau decay products, excluding the neutrino(s), (b) the energy within a 200 mrad cone about the tau candidate track(s) calculated using tracks only, (c) the scaled visible energy, after preselection cuts of  $0.3 < R_{\text{vis}} < 1.0$  and (d) the transverse momentum of the event. The contribution from  $W^+W^- \rightarrow q\bar{q}e\bar{\nu}_e$  and  $W^+W^- \rightarrow q\bar{q}\mu\bar{\nu}_\mu$  decays is shown as the single hatched histogram and the contribution from background processes as the doubly hatched histogram. The data are shown as the points with error bars.

## OPAL

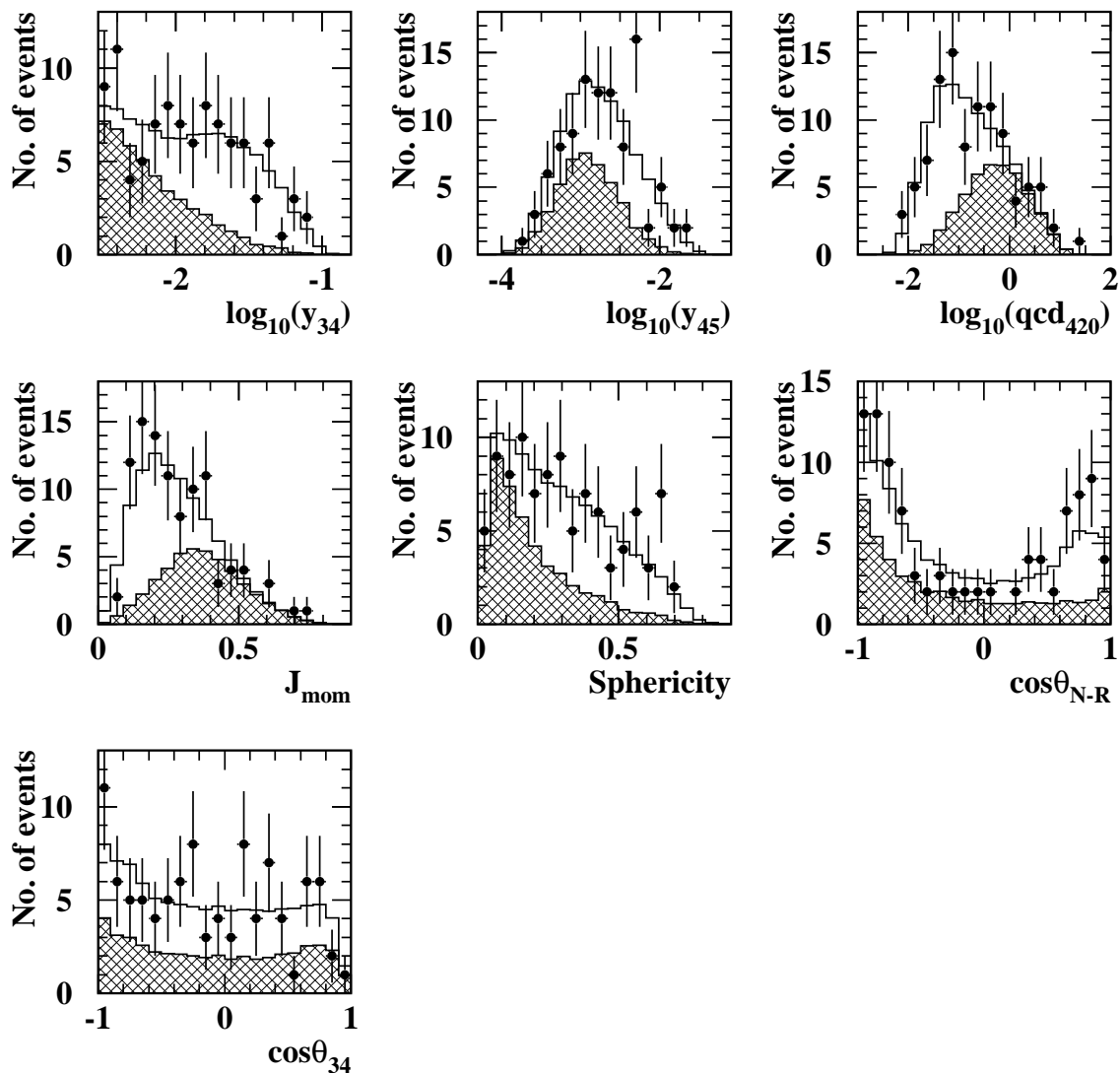


Figure 16: Distributions of the seven variables that have been used in the  $W^+W^- \rightarrow q\bar{q}q\bar{q}$  likelihood selection, after preselection. The points indicate the data, the open histogram shows the  $W^+W^- \rightarrow q\bar{q}q\bar{q}$  Monte Carlo and the hatched histogram shows the total background expectation.

# OPAL

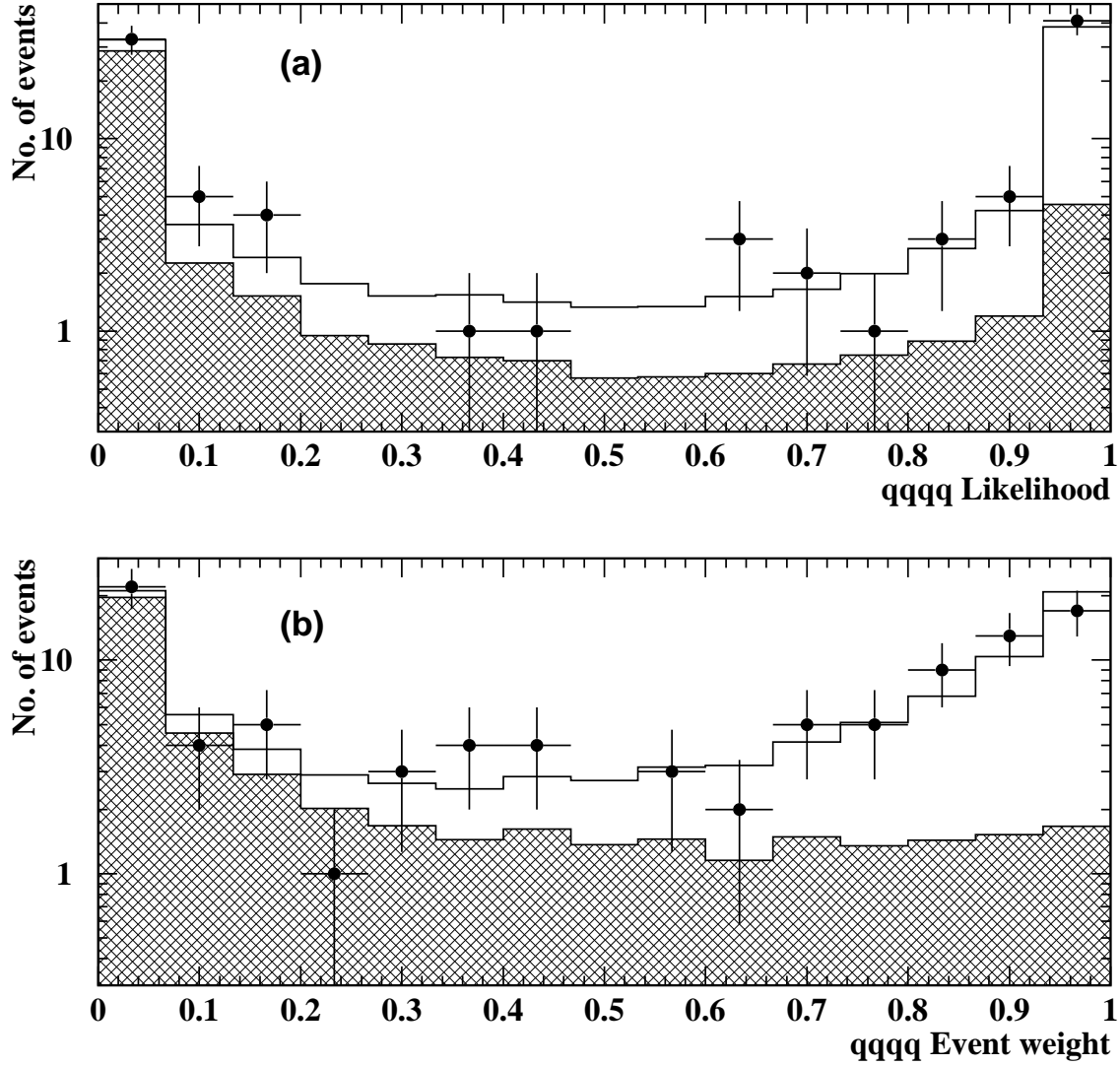


Figure 17: Distributions of (a) the likelihood distribution, used to select events for the mass and event properties analyses and (b) the event weights, used for the cross-section measurement. The points indicate the data, the open histogram shows the  $W^+W^- \rightarrow q\bar{q}q\bar{q}$  Monte Carlo and the hatched histogram shows the total background expectation.

